SE8100092

LUNFD6
~~LUNDF6~~/NFAS--0017

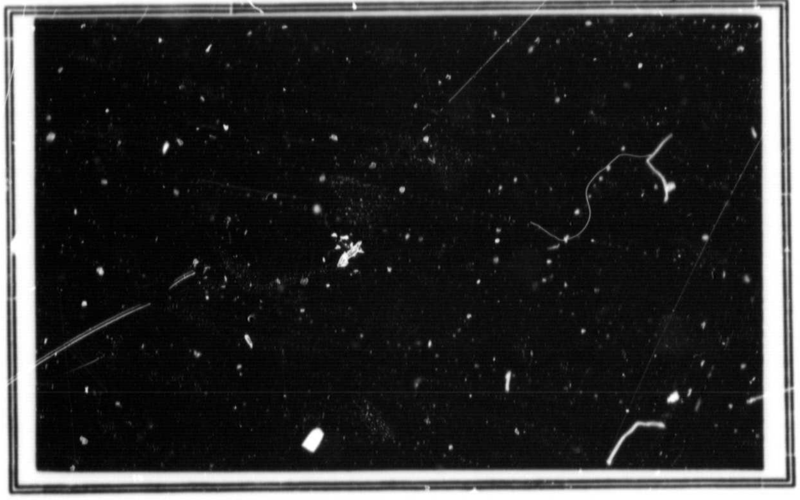

REPORTS
FROM
THE OBSERVATORY OF LUND

Please note that, according Studviks' letter dated 19 October 1981, the report number of this document should be

LUNFD/6 and not
LUNDF/6.

ERRATA

Replace eq. 2.1 on p. 8 by

$$\begin{bmatrix} I_1 \\ I_2 \\ U \\ V \end{bmatrix} = \frac{1}{k^2R_a^2} \begin{bmatrix} I_{11}(\theta) & I_{12}(\theta) & 0 & 0 \\ I_{21}(\theta) & I_{22}(\theta) & 0 & 0 \\ 0 & 0 & a_3(\theta) & b(\theta) \\ 0 & 0 & -b(\theta) & a_4(\theta) \end{bmatrix} \begin{bmatrix} I_1^o \\ I_2^o \\ U^o \\ V^o \end{bmatrix}$$

Replace eq. 2.2 on p. 8 by

$$\begin{bmatrix} I_1 \\ I_2 \end{bmatrix} = \frac{1}{k^2R_a^2} \begin{bmatrix} I_{11}(\theta) & I_{12}(\theta) \\ I_{12}(\theta) & I_{22}(\theta) \end{bmatrix} \begin{bmatrix} I_1^o \\ I_2^o \end{bmatrix}$$

Replace eq. 3.23 on p. 36 by

$$I_{AB} = \frac{I_B F}{k\ \rho} \left(\ell - \left|D_A \sin(\beta_A) - D_B \sin(\beta_B)\right|\right)$$

In the figure legend B.3 on p. 119, replace T41A in the fourth row by T11R.

Note:

I_{tot} as used in this text differs by a factor 2 from the intensity I of scattered natural light in the notations of van de Hulst (1957).

The total number of interfering pairs represented in figure B.3, p.119 are given by $\int P_{tot} dr$ where the integral were taken from 0 to the boundary of the ensemble.

Scattering by Ensembles of Small Particles

Experiment, Theory and Application

by

Bo Å. S. Gustafson

Reports from the Observatory of Lund, No. 17
1980
ISSN 0349-4217

This work is dedicated to my parents,

Elsa and Åke

Gustafson

Abstract

A hypothetical selfconsistent picture of evolution of prestellar interstellar dust through a comet phase leades to predictions about the composition of the circum-solar dust cloud. Scattering properties of thus resulting conglomerates with a "bird's-nest" type of structure are investigated using a micro-wave analogue technique. Approximate theoretical methods of general interest are developed which compare favorably with the experimental results. The principal features of scattering of visible radiation by zodiacal light particles are reasonably reproduced. A component which is suggestive of β-meteoroids is also predicted.

Key words: Light scattering by ensembles of small particles — cometary debris — interplanetary dust — zodiacal light.

Content

Chapter 1

Chapter 2

THE MICRO-WAVE ANALOGUE METHOD AND THE LABORATORY

Chapter 3

SCATTERING APPROXIMATIONS FOR SOME INHOMOGENEOUS PARTICLES OR SCATTERING SYSTEMS

Chapter 4

EXPERIMENTAL RESULTS AND VERIFICATION OF THE "INTERFERENCE" THEORY

Chapter 5

COMPARISON WITH ASTRONOMICAL OBSERVATIONS

TABLE OVER EXPERIMENTAL SECTIONS AND FIGURES

EXPERIMENT ID. # (SEE FOLD-OUT)	PRINCIPAL SECTIONS WHERE THE EXPERIMENT IS DISCUSSED	FIGURES PARENTHESES ARE FOR THEORY WITHOUT EXP. COMPARISON IN THE FIG.
T11R	4.1.7	4.20, 4.24, 5.7, 5.13, (B.3)
T21R	4.1.7, 4.1.9	4.2b, 4.2c, 4.20, 4.24, 4.27, 4.28, 5.4, 5.7, 5.10, 5.13
T41R	4.1.7, 4.1.8	4.20, 4.24, 4.26, 5.7, 5.13
TC21R	4.1.9, 5.2.3	4.27, 4.28, 5.4, 5.5, 5.10, 5.11
V21R	4.1.9, 5.2.3	4.27, 4.28, 5.5, 5.11
12	4.2.1	4.29, 5.3, 5.14
IC4b	4.2.1, 5.2.2, 5.2.3	4.30, 4.31, 4.36, 5.3, 5.6, 5.9, 5.12
IC4c	4.2.1, 5.2.2, 5.2.3	4.32, 4.33, 4.36, 5.3, 5.5, 5.6, 5.9, 5.11, 5.12
IC4d	4.2.1, 5.2.2	4.34, 4.35, 4.36, 5.3, 5.9
IC3b	5.2.3	4.37, 5.6, 5.12
IC1a	5.2.3	4.38, 5.4, 5.10
C41R	4.1.6	4.17, 4.19, D.2
T41A	4.1.1, 4.1.2, 4.1.3, 5.2.1	4.1, 4.2a, 4.3, 4.4, 4.5, 4.6, 4.8, 4.9, 4.10
U41A	4.1.5, 4.1.8	4.14, 4.15
U41R	4.1.6	4.18, 4.19, 4.26
C41A	4.1.5	4.14, 4.15
B11R	4.1.7	4.21a, 4.21b
B21R	4.1.7	4.22a, 4.22b
B41R	4.1.7, 4.1.8	4.23a, 4.23b, 4.26
P11	4.1.4	4.12, 4.13
Long $x = 1.88$ cylinder;		D.1
4:1 $x = 1.88$ cylinder (C41);	4.1.5	4.16a, 4.16b, D.1

Introduction

The interplanetary particles producing the zodiacal light by scattering of sunlight were for many years considered to be in a range of sizes not very widely different from the wavelength of visible radiation. Furthermore, most of the calculations of the brightness and polarization were done for spherical particles using Mie theory (for references see Weinberg, 1967, and the review article by Weinberg and Sparrow, 1978). A simple preliminary theoretical approach showed that significant modifications in the prediction were possible, if one used similar-sized particles but non-spherical rather than spherical ones (Greenberg, 1970).

Recent observations of the optical properties (Weinberg and Sparrow, 1978) and the size and composition of the interplanetary particles as determined from collection and impact studies (Fechtig, 1976, and Brownlee, 1978) have led to new concepts of the interplanetary particles. Large irregular particles in the 10 μm to 100 μm size range are now believed to provide most of the zodiacal light (Giese et al., 1978). To date, only two models have reasonably well reproduced the zodiacal-light brightness and degree of polarization as deduced by Dumont (1976) from observations. It is interesting that the two models were arrived at using quite different approaches. Fluffy interplanetary dust grains were studied by Giese et al. (1978) with connection to the type of particles collected in the Earth's upper atmosphere (Brownlee, 1978). Our approach is to apply an evolutionary model leading to the concept that we call a "bird's-nest" structure (Greenberg and Gustafson, 1980).

Chapter 1

THE PURPOSE OF THE INVESTIGATION

The hypothesis to be tested in this study is a unifying evolutionary model relating interstellar dust to comets and finally to the zodiacal-light particles. We will start with a set of assumptions that satisfy the existing observations but that may not be unique. It will be shown in chapter 5 that the resulting predictions are consistent with observations that in the absence of this model were unrelated. We adopt the bi-modal model for interstellar dust of Greenberg and Hong (1973). The comets are assumed to have aggregated directly from the dust during the formation of the Solar System. Finally, the zodiacal-light particles are modeled as cometary debris.

Although there is an identifiable mechanism for internal heating by primordial radioactive species, which could make a significant change in the internal structure of a comet nucleus (Irvine et al., 1980), our modeling is an attempt to work as closely as possible with constructs based on the hypothesis that we are seeing pieces from the surfaces of essentially primordial comets. One justification for doing this is that there is as yet no way of knowing to what extent comets of various sizes may have undergone internal or external structural or chemical modifications by heating. There are uncertainties both in the amount of primordial radioactive species accreted in the primordial comets as well as in the details of the heating process (d'Hendecourt and Greenberg, unpublished calculations). Another justification is that the albedo of comets (Delsemme and Rud, 1973) and the abundance of volatiles seem more consistent with at least the outer parts of a significant number of comets remaining primordial than being subject to high heating. Assuming that comets have undergone little change in their properties since birth - and this seems to be an inherent assumption in the "icy" models of Whipple (1978) and Delsemme and Rud (1973) - then the cometary debris could essentially be derivates of clumps of large numbers of interstellar grains.

The major constituents in the bi-modal distribution of interstellar grains as given by Greenberg and Hong (1973), are in the elongated core-mantle particles with silicate (or metallic oxide) cores of typically 0.05 μm radius surrounded by mantles of mean thickness about 0.1 μm composed of complex molecular mixtures of predominatly oxygen, carbon, and nitrogen with hydrogen (Greenberg, 1978). The mantles may achieve a mean thickness as large as about 0.15 μm (total grain diameter ≈ 0.4 μm) at the time when coagulation of the dust leads to the formation of the comet (Greenberg, 1979). Thus, the relative volume of mantle-to-core material is of the order of $(4:1)^3$ or about 60:1. The index of refraction of the silicate core is approximately $m = 1.6$ and the index of refraction of the mantle is about $m = 1.3$ as characteristic of complex ices. The absorption of the core and mantle material in the visible is quite low. The other constituents in the bi-modal distribution are in a large number of very small particles of not completely determined chemical composition, which however contribute at most a small amount both to the bulk (< 1%) and the optical characteristics of the aggregated material (Hong and Greenberg, 1980), even if they are predominantly made of graphite. This can also be seen by noting that the total absorption by such particles in the visual, in the interstellar medium, is small compared with the extinction by the core-mantle particles.

Subsequent to breaking away from the comet, the debris will be subjected to both solar radiation and solar wind particles. This is a rather complex problem to treat in its entirety because one should follow the particles during their entire lifetime (~ 10^5 years) while their orbits bring them within varying distances from the sun. It is illustrative that at 1 AU the sputtering or erosion of such components of the aggregate as H_2O ice could occur at a rate of about 5Å per year as a result of the solar wind (Lanzerotti et al., 1978). The less volatile components like the silicates and the very large molecules (which are not melted or evaporated at temperatures as high as 600 K) in the photo-processed grain mantles (Hagen et al., 1979) would undoubtedly erode at a much slower rate. Thus comet debris particles of initially ~ 100 μm radius could have parts of their outer material eroded away in varying amounts to depths up to ~ 50 μm leaving an open outer structure containing mostly the silicate cores and the nonvolatile mantle molecules. This tangle of elongated silicate particles as exposed in the outer portion of the comet debris particle or as imbedded in various degrees within the grain mantle material we envision as a bird's-nest type of structure. We note here that not only erosive effects can be produced by the solar wind particles but also as a processing of the debris matter analogous to the photo-processing of interstellar grains. The low density of the agglomerates as well as of the fluffy particles studied by Giese et al. (1978) is apparently not consistent with the densities inferred by Le Sergeant and Lamy (1978) from lunar rock cratering but is consistent with the densities ~ 1 g cm^{-3} inferred by Nagel et al. (1975) and with the micrometeoroid detections by the Helios 1 spacecraft (Grün et al., 1980), where it was found that a large number of particles have densities below 1 g cm^{-3}. In chapter 5 the optical properties of "bird's-nest" structures are compared to those inferred for the zodiacal-light particles. Clearly, the theory required to predict the exact scattering by such structures is far

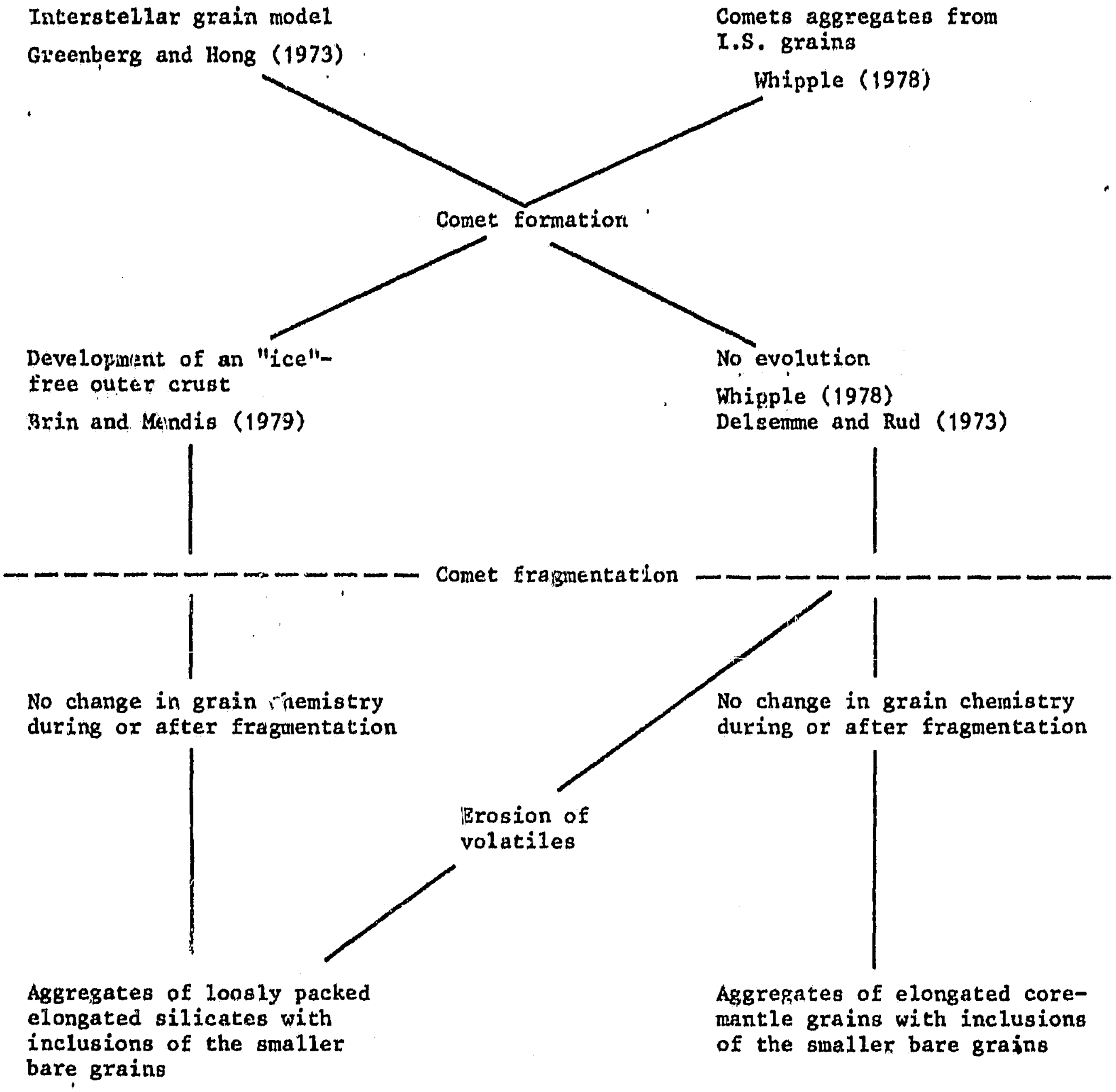

Fig. 1.1 Successions of theories and assumptions leading to the concept of "bird's-nests".

beyond the scope of present techniques. Not only need one consider a large number of particles simultaneously, as in normal multiple-scattering theory, but one must also take into account that the embedded silicates are close enough to each other to require inclusion of near-field modifications. Faced with this impossible situation we resort to the microwave analogue method described in chapter 2. Some of the targets discussed in chapter 4 are designed to clearly separate higher-order scattering effects from relatively easily predictable effects. The latter effects are included in the approximate method developed for investigation of light-scattering functions for some categories of inhomogeneous targets that fall outside the present laboratory constraints and especially for providing a first approximate understanding of this exotic field in light-scattering theory. The higher-order scattering effects are found to be negligible, so the comparisons with measurements in chapter 4 are quite reasonable.

Chapter 2

THE MICRO-WAVE ANALOGUE METHOD
AND
THE LABORATORY

2.1 Historical Background

In 1960, J. Mayo Greenberg constructed the first microwave analogue scattering facility to measure the extinction by single, irregular particles (see Lind, 1966). Over the years, such measurements have contributed significantly to characterizing (size, chemical composition, core-mantle nature of) interstellar grains. The micro-wave laboratory under its director Dr. D.W. Schuerman is now a part of the Space Astronomy Laboratory (S.A.L.) which is a research-only organization of the State University of New York at Albany. Most of the work reported in the present study were made at this laboratory.

The measurements for the three largest agglomerates were performed in the micro-wave facility of Bereich Extraterrestiche Physik, Ruhr Universität Bochum, German Federal Republic. In this laboratory scattering from cubes and other non-spherical particles, including the fluffy model for zodiacal-light particles, have been extensively investigated by R. Giese, R. Zerull and their co-workers.

2.2 The Analogue Method

In the general theory of scattering based on Maxwell's equations, all parameters involving the size of the particle are measured in units of the wavelength of the incident radiation. Thus, it is possible to scale the entire problem of visible, ultra-violet and infra-red scattering off micron and sub-micron particles to larger wavelengths and particle sizes. At S.A.L. the scale factor is about 10^5. Thus, apple-size particles are irradiated by micro-waves of $\lambda = 3.18$ cm. A particle of arbitrary shape is simulated by machining or molding a micro-wave target which is $\sim 10^5$ times larger than the real particle. The target material is selected by requiring it to have, at the frequency of 9.42 GHz, the same properties (dielectric constant, conductivity and size to wavelength ratio) as the actual particle has at visible, ultra-violet or infra-red wavelengths.

2.3 Measured Quantities

The scattering process is described by a 4 x 4 scattering (or F) matrix which operates on the intensity of the radiation as represented by the Stokes vector:

$$\begin{bmatrix} I_1 \\ I_2 \\ U \\ V \end{bmatrix} = \frac{1}{k^2R_a^2} \begin{bmatrix} I_{11}(\theta) & I_{12}(\theta) & 0 & 0 \\ I_{21}(\theta) & I_{22}(\theta) & 0 & 0 \\ 0 & 0 & a(\theta) & b(\theta) \\ 0 & 0 & b(\theta) & a(\theta) \end{bmatrix} \cdot \begin{bmatrix} I_1^o \\ I_2^o \\ U^o \\ V^o \end{bmatrix} \tag{2.1}$$

where $k = 2\pi/\lambda$ and R_a is the distance between the scatterer and the receiving antenna.

The matrix contains only six independent functions because it is assumed that the elements are averaged over a random distribution of similar particles. Since the input radiation, defined by the Stokes vector (I_1^o, I_2^o, U^o, V^o), is usually natural light, we set $(I_1^o, I_2^o, U^o, V^o) = (I_1^o, I_2^o, 0, 0)$ with $I_1^o = I_2^o = I^o$. From the form of the F matrix in equation (2.1), it is obvious that the Stokes vector of the scattered radiation must be of the form $(I_1, I_2, 0, 0)$, so that equation (2.1) can be written more economically as

$$\begin{bmatrix} I_1 \\ I_2 \end{bmatrix} = \frac{1}{k^2R^2} \begin{bmatrix} I_{11}(\theta) & I_{12}(\theta) \\ I_{12}(\theta) & I_{22}(\theta) \end{bmatrix} \begin{bmatrix} I_1^o \\ I_2^o \end{bmatrix} \tag{2.2}$$

The measured quantities are $I_{11}(\theta)$, $I_{12}(\theta)$, and $I_{22}(\theta)$. Given these values the total brightness

$$I_{tot}(\theta) = I_{11}(\theta) + 2I_{12}(\theta) + I_{22}(\theta) \tag{2.3}$$

and degree of polarization

$$P(\theta) = \frac{I_{11}(\theta) - I_{22}(\theta)}{I_{11}(\theta) + 2I_{12}(\theta) + I_{22}(\theta)} \tag{2.4}$$

can be determined.

2.4 Definition of Target Orientation

The orientation of a particle is defined with respect to the direction of the incident plane wave $\vec{k}_o$ and of the measured scattered radiation $\vec{k}_s$. Figure 2.1 represents an arbitrarily orientated cylinder whose symmetry axis makes an angle ψ with the perpendicular X to the scattering plane $k_o - k_s$ $(Y\text{-}Z)$ and whose projection in this plane makes an angle χ with the incident $\vec{k}_o$-vector. The angle between $\vec{k}_o$ and $\vec{k}_s$ is the scattering angle θ.

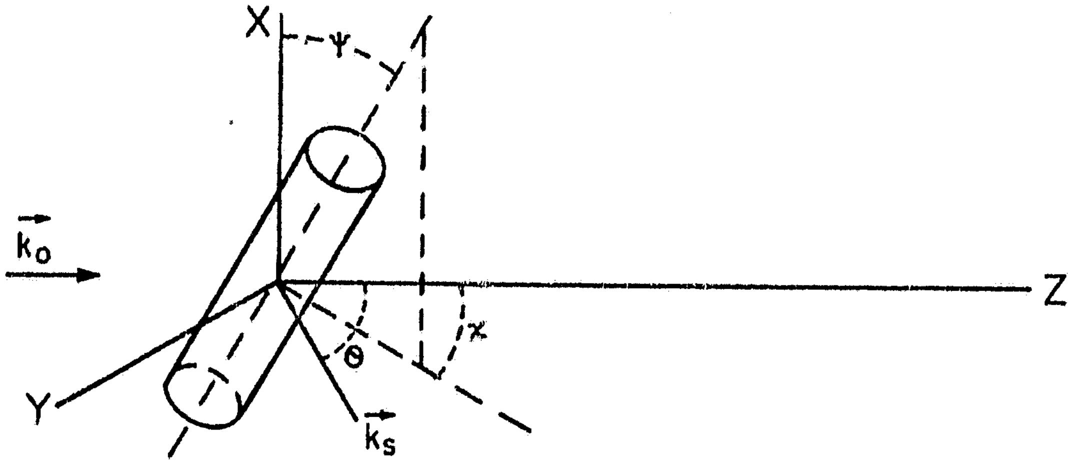

Fig. 2.1 Angular coordinates specifying the orientation of the symmetry axis of a cylindrical scatterer with respect to the direction of propagation $\vec{k}_o$ of the incident and $\vec{k}_s$ of the scattered radiation.

In the laboratory a target is mounted in such a way that it may be rotated around two mutually perpendicular axes, the laboratory fixed azimuth axis X, and the target fixed tilt axis which sweeps in the scattering plane. For particles that do not possess an axis of symmetry, an arbitrary axis is used as reference.

2.5 The Microwave Laboratory

2.5.1 The microwave laboratory at S.A.L.

The target, in operation, is suspended in the center of the micro-wave room by nylon monofilament lines, which are sufficiently thin to cause negligible scatter. The target is irradiated by micro-waves generated by a single screened dipole at the focus of a 51 cm diameter parabolic reflector located 9.84 m from the target. The dipole, which can be arbitrarily oriented in the focal plane by means of a rotary joint, is fed through a waveguide by a 9.42 GHz stabilized oscillator. The resulting scattered radiation is measured by means of a square-law crystal detector fed by a similar 41 cm diameter antenna at 5.18 m from the target. The signal is chopped by a 1000 Hz square-law modulator--fed diode switch located between the detector and a hybrid junction. In the junction the scattered signal is mixed with a background compensation signal, made equal in amplitude to the signal from the receiving antenna in the absence of the target by means of a variable attenuator and made destructive by use of a variable phase shifter. The compensation wave is tapped from the waveguide supplying the transmitting dipole by a 10 dB directional coupler. The length of the waveguide is choosen to minimize the optical path differences between background and compensation signals at small scattering angles, where direct radiation may be intercepted. A rotary joint on the waveguide permits the entire detection system to be mounted on a moving carriage and located at any scattering angle θ from 0 to 170°. A second antenna and detection system is located directly in line with the transmitter-target; it measures the amplitude and phase of the forward-scattered ($\theta = 0$) radiation. This antenna is located in a radiation trap and is covered by a micro-wave absorber during the side--scattering measurements. Further technical details may be found in Greenberg et al. (1967) and Wang and Greenberg (1978).

As part of a continuous effort, increased experimental accuracy and speed has been achieved by digitalizing the data handling and target orientation mechanism in two phases during the measurement period. We name the versions used in this study A, B and C.

2.5.2 Version A

The diagram in figure 2.2 represents the apparatus of version A. The output potential over the detector, which is proportional to the intensity of the incident radiation, is amplified up to 10^7 times by a lock-in amplifier unit linearly feeding the ordinate on an X-Y plotter. The abscissa is connected to a potentiometer which senses the azimuthal angle (χ) driven by an analogue motor. The motor is controled by a manually operated potentiometer through a feed-back mechanism using the χ-detector. A similar system controls the elevation and the tilt angle. For a detailed description of the orientation mechanism we refer to Lind (1966).

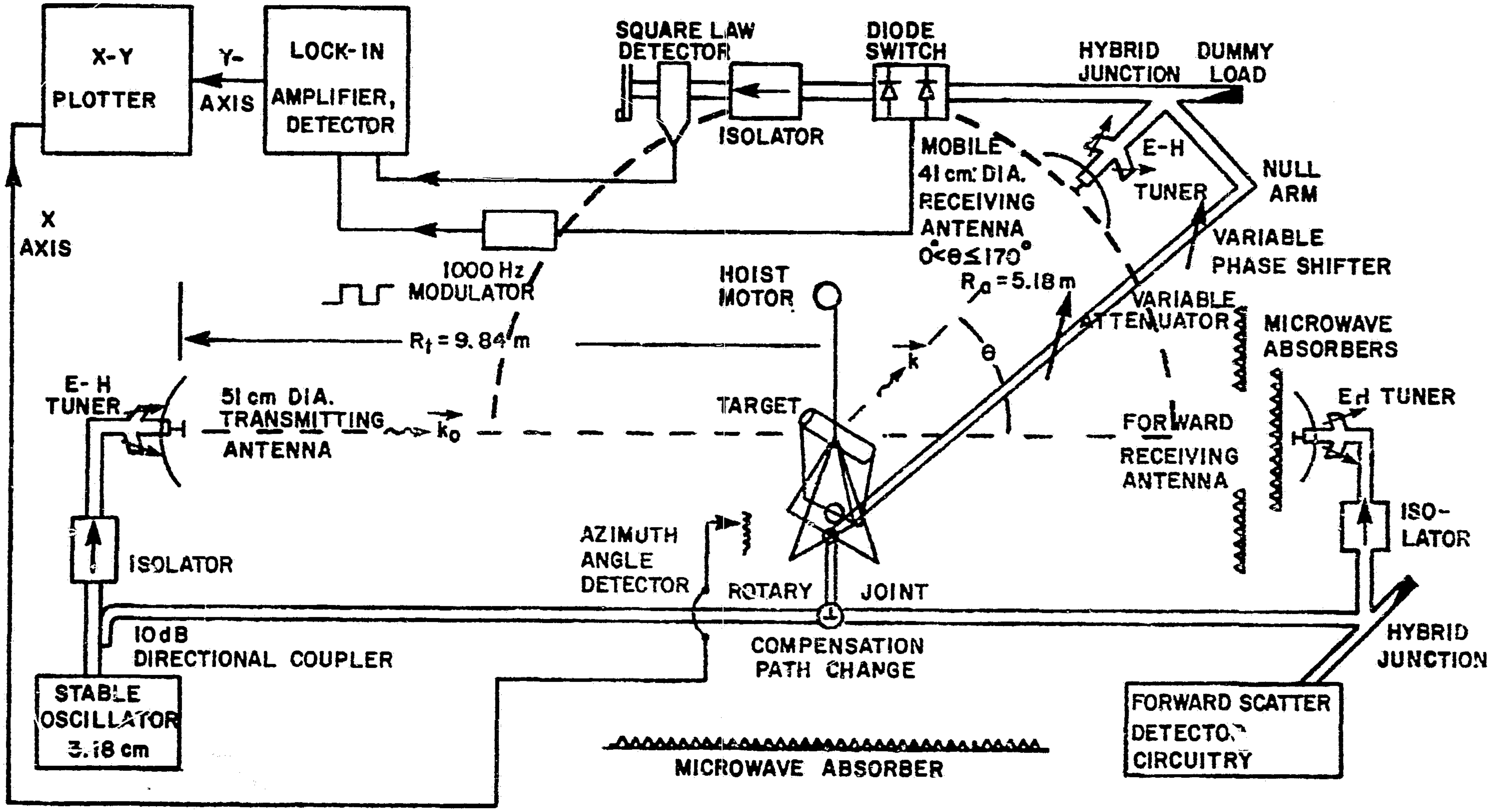

Fig. 2.2 Microwave circuitry version A, antenna diameters and ranges for angular distribution studies, at Space Astronomy Laboratory, State University of New York at Albany, Albany, New York.

2.5.3 Operating procedures, version A

The detector feeding a lock-in amplifier, described by Brophy (1977) or in any basic textbook in electronic engineering, is intermittently screened out. In the process of amplifying, the noise signal thus detected is subtracted. The square wave feeding the diode switch is used as reference signal. First, the phase is adjusted so that the output signal vanishes; we are then 90° from the correct phase if the reference wave is symmetric. At 180° phase shift the true signal is subtracted from the noise; the symmetry of the square wave is adjusted so that the output $U(180^0) = -U(0)$. At the beginning and end of a set of measurements the system is calibrated by detecting the known scatter of a standard target. Around the selected scattering angle $\theta = 45^0$, the phase function for the lucite sphere with circumference to wavelength ratio 4.978 is relatively feature less and the background is low. In the absence of the target, the residual signal is brought to less than 0.1 μV using the variable phase shifter and attenuator on the compensation waveguide. The target is placed in the beam and the height controlled through a telescope. One of 13 linear scales amplifying from 10 to 10^7 times were selected. This one scale was used as the target was rotated a full 180° around the azimuth axis. As the target rotates small oscillations in the detected signal, caused by inhomogeneties in the target material, average out. Subsequently, the scatter from targets with unknown optical properties can be measured. The background compensation procedure is repeated at each new scattering angle, and the apparatus is re-calibrated for each combination of polarizations. Intermediate calibrations were performed during long sets of measurements, especially after changes in the external conditions such as sunrise, sunset or thunderstorms. The data reduction from the graphs were performed manually ($\sim 10^4$ data points per target). The data presented for targets U41R and U41a was accumulated in this way. The measurements for targets T11R, T21R, T41R, T41A and C41 using this apparatus were in general agreement with the corresponding data using versions B or C of the laboratory. The later data is used in this study.

2.5.3 Apparatus and operating procedures, version B

The analogue motors in the orientation mechanism were replaced by step-motors orienting the target with a resolution of 0.1°. The tilt mechanism, originally used for very elongated targets, was redesigned and the range increased from < 180° to 180° by use of a constant tension spring-motor counteracting the pull of the step-motor. The range of the azimuth drive was increased to 400°. Two sets of micro-wave absorbers were added to screen out the orientation mechanism. A PDP-11/03 DECLAB minicomputer was installed to control the step-motors, reading of the lock-in amplifier, and for data reduction. A laser for re-alignment of the receiving antenna at each scattering angle was mounted on the

Fig. 2.3 The four aluminium arms of the target orientation mechanism used in versions B and C of the laboratory are mounted on the rotating azimuth plate supported by three adjustable rolls. The free end of each arm is connected to the target by use of a thin nylon monofilament string. The tilt mechanism rotates with the azimuth plate. The background wall is covered by micro-wave absorbers. The boxes contain other absorbers and form screens that can be repositioned according to the needs in each configuration of polarization and scattering angle.

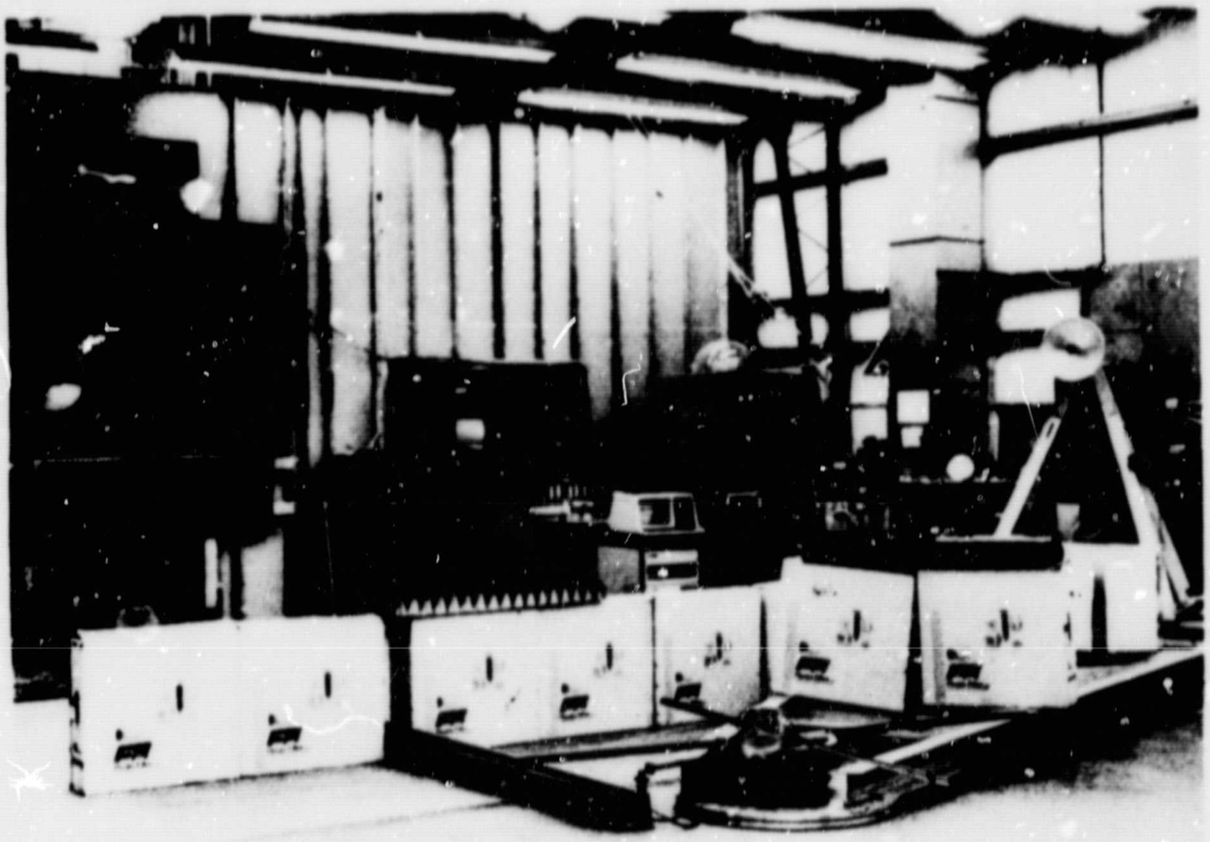

Fig. 2.4 View of the micro-wave laboratory at the Space Astronomy Laboratory, State University of New York at Albany, U.S.A..

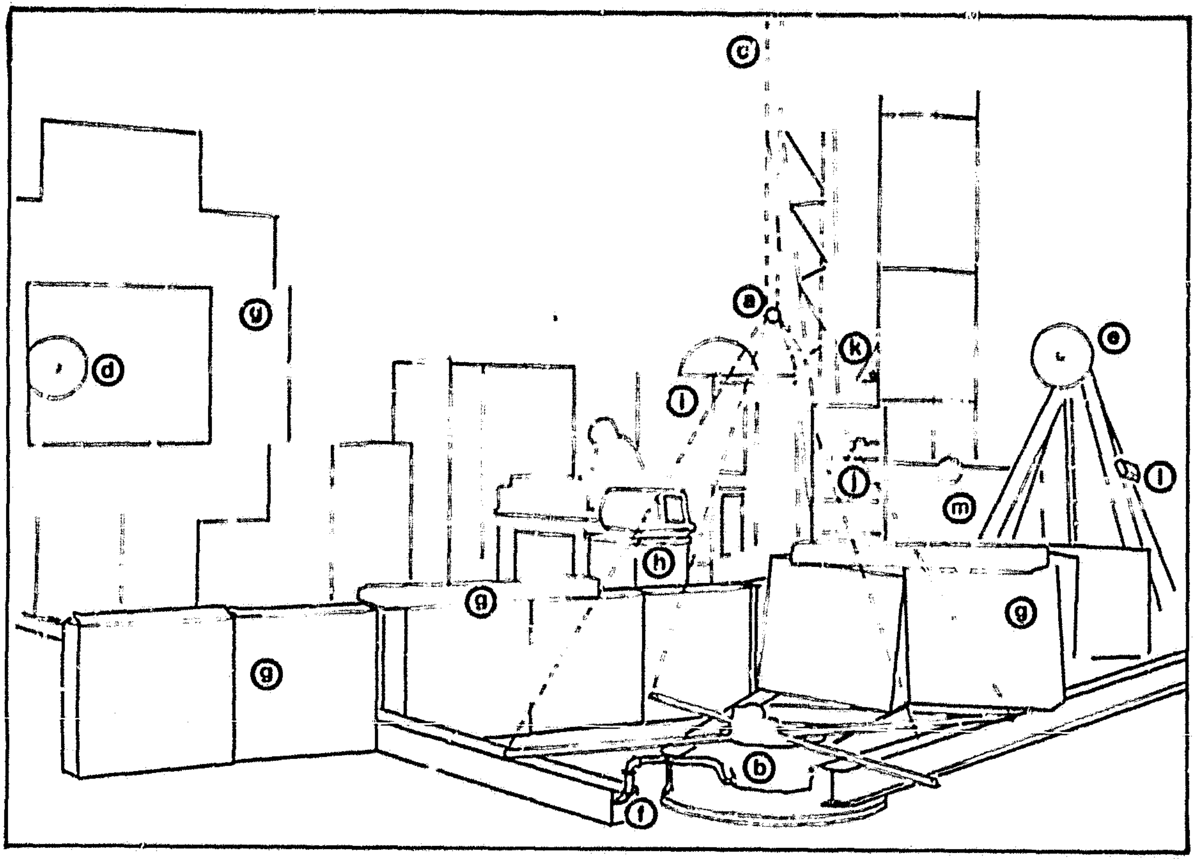

The dashed lines are the nylon monofilament strings supporting and orienting the target.

Figure code:

a - spherical target
b - target orientation mechanism
c - to the hoist
d - transmitting antenna
e - receiving antenna
f - background compensation waveguide
g - micro-wave absorbers
h - mini-computer
i - power supply and computer interface with the step motors
j - detector electronics on a mobile rack
k - telescope for target alignment
l - laser for antenna alignment
m - target rack

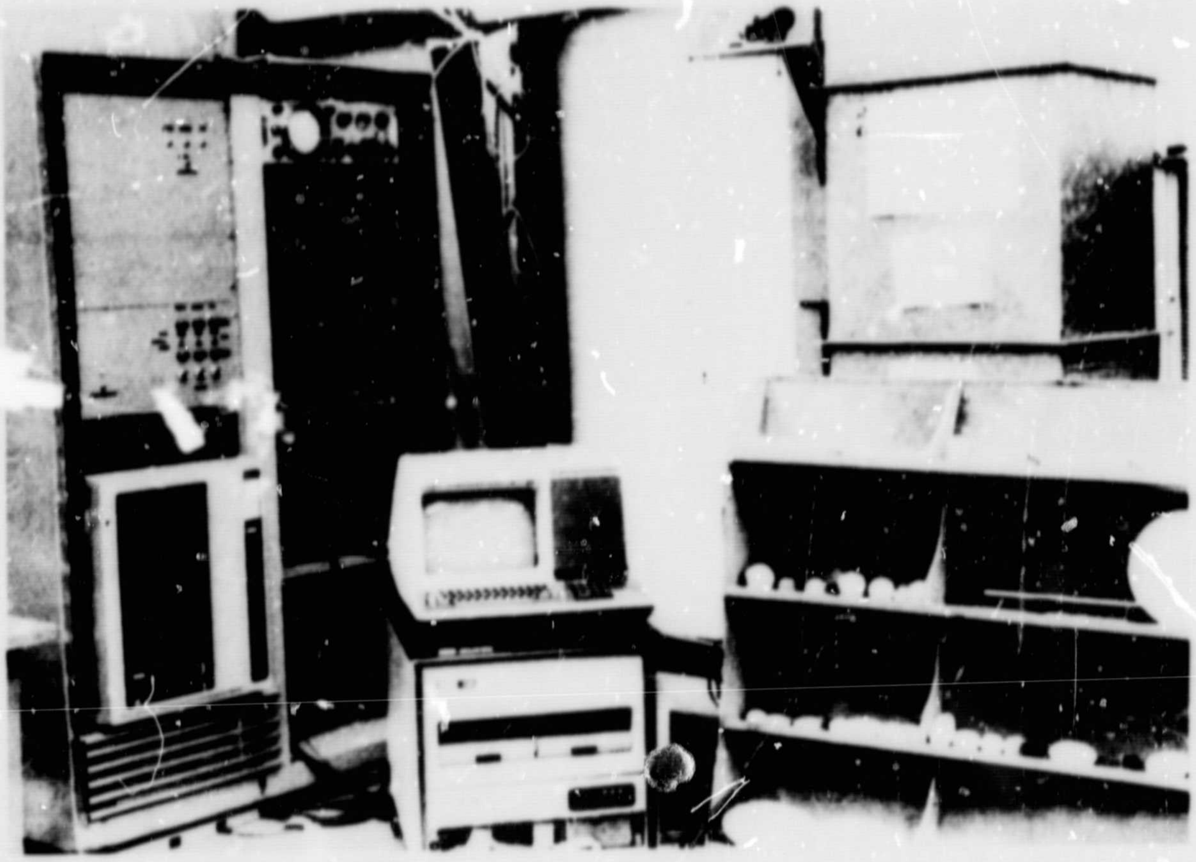

Fig. 2.5 The PDP 11/03 Declab mini-computer in the center orients the target, collects the scattered signal and stores the result on a floppy-disc. The rack to the left contains the power supply to the step motors and interface electronics as well as a band station for magnetic tape. Some micro-wave targets are seen on the rack to the right.

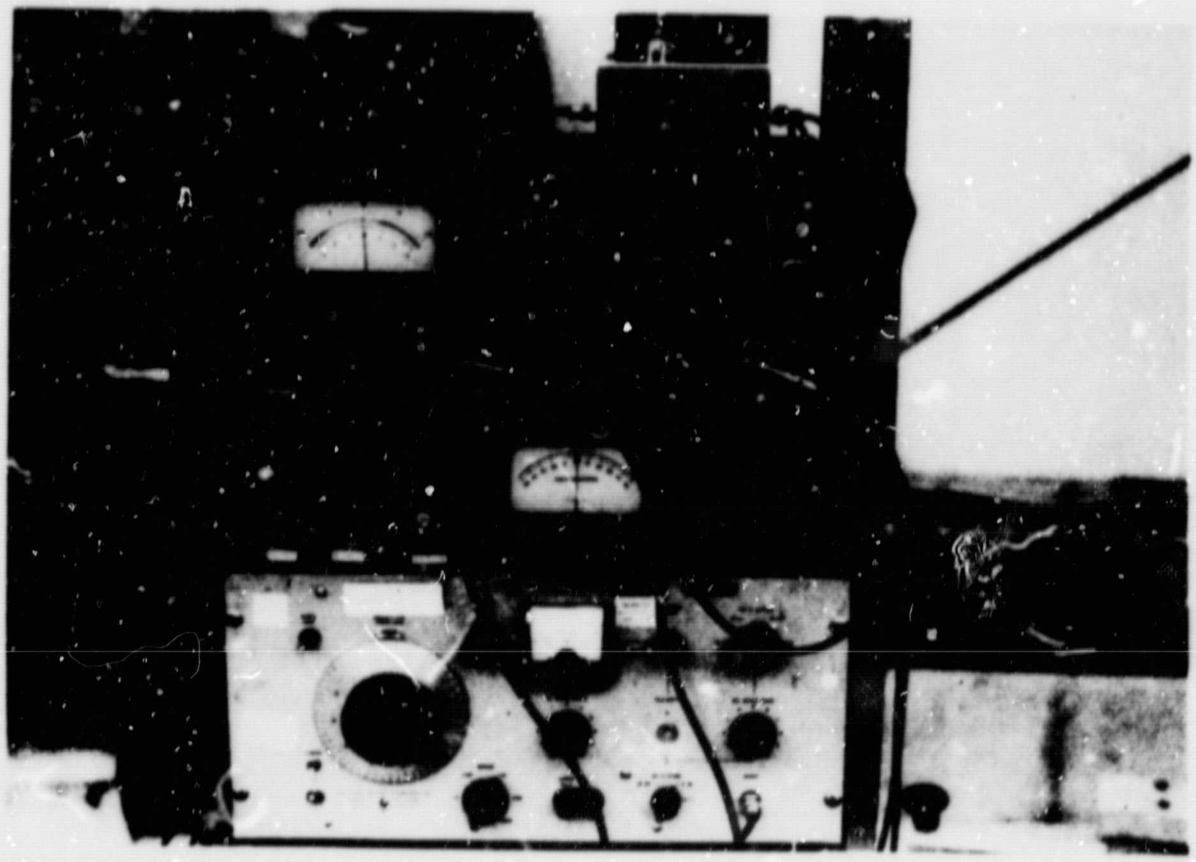

Fig. 2.6 The 1000 Hz square wave modulating the diod switch which periodically screens out the detector is used as reference signal to the lock-in amplifiers in the upper part of the rack. The square wave is generated by the oscillator seen below. One of the two sets of lock-in amplifiers is computer controlled.

mobile carriage. The computer was programmed to step the target through any preselected set of orientation. At each orientation 21 measurements were collected, and if the mean fell outside 15-85% of the full-scale value at the selected gain the measurement was rejected and new measurements were taken at this orientation when the appropriate scale (requested by the computer) had been set. If not rejected, data was sampled at each of these orientations until the standard deviation of their mean was less than any preselected value or a maximum of 10^4 measurements was reached. The average and the number of measurements were stored on a floppy disc along with a flag indicating if the preselected standard deviation of the mean was reached. Using this apparatus targets T11R, T21R, T41R, T41A and IC1a required an average of 250-300 hours each for a full set of measurements.

2.5.5 Apparatus and operating procedures, version C

A second lock-in amplifier controlled by the computer and with maximum gain of 10^8 was installed. The manually controlled amplifier was still used for nulling. This and other refinements have gradually increased the rate of measurements to ~ 45 hour/particle.

2.5.6 Errors

The uncancelled background signal $I_b \lesssim 0.02$ interferes with the scattered signal I_s. The resulting intensity I is given by

$$\sqrt{I} = \sqrt{I_s} + \sqrt{I_b} \cos \Delta$$

where Δ is the phase difference. If the intensity I_s incident on the detector causes a potential difference of 10 μV. The potential $8.1 \leq U_I \leq 12.2$ in μV or in absolute units $0.162 \leq$ [illegible] $\lesssim 0.244$ results. However, the phase of the background signal may vary rapidly (if not rapidly variable it can be canceled). If Δ is truly random over the set of measurements, at each orientation the intensities add directly; thus, $U_I = 10.1$ μV. In the case of the "bird's-nests" at higher scattering angles, the phase of the scattered wave takes all values as the target is stepped through the 272 orientations, therefore the maximum error of the mean is given by $(\sqrt{I_s} + \sqrt{I_b})^2 - I_s$ at $\theta = 0$ and approaches $I_b = 0.02$ at higher scattering angles. Drift in the gain may reach 10%. For this reason, the system was re-calibrated against the standard sphere intermittently during the course of measurements. The (generally) small cross-polarization components vanish for spheres, the average of the calibration constants for the 11 and 22 components were substituted. The agreement between theory and measurements for scattering by spheroids using verions B and C of the apparatus was found to be very good (Schuerman et al., in preparation). This was still true when the cross-polarization terms were calibrated as in tnis study.

2.5.7 The micro-wave laboratory at Ruhr Universität Bochum

The laboratory operates at 35 GHz and is intended for side-scattering only. Both transmitting and receiving antenna are of the horn type. The mobile receiving antenna, mounted on a track, stops automatically every 5° as it moves from $\theta = 155^{\circ}$ to 50°. In this interval, there is no compensation for the background. At other scattering angles the target is removed from the beam and the background cancelled in a manner similar to that at S.A.L.. The scattered signal is integrated electronically as the target is rotated 360° in the scattering plane. The gain is calibrated through the known scatter of a standad sphere at one given scattering angle. For a more complete description, see Zerull (1973).

2.6 Target Manufacturing

2.6.1 "Bird's-nests"

In space, the "bird's-nest" type particle problem involves three media, vacuum ($m = 1$), "ice" ($m \approx 1.3$) and silicates ($m \approx 1.6$). This is modelled in the laboratory, using the four media; air ($m \approx 1$), eccofoam ($m \approx 1$), eccofoam PS 1.7 ($m \approx 1.3$) and lucite ($m \approx 1.6$). In all cases the imaginary part is small. The eccofoam is used to fix the relative positions of the individual scatterers and is similar to eccofoam PS 1.02, which is optically almost identical with air except at small scattering angles. The match of refractive indices is within the uncertainty for the cosmic materials. The "bird's-nests" were built in modules (see Table 1) which can be combined arbitrarily. Lucite, also known as plexiglas, is an acrylic that is commercially available in long rods. The cylinders were cut to size from appropriate diameter rods. The indices of refraction ($m = 1.618 - 0.005i$) of two samples cut out of an 1.5 inches diameter cylinder, both made to fit snugly into a waveguide only differing in length, were derived from two sets of standing wave patterns arising inside the waveguide containing a respective sample using the slotted waveguide method of Roberts and van Hippel (1954) and further developed by Wang (1968). The eccofoam PS is a low loss polystyrene manufactured by Emerson & Cuming Inc. The dielectric

TABLE 1

Number of modules	elongation length/diam.	diam. inches	homogeneous lucite	core lucite	elongation length/diam.	diam. inches	mantle eccofoam PS 1.7
700	4 / 1	3/16	X				
650	2 / 1	3/16	X				
840	1 / 1	3/16	X				
50	2 / 1	5/16	X				
100	4 / 1	3/4	X				
80	2 1	5/16		X	2 / 1	1	X
44	2 / 1	1/4		X	2 / 1	.8	X
1	210/ 1	3/4	X				
	hollow eccofoam PS 1.02 or similar sphere			cavity diameter inches			
1		X			7.7		
1		X			6.3		
1		X			5.0		
1		X			4.0		

constant ε, being closely related to the density of the target, is adjusted by pre-heating, and thus controlled expansion of the target material. Eccofoam PS 1.02 has $\varepsilon \approx 1.02$. In eccofoam PS 1.7, microspheres (36 DS) are mixed to the polystyrene to achieve $\varepsilon = 1.7$ to an accuracy of ± 0.02 (Emerson & Cuming Inc., pers. com.). The dissipation factors $\tan\delta$ are smaller than 0.0002 and 0.0001 respectively. The resulting refractive indexes,

$$m = \sqrt{\frac{\varepsilon + \sqrt{\varepsilon^2 + (\varepsilon \tan\delta)^2}}{2}} - i\sqrt{\frac{-\varepsilon + \sqrt{\varepsilon^2 + (\varepsilon \tan\delta)^2}}{2}}$$

are ≈ 1.01 and 1.304 ± 0.003 respectively. The eccofoam PS 1.7 was sawed very slowly (less than 1 inch/min.) and cooled with running water to avoid further expansion due to friction heat. The resulting square rods (1 x 1 x 5.5 inches) were machined circular in a lathe and cut to 1.0 or 0.8 inch diameter cylinders. Each cylinder was cut in two, and a concentric hole drilled (see Fig. 2.7) to accomodate the lucite cylinder. The two eccofoam parts were glued together using a paper glue with index of refraction close to 1.3. The resulting concentric cylinders, with length-to-diameter ratio of both core and mantle 2:1, were exposed to a 0.4 mm Hg vacuum for more than an hour to evaporate any remaining water and to dry out the glue.

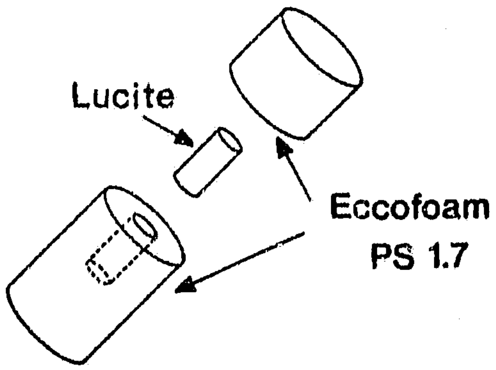

Fig. 2.7 Model of an interstellar core-mantle grain. Each eccofoam ("icy"-material at visual wavelengths) cylinder is cut in two and a concentric and coaxial hole drilled to accomodate the lucite (modelling silicate type material) cylinder. The two eccofoam parts were glued together using a paper glue with index of refraction close to that of the eccofoam ($m \approx 1.3$).

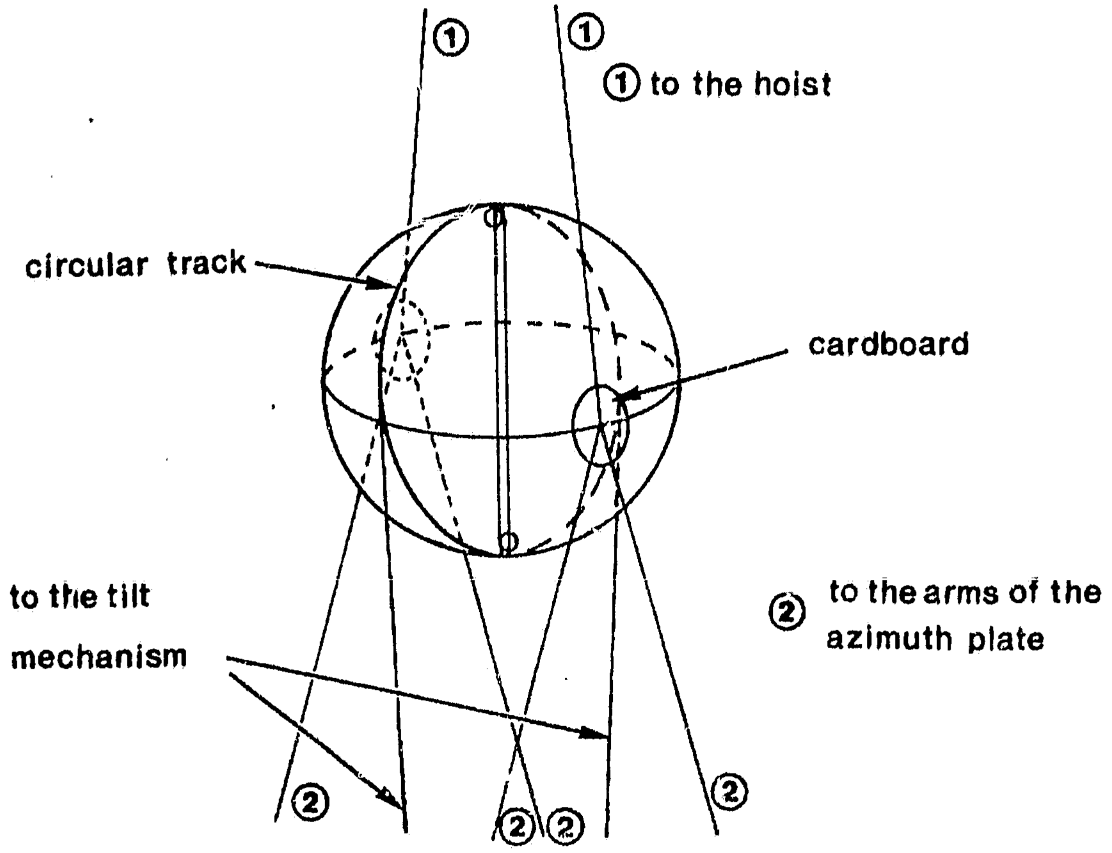

Fig. 2.8 One of the spherical eccofoam shells pictured as part of the target positioning mechanism. The nylon monofilament string connecting to the tilt motor windes on a machined circular track and reinforces the bound between the upper and lower eccofoam hemispheres by first passing diametrically across the sphere then following the machined track 360° and passing back diametrically across the sphere again. The nylon (fish-) line and the eccofoam are almost invisible at the microwave part of the electro-magnetic spectrum.

The hollow eccofoam spheres ($m \approx 1$ define the shape and size of the agglomeration and are part of the suspension mechanism. Homogeneous spheres of this material are commercially available. Using an arrangement similar to that of a lathe, a well defined track was carved out for the tilt string. Then the spheres were cut approximately along a great circle and the halves carved out with a razor blade to avoid crushing the material. The spherical boundary was purposely made rough to prevent the cylinders sliding. The halves were glued back together and an opening cut out. The volume was measured by inserting a plastic bag and filling it with water to obtain the volume (or weight). The removed material was saved to be inserted between cylinders. The hole passing the string connecting to the hoist was reinforced by small pieces of cardboard. The string connecting the tilt mechanism also reinforces the bond between the hemispheres as pictured in Fig. 2.8. The spherical cavity was then filled with the desired mixture of cylinders and filling material (eccofoam) such that the number density of cylinders was constant in layers.

Some of the smaller "bird's-nests" containing only lucite cylinders were made by inserting the cylinders into an eccofoam sphere thereby keeping the number density constant in concentric spherical layers Two, orthogonal annular rings were fit around the sphere (no glue). On one the track for the tilt mechanism string was machined; the other was used to attach the strings to the hoist. The two "bird's-nests" containing aligned cylinders were also made from solid eccofoam spheres but these were cut in hemspheres, and the cylinders were inserted perpendicularly to the plane surfaces to facilitate alignment. As these targets were never tilted the strings attached to the hoist were glued directly to the eccofoam.

2.6.2 Single cylinders

The single circular homogeneous or concentric cylinders, as described in the previous section, were suspended by two strings glued directly to the cylinder on diametrically opposite points equidistant from the two ends. The two strings used to control the target tilt-angle were glued on opposing cylinder edges, such that the projection of the total of four points of attachments on a plane perpendicular to the symmetry axis are corners of a square.

2.7 Simulation of an Optically Thin Cloud of Randomly Orientated Scatterers

An optically thin cloud of randomly orientated particles is simulated by averaging the signals received from a few hundred uniformly distributed particle orientations. This set of orientations for a particle having axial symmetry is obtained by pointing the symmetry axis of the particle to 272 positions almost uniformly distributed over an imaginary sphere centered on the particle. Perfect uniformity cannot be achieved - a fact known to the ancient Greeks who discovered that only 4, 6, 8, 12 or 20 points could be so distributed over a sphere. However, by distributing points over a pentagon in an almost uniform manner, one can combine 12 such pentagons to form a dodecahedron - one of the five regular figures which can be inscribed in a sphere. In this sense, we obtain the closest approximation possible to uniformity.

2.7.1 Uniform distribution of all orientations of the single cylinders

The single cylinders C41 and 12 have both an axis of rotational symmetry and a plane of symmetry perpendicular to this axis. The cylinders were orientated so that their axis of symmetry was successively pointing to 1/8 of the 272 orientations determined as described above. The 34 orientations were chosen as described in appendix A for axial symmetric particles with a plane of symmetry perpendicular to the symmetry axis. Also 8 fixed orientations including alignment of the symmetry axis with the incident $\vec{k}$, $\vec{E}$ and $\vec{H}$ -vectors were investigated; but the results are excluded from the present study.

2.7.2 Uniform distribution of all orientations of a "bird's-nest"

The "bird's-nest" type dust grains are asymmetrical. Thus only the symmetry relation a defined in appendix A prevails. All possible orientations using the laboratory orientation mechanism are independent as long as the tilt axis does not coincide with the bisectrix of the complement to θ. We will first consider the orientation of "bird's-nests" consisting of cylinders aligned for perpendicular incidence. To keep the cylinder axes perpendicular to the incident radiation we are only free to rotate the target around the azimuth axis. Let $\chi = 0$ be an arbitrary orientation around the azimuth axis. The target is then orientated to $360^\circ - \Delta\chi$ with increments of $\Delta\chi$. At each orientation, measurements are performed until the standard deviation of their mean is less than a pre--selected value (with a minimum of 21 and maximum of 10,000 measurements). As can be seen in Fig. 4.2 the scattered intensity oscillates heavily as the target is rotated, as a result of interference of the contributions from individual scatterers. The periodicity p of the oscillations is dependent on the scattering angle. This phenomenon is discussed in appendix B. To avoid systematic errors we choose $\Delta\chi \ll p$. This condition leads to several thousand orientations at the higher scattering angles. If the "bird's-nest" consists of randomly orientated cylinders we may also rotate around the tilt axis, or to 10^6 - 10^7 orientations. At an average rate of 10 sec per orientation, the time required is of the order of a year or more. Instead the 272 orientations resulting from a combination of 12 pentagons were used.

2.8 The Targets Selected

Of the 17 targets used in the measurements, eleven represent agglomerates of, or single, homogeneous silicate cylinders. The remaining six targets represent agglomerates of, or single, silicate-core - ice-mantle cylinders. It is convenient to refer to 21 separate sets of measurements as represented in the fold out page, because som targets have been investigated at two wavelengths or at differing orientations. In the group of ten targets nine sets of measurements (B41R, U41R, C41R, B21R, B11R, U41R, C41A, P11 and T41A, where the two digits stands for the elongation of individual cylinders and the final letters A for aligned and R for random) and one (12R in the group of six targets) were selected to illuminate the multiple scattering problem and provide tests for the theory. Target 12 represents a single interstellar grain, and its scattering characteristics are therefore of interest for other astronomical applications as well. The rest of these scatterers do not represent likely cosmic grains at visual wavelengths, with the possible exception of T41A. All the other pure silicate "bird's-nests", model cometary debris from which the volatiles have erroded before or after fragmentation. The silicate-core--ice-mantle group of targets represent pieces from comets that have remained premordial.

The agglomerates correspond to the 1.5 - 6 μm diameter range at λ = 5000 Å and our biggest model for actual cometary debris corresponds to a 3 μm particle. This is dictated by the laboratory constraints. Actual comet debris, however, have a rather wide size distribution and the optically most important zodiacal light particles are thought to be in the 10 - 100 μm size range (Weinberg and Sparrow, 1978). For future interpretation of scattering from larger dust particles an approximate theory is developed in chapter 3.

Chapter 3

SCATTERING APPROXIMATIONS FOR SOME INHOMOGENEOUS PARTICLES OR SCATTERING SYSTEMS

3.1 Scattering at Long Wavelengths Compared to the Inhomogeneties of Their Mutual Distances

We may divide the inhomogeneous target material into volume elements that are small compared to the wavelength λ of the incident radiation. If the material is randomly inhomogeneous there is a wavelength such that the integrated polarizability over the volume elements is uniform. At this and larger wavelengths the particle acts like a homogeneous scatterer with the index of refraction $\tilde{m}$ given by

$$\tilde{m} = 1 + 2\pi P , \tag{3.1}$$

where P is the induced dipole moment per unit volume.

3.2 The Target Material when $m \approx 1$

When λ is made short enough some volume elements contain individual molecules while other are vacuum. If the mutual distances between volume elements with $m \neq 1$ are $\gg \lambda$ each volume acts like an individual scatterer. The extinction and dispersion in a dilute medium of N randomly spaced scatterers with forward scattering amplitude $S(0)$ is discussed by van de Hulst (1957, p. 32). It is shown that a wave travelling through the medium suffers a phase lag and attenuation, that can be represented by the complex index of refraction $\tilde{m}$ of a homogeneous material,

$$\tilde{m} = 1 - i\, S(0)\, \frac{2\pi N}{k^3} . \tag{3.2}$$

Let $z = 0$ be the boundary of the target material. Then we may write the incident electric field

$$E_o = e^{i\omega t} \tag{3.3}$$

and the field incident from the negative z direction on the particle with coordinate y_i, z_i in the scattering plane as

$$E_{oi} = e^{-ikz_i\tilde{m} + i\omega t} \; , \qquad (3.4)$$

Combining eq. 3.3 and 3.4,

$$E_{oi} = E_o e^{-ikz_i\tilde{m}} \; . \qquad (3.5)$$

The field scattered from the target to the point y,z in the far field is given by

$$E_s = S\left(\arctan \frac{y-y_i}{z-z_i}\right) \frac{e^{-ik\sqrt{(y-y_i)^2 + (z-z_i)^2}\,\tilde{m} + i\omega t}}{ik\sqrt{(y-y_i)^2 + (z-z_i)^2}} \; , \qquad (3.6)$$

or in units of the radiation incident on the scatterer,

$$E_s = S\left(\arctan \frac{y-y_i}{z-z_i}\right) \frac{e^{-ik\sqrt{(y-y_i)^2 + (z-z_i)^2}\,\tilde{m}}}{ik\sqrt{(y-y_i)^2 + (z-z_i)^2}} E_{oi} \; . \qquad (3.7)$$

Insertation of eq. 3.5 into 3.7 gives

$$E_s = S\left(\arctan \frac{y-y_i}{z-z_i}\right) \frac{e^{-ik\left(\sqrt{(y-y_i)^2 + (z-z_i)^2} + z_i\right)\tilde{m}}}{ik\sqrt{(y-y_i)^2 + (z-z_i)^2}} E_o \; . \qquad (3.8)$$

The total scattered intensity from N particles is simply

$$I(y,z) = \left(\sum_{i=1}^{N} E_s^i(y,z)\right)^2 \; . \qquad (3.9)$$

In the forward direction $y=y_i$ thus eq. 3.8 becomes

$$E_s = S(0)\, \frac{e^{-ikz\tilde{m}}}{ik(z-z_i)} E_o \qquad (3.10)$$

so that the amplitude but not the phase of the forward scattered wave depends on the particle location. Thus the scattered radiation is strongly peaked in the forward direction because of interference. Note that in the limit where the material of infinite dimensions is homogeneous $I(\theta)$, $\theta \neq 0$ vanishes. If the Rayleigh approximation $S(0) = ik^3\alpha$ for the forward scattering by the volume elements is substituted the mean index of refraction can be written from eq. 3.2

$$\tilde{m} = 1 + 2\pi\alpha N \tag{3.11}$$

where α is the polarizability of the particle. The assumption made in deriving eq. 3.2 is that the system of scatterers is dilute, which implies that $\tilde{m} \approx 1$. In this limit the Lorentz-Lorenz formula

$$4\pi\alpha N = \frac{3(\tilde{m}^2 - 1)}{\tilde{m}^2 + 2} \tag{3.12}$$

can be rewritten as

$$4\pi\alpha N \approx \tilde{m}^2 - 1 \approx 2(\tilde{m} - 1) \tag{3.13}$$

so that the two formulae are equivalent for $m \approx 1$. This relationship is pointed out by van de Hulst (1957).

So far we have discussed the extreme cases where $\lambda \gg$ the dimensions of the individual scatterers and further more their mutual distances are either $\ll \lambda$ or $\gg \lambda$. The discussion and the formulae in this section apply to any dilute system of scatterers separated by distances large compared to λ and to the particle dimensions with the appropriate solution for $S(0)$.

3.3 Particles Very Large Compared to the Wavelength

The condition in the previous section was that the distance between scatterers $\gg \lambda$. This implies that the formula derived in that section only apply to scattering systems $\gg \lambda$. In this particular case the incident plane wavefront of infinite extent can be thought of as consisting of separate rays that persue their own path. The condition is that the ray of length L must have a width of the order of $\sqrt{L\lambda}$ corresponding to the first few Fresnel zones. The rays passing along the particle form a plane wave from which a part in the form and size of the geometrical cross section of the particle is missing. This incomplete wavefront by Huygens' principle produces the Fraunhofer diffraction pattern at small scattering angles (see van de Hulst 1957, p. 24, or any textbook in basic scattering theory). The Fraunhofer diffraction is unpolarized, and by definition independent of the internal structure of the particles. Furthermore, the restrictions on target shape are not very rigorous. At larger scattering angles the scattering resulting from eq. 3.9 where the summation is made over the whole ensemble, dominates. An interesting result is known as Babinet's principle (van de Hulst, 1957). We will make the classical set of imaginary experiments; (1) we replace the particle by a disc that totally blocks an area of the wavefront of the same shape and size as the geometrical cross section. The diffraction observed is identical with that of the particle blocking the wavefront. (2) If instead the whole wavefront is covered, except for a hole of the same geometry as the particle cross section, a similar diffraction pattern is seen, but the electric fields are of opposite signs. (3) Obviously, if we were to combine the two diffraction patterns (1) and (2), they cancel each other by destructive interference. In (3) we do not block any part of the wave and therefore the wavefront must remain undisturbed. Let a be a typical dimension for the particle (for spheres we let a be the radius). Then similarly, if we place a large particle with the index of refraction $m \ll 1 + \frac{\lambda}{2\pi a}$ in the homogeneous wavefront, the diffraction pattern (1) is partially cancelled. The restriction on m means that the phase difference between light rays that have passed aside the particle and the transmitted wave is small.

The resulting scattering pattern for the large scatterers discussed in this section is strongly peaked in the forward direction where the Fraunhofer diffraction pattern (1) dominates. If the condition $m \ll 1 + \frac{\lambda}{2\pi a}$ is fulfilled, the diffraction pattern has the same shape as in (1) but is lower in magnitude. In other directions the scattering given by eq. 3.9 dominates. The side--scattering depends strongly on particle shape and size and goes generally through a large number of oscillations as a function of θ. As an example, an ensemble of scatterers in the shape of a hexahedron aligned along the axes X,Y,Z, defined in section 2.4 will scatter in phase at $\theta = 0$, $I(0) = (\sum_{i=1}^{N} E_i(0))^2$. If the target contains N truly randomly located scatterers and the thickness is $n \frac{\lambda_m}{2}$, where n is a large integral number and λ_m is the wavelength inside the target, $\lim_{N\to\infty}(I(180^\circ)) = \sum_{i=1}^{N} E_i^2 (180^\circ) = \sum_{i=1}^{N} I_i (180^\circ)$. If the dimensions along the Y- and Z-axes each are mupliples of λ_m, then $\lim_{N\to\infty} (I(90^\circ)) = \sum_{i=1}^{N} I_i (90^\circ)$. If m is isotropic (randomly oriented scatterers) eq. 3.9 is indpenendent of the state of polarization of the scattered radiation. Therefore the degree of polarization is small where the Franhofer diffraction domintates and approaches that for individual scatterers as θ increases.

3.4 Expected Effects on the Scattering Pattern as the Target Size Decreases

The Fraunhofer diffraction pattern will extend to higher scattering angles and decrease in relative total intensity when the target size decreases. The interference pattern (eq. 3.9) remains constructive father out and the number of oscillations in the scattered intensity as a function of θ decreases. As the number of individual scatterers decreases, the angular distribution becomes increasingly dependent on the relative location of scatterers, because the phase differences between contributions from individual scatterers fluctuates statistically around the asymptotic mean value at $N\rightarrow\infty$ as different but always random distributions of the finite sample of scatterers are chosen. This effect is observed in the laboratory as oscillations in the scattered signal when the ensemble is rotated at a fix scattering angle. This effect and it dependence on θ is discussed in appendix B.

3.5 Expected Effects on the Scattering Pattern as the Distance between Scatterers Decreases

The components of the polarizability vector joining individual scatterers, and multiply scattered radiation, will increase in importance when the distances between scatterers decrease. These two effects can not easely be evaluated partially because the particles are not in each other farfields any longer. We resort to the micro-wave laboratory.

3.6 The Single-Scattering Approximation

Both single- and secondary-scattering computations were performed for T41A consisting of 125 randomly located 4:1-elongation silicate cylinders all aligned perpendicular to the scattering plane, each with the circumference-to-wavelength ratio or size parameter $x = 0.47$ in a spherical ensemble with size parameter $X = 10.04$. For each cylinder the scattered intensity and phase respectively were computed separately. This was dictated by the limitation of core size available in the computer.

3.6.1 Intensity

For the finite cylinders with $x = 0.47$ the particles are too small to provide reliable experimental data as individuals. Also the infinite cylinder computations are not readily normalized (see appendix D) because the intensity at a distance r in the far zone is proportional to r^{-1} rather than r^{-2} as for finite targets. Therefore, we have substituted appropriately normalized spheroid calculations. Each cylinder is replaced by an equal volume spheroid whose scattering is computed using the Rayleigh approximation.

3.6.2 Phase

The phase is defined with respect to an imaginary wave deflected at the target site in vacuum. The optical path of radition scattered off a cylinder A (D,α,β) in the "bird's-nest" of radius R and with mean index of refraction $m_{eq} = m' - im''$, is

$$\overline{O} = (\overline{e_iA} + \overline{Ae_o})(1 - m') + \overline{w_iA} + \overline{Aw_o} \tag{3.14}$$

see Fig. 3.1.

Let
$$r = \sqrt{R^2 - D^2\sin^2(\beta)}$$
$$x = D\cos(\beta)\cos(\alpha)$$
$$y = D\cos(\beta)\sin(\alpha) \tag{3.15}$$

Then;

$$\overline{e_iA} = \sqrt{r^2 - y^2} + x$$
$$\overline{Ae_o} = \sqrt{r^2 - (y\cos(\theta) + x\sin(\theta))^2} - x\cos(\theta) - y\sin(\theta)$$
$$\overline{w_iA} = \sqrt{R^2 - y^2} + x$$
$$\overline{Aw_o} = \sqrt{R^2 - (y\cos(\theta) + x\sin(\theta))^2} - x\cos(\theta) - y\sin(\theta) \tag{3.16}$$

The resulting phase, where ph_A is the phase shift over the cylinder, is

$$PH = (\overline{O} - 2R)\frac{2\pi}{\lambda} + ph_A \tag{3.17}$$

Note that m' in eq. 3.14 formally results from secondary scattering.

3.6.3 Some predictions by the single scattering approximation

The maximum phase shift in the $\theta = 0$ direction over the ensemble with radius R is given by

$$PH_{\text{max}} = 2(m_{eq} - 1)X \approx 16\,\frac{R\pi^2}{\lambda}\,P \tag{3.18}$$

where the dipole moment P per unit volume is proportional to NR^{-3} and N is the number of identical agglomerated particles, thus $PH_{\text{max}} \propto NR^{-2}$ and the inter-

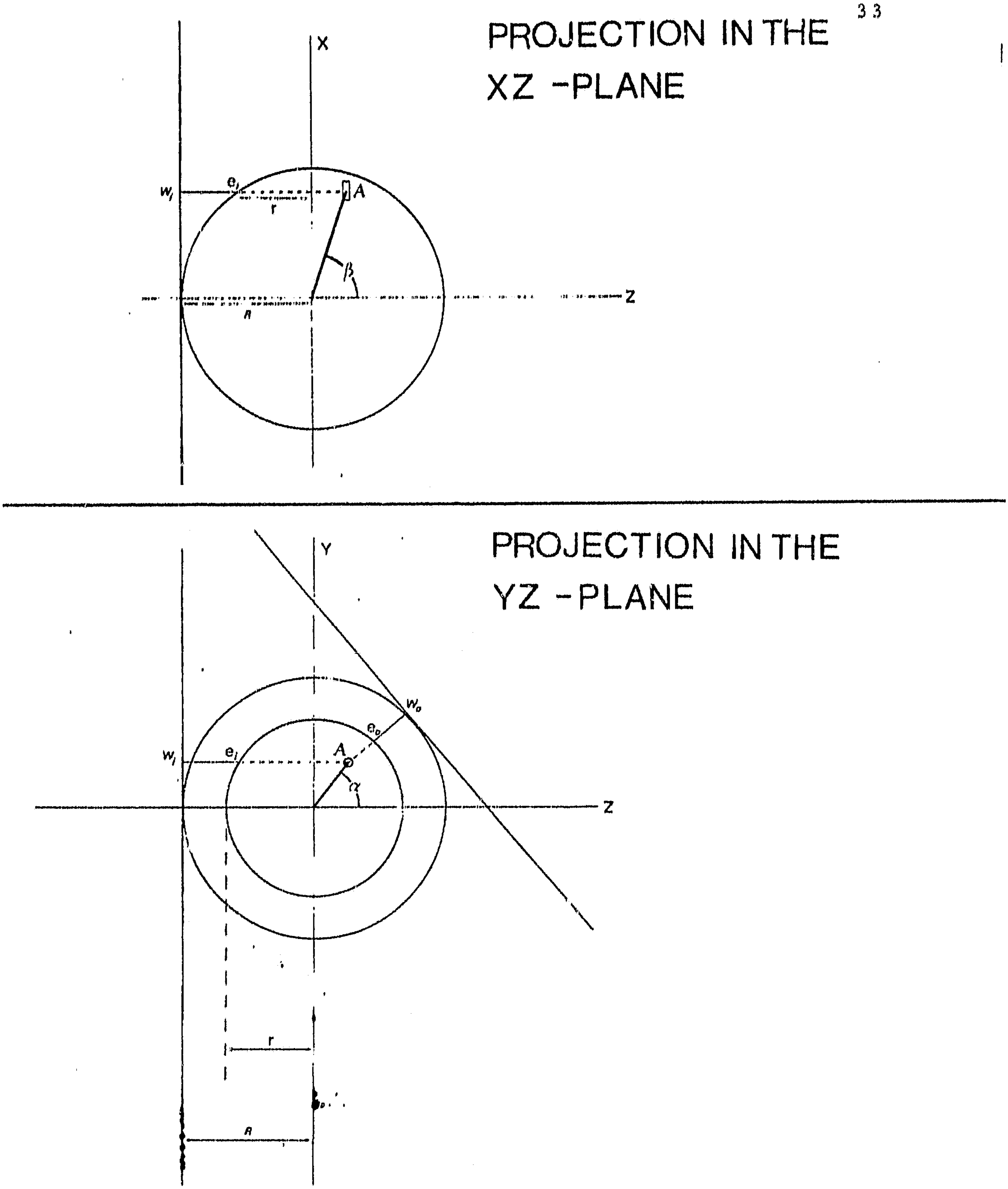

Fig. 3.1 The single scattering geometry. *A* is the location of the scattering cylinder with spherical coordinates D,α,β. Aw_i is the perpendicular distance between *A* and the incident wavefront tangent to the "bird-nest" with radius *R*. Aw_o is the perpendicular distance between *A* and an imaginary scattered wavefront tanget to the "bird's-nest".

ference pattern becomes increasingly constructive as the ensemble expands or N decreases. In the limit $m_{eq} \to 1$, eq. 3.14 becomes $\overline{O}_A = w_i A + A\overline{w}_o$. The position (D,α,β) of a cylinder can be written $(\mathrm{X}d,\alpha,\beta)$. Then

$$w_i A = R + \mathrm{X}d\cos(\beta)\cos(\alpha)$$

$$Aw_o = R - \mathrm{X}d\cos(\beta)\cos(\alpha - \theta), \tag{3.19}$$

and

$$PH = \mathrm{X}d\cos(\beta)(\cos(\alpha) - \cos(\alpha - \theta))\frac{2\pi}{\lambda} + ph_A \, . \tag{3.20}$$

It is seen that in this approximation the dependence of PH on α and β vanishes at $\theta = 0$, where the interference pattern depends only on ph, the phase shift over single cylinders. Eq. 3.20 can be rewritten

$$PH - ph_A = -\frac{4\pi \mathrm{X}d}{\lambda}\cos(\beta)\sin(\alpha - \tfrac{\theta}{2})\sin(\tfrac{\theta}{2}), \tag{3.21}$$

where it is seen that PH_A and therefore the phase differences and their dependence on α and θ are proportional to X and increase with θ.

3.7 Secondary Scattering Approximation

3.7.1 Intensity

In the previous section each cylinder was assumed to scatter the light incident on the agglomerate independently of all other cylinders. However, some of the light may be absorbed or scattered by other cylinders. This is the phenomenon of extinction represented by the imaginary part of the index or refraction. The thus scattered light will irradiate the cylinders from directions deviating from that of light incident on the agglomerate as a whole. However, we assume that the cylinders "look" infinite at a distance comparable to their length so that the cylinders are in effect irradiated at perpendicular incidence. Let I_A be the incident intensity on cylinder $A(D_A,\alpha_A,\beta_A)$, then the intensity I_B scattered of A and incident on cylinder $B(D_B,\alpha_B,\beta_B)$ approximated by the far--field solution is the cylindrical wave

$$I_B = \frac{I_A\ F(\varphi)(\ell - |D_A\sin(\beta_A) - D_B\sin(\beta_B)|)}{k\ \sqrt{D_A^2\cos^2(\beta_A) + D_B^2\cos^2(\beta_B) - 2D_A\cos(\beta_A)\,D_B\cos(\beta_B)\cos(\alpha_A - \alpha_B)}} \tag{3.22}$$

where ℓ is the length of the cylinders and φ is the angle between the direction of the incident radiation and the direction to B. The parenthesis in the numerator denotes the length of B illuminated by A (the perpendicular projection of A on B) if this is 0 or negative no secondary scattering is assumed to occur. The $I_{\shortparallel}$ element in $F(\varphi)$ varies only by 13% between $\varphi = 0^{\circ}$ and 180° (Fig.

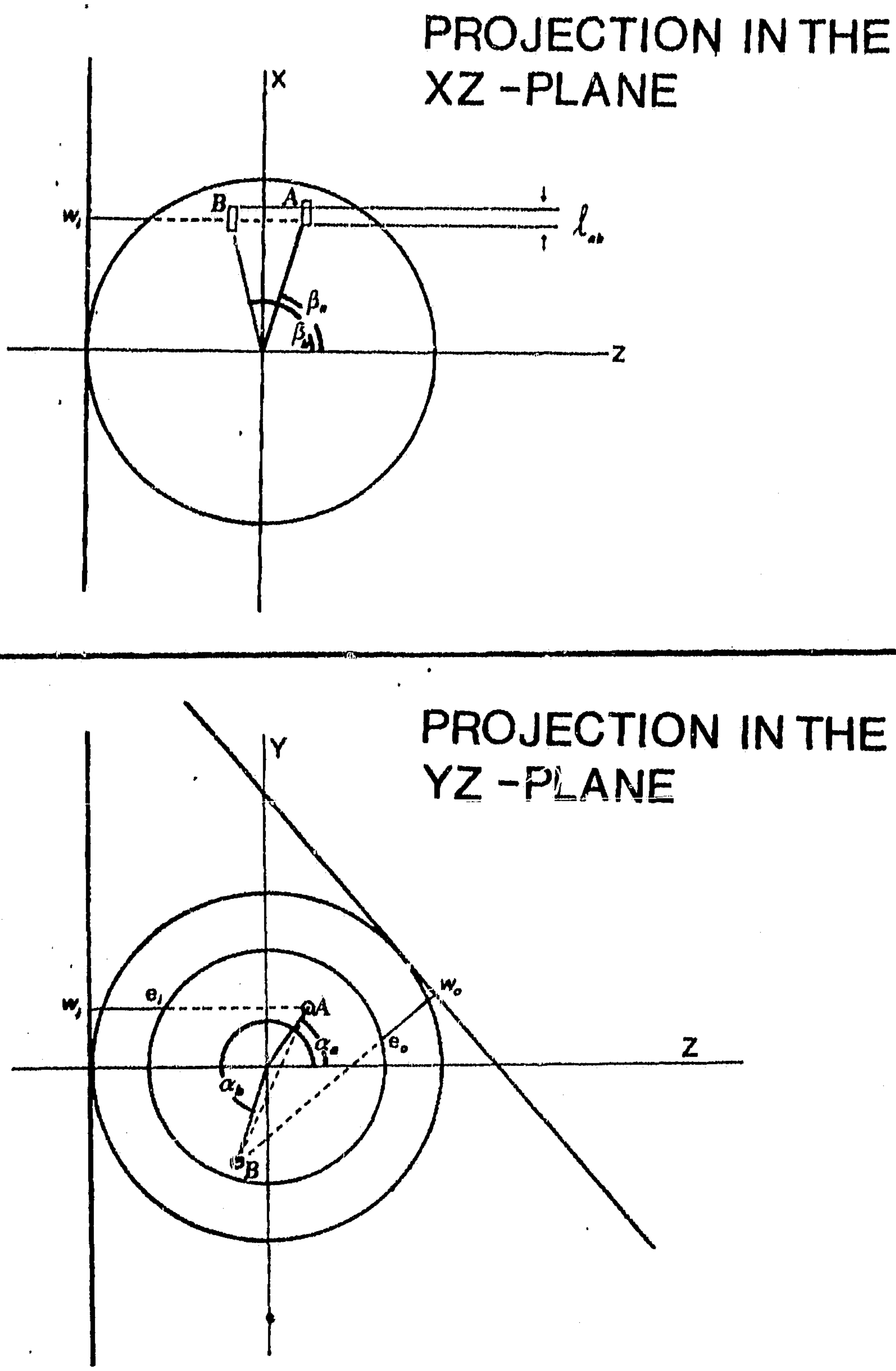

Fig. 3.2 The geometry for the secondary scattering approximation. The light is first scattered by *A* and then by *B*. In the secondary scattering approximation ℓ_{ab} is the length of *B* illuminated by *A*.

4.7) and to save computer core $F(\varphi)$ is approximated by the mean value 0.095 at all φ's. Also the phase function for cylinder B is approximated by this value. The intensity of the secondary scattering in I_1 is thus isotropic at the far field, at which the dimension of the "bird's-nest" can be neglected compared to the distance ρ to the observer. The intensity of the radiation first scattered off A and then off B is,

$$I_{AB} = \frac{I_B^F}{k\ \rho} \left(\ell - |D_A\sin(\beta_A) - D_B\sin(\beta_B)|\right) \tag{3.23}$$

3.7.2 Phase

The optical path is given by

$$\overline{AB} = m' \sqrt{D_A^2\cos^2(\beta_A) + D_B^2\cos^2(\beta_B) - 2D_A D_B\cos(\beta_A)\cos(\beta_B)\cos(\alpha_A - \alpha_B)} \tag{3.24}$$

where m' is the real part of the index of refraction as determined by eq. 3.1 or 3.2. The total phase shift is then;

$$PH = \frac{\overline{w_i A} + \overline{AB} + \overline{Bw_o}}{\lambda} 2\pi + ph_A + ph_B \tag{3.25}$$

where $ph_A = ph_B = ph$ is the phase shift due to the scattering by the cylinders. In the Rayleigh approximation $ph = 0^\circ$, while for spheres of the same size-parameter as the cylinders, Mie theory predicts ph close to 1.7° in I_1 at all θ's. $ph = 1.7^\circ$ is used in these computations.

Chapter 4

EXPERIMENTAL RESULTS
AND
VERIFICATION OF THE "INTERFERENCE" THEORY

4.1 Agglomerates of Homogeneous Cylinders

4.1.1 The single scattering approximation applied to T41A

T41A: 125 $x = 0.47$, 4:1 -elongation homogeneous cylinders aligned perpendicular to the scattering plane within an $X = 10.04$ sphere.

In the single scattering approximation the scattering from each cylinder is replaced by the Rayleigh approximation for an equal volume V prolate spheroid with the same elongation as the cylinders. The polarizability α_j along the major axis $j = 1$ and the minor axis $j = 2$ is given by

$$\frac{V}{4\alpha_j} = L_j + \frac{1}{m^2-1} \tag{4.1}$$

Let $e^2 = 1 - (b/a)^2$ where a and b are the length of the semi-major and -minor axes respectivly, then for the depolarization factors we have

$$L_1 = \frac{1-e^2}{e^2}\left(-1 + \frac{1}{2e}\ln\frac{1+e}{1-e}\right) \tag{4.2}$$

and

$$L_1 + 2L_2 = 1 \tag{4.3}$$

Using $b/a = 1/4$, it follows that:

$$\begin{aligned} L_1 &= 0.0754, \\ L_2 &= 0.4623. \end{aligned} \tag{4.4}$$

For details we refere to van de Hulst (1957, p. 70). Using the index of refraction ($m = 1.618 - 0.005i$) obtained from the larger casted cylinder (see sec. 2.6.1, p.19) in eq. 4.1 we obtain:

$$\alpha_1 = 0.02596 - 0.00023i,$$
$$\alpha_2 = 0.01666 - 0.00010i. \qquad (4.5)$$

The scattered field entering in eq. 3.9 is obtained from the scattering tensor:

$$\begin{bmatrix} S_2 & S_3 \\ S_4 & S_1 \end{bmatrix} = ik^3 \begin{bmatrix} \alpha_2 \cos(\theta) & 0 \\ 0 & \alpha_1 \end{bmatrix} \qquad (4.6)$$

The cylinders are embedded in the expanded polystyrene matrix material with index of refraction m_0 (assumed real). The mean index of refraction m_{eq} of the ensemble used to compute the optical path of light travelling inside the "bird's-nest" is given by eq. 3.1 and may be written

$$m_{eq} = m_0 + 2\pi P. \qquad (4.7)$$

The dipole moments P per unit volume for the electric vector parallel (11) and perpendicular (22) to the aligned particle axes are given by

$$P_{11} = N \frac{V}{\left(L_1 + \frac{1}{m^2-1}\right) 4\pi} V_{ens}^{-1}$$
$$P_{22} = N \frac{V}{\left(L_2 + \frac{1}{m^2-1}\right) 4\pi} V_{ens}^{-1} \qquad (4.8)$$

where V_{ens} is the volume of the ensemble.

Using the computed values of P for radiation polarized parallel and perpendicular to the spheroid axis, we finde

$$m'_{11} = m_0 + 0.060, \qquad m''_{11} \approx 5 \cdot 10^{-4},$$
$$m'_{22} = m_0 + 0.038, \qquad m''_{22} \approx 2 \cdot 10^{-4} \qquad (4.9)$$

As expected, $m'' \ll m'-1$ so that the ensemble material acts like a dielectric. The scattered intensity given by eq. 3.9 is dependent on the orientation of the ensemble (defined by the angle χ, see sec. 2.4). The details of this scattering pattern depends on the exact location of the individual cylinders. In the theoretical target the cylinders were distributed using a random number generator, whereas in the experimental target each particle was inserted by hand in as close an approximation to randomness as possible. The resulting χ -dependence given by the theory (Fig. 4.1) and the experiment (Fig. 4.2) are therefore seen to differ in detail but to show the same over-all characteristics. The run of the standard deviation $\sigma_{ij}(\theta)$ of the scattered radiation $I_{ij}(\theta)$, normalized to $I_{ij}(\theta)$ is a measure of the isotropy of the optical properties of the scatterer. The ratio $\sigma_{ij}(\theta)/I_{ij}(\theta)$ is independent of the gain of the apparatus and is likely to contain extensive information about the internal structure and shape of particles. The predicted and measured run of σ_{ij}/I_{ij} with θ are compared in Figs. 4.9 ($i=j=1$) and 4.10 ($i=j=2$). To simulate a cloud of similar agglomerates, the scattered intensity at each scattering angle was averaged over 72 orientations. The resulting angular distribution from both experiment and theory is shown in Figs. 4.3 and 4.4 for radiation polarized along the cylinder axes (perpendicular to the scattering plane) and perpendicular to the cylinder axes (in the scattering plane) respectivly. The Fraunhofer diffraction pattern which is confined to the forward scattering hemisphere, and expected to dominate for larger agglomerates at small scattering angles is still seen and well represented by Mie-theory, although the size of the ensemble is as small as $X = 10.04$.

If we replace the finite cylinders by equal length portions of infinite cylinders in the theoretical solution, the magnitude of the scattered intensity is increased by a factor ≈ 3 (Figs. 4.5 and 4.6) because the scattering by an infinite cylinder is concentrated precisely in the scattering cone while the scattering by a finite cylinder is spread by diffraction (Lind, 1966, Greenberg, 1974). In this case eq. 3.2 was used to compute m_{eq}. The shape of the angular distribution is quite similar. When the scattering tensor entering in eq. 3.9 was replaced by the exact solution for infinite cylinders normalized to the Rayleigh approximation for spheroids (eq. 4.6), the solution using the Rayleigh approximation alone was closely reproduced but the experimental values were further approached. This was expected as a comparison between the shape of the scattering from the cylinder to the Rayleigh approximation (Fig. 4.7) illustrates the well-known fact that back-scattering is overestimated in the Rayleigh approximation.

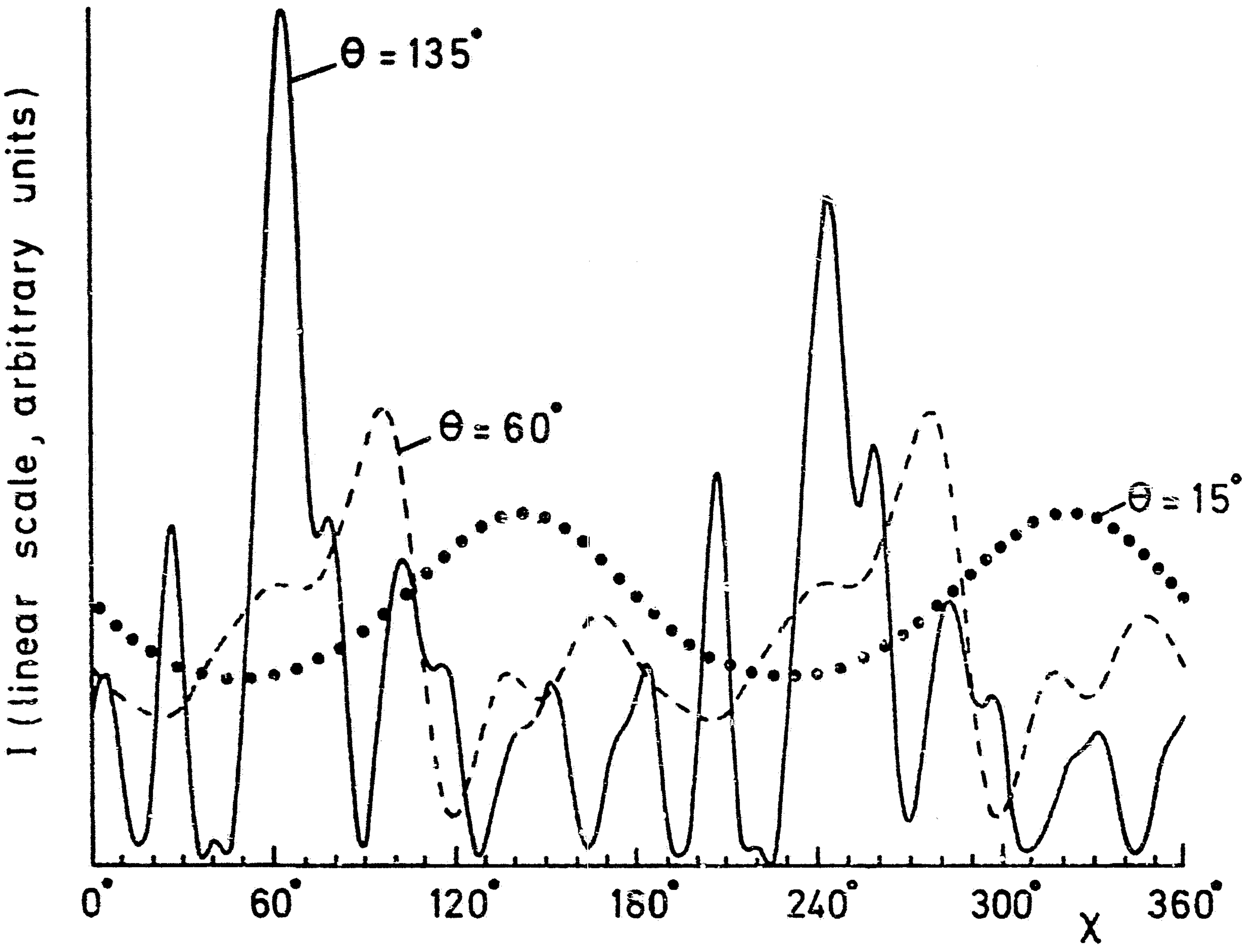

Fig. 4.1 Mathematical simulation of variation of scattering by the spherical ensemble T4[illegible] scatterers (x = 0.47 aligned cylinders) as the ensemble is ro[illegible] at various scattering angles θ.

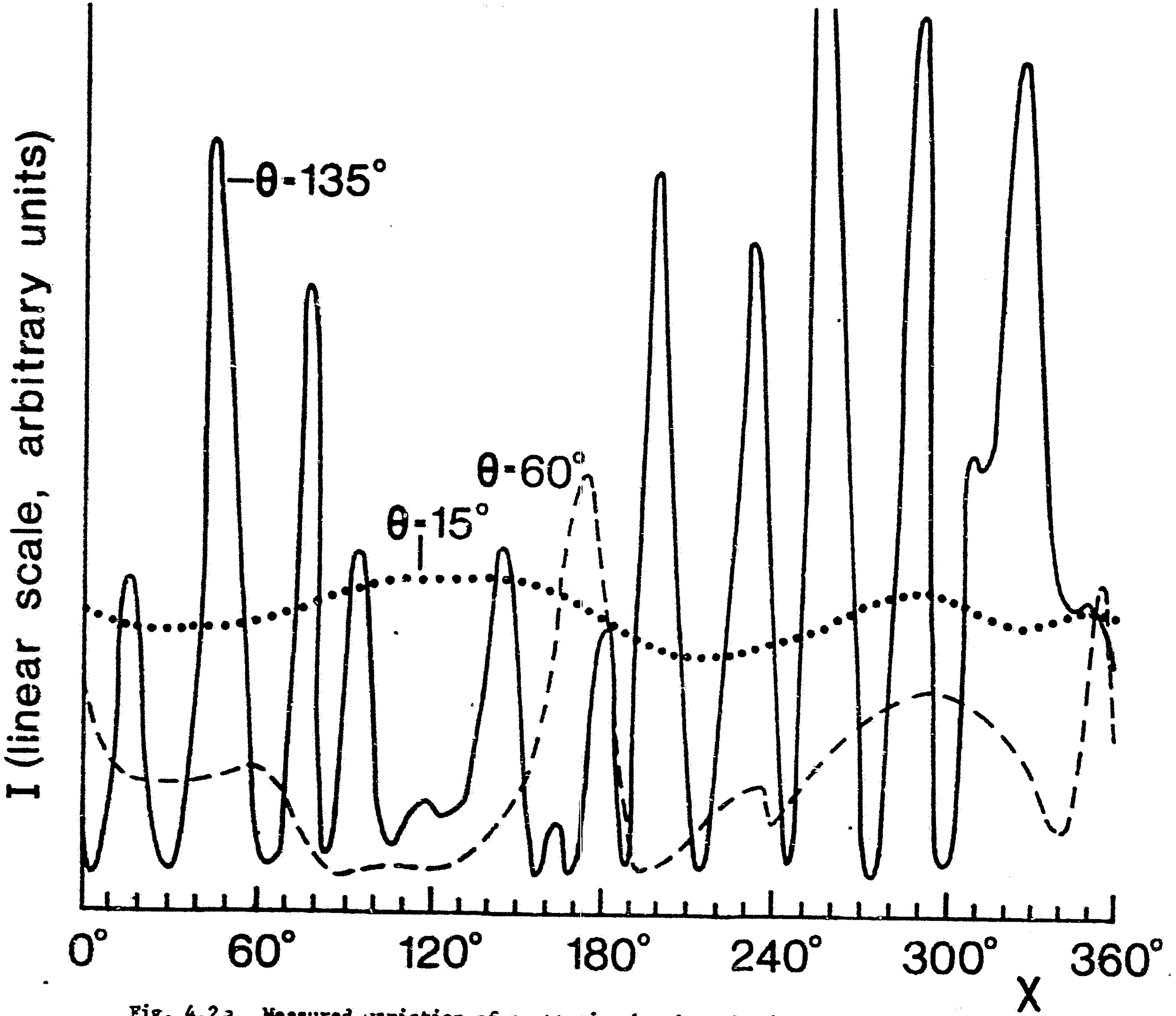

Fig. 4.2a Measured variation of scattering by the spherical ensemble T21R consisting of 240, 2:1 -elongation, randomly orientated cylinders, as the ensemble is rotated in azimuth about an axis: at various scattering angles θ.

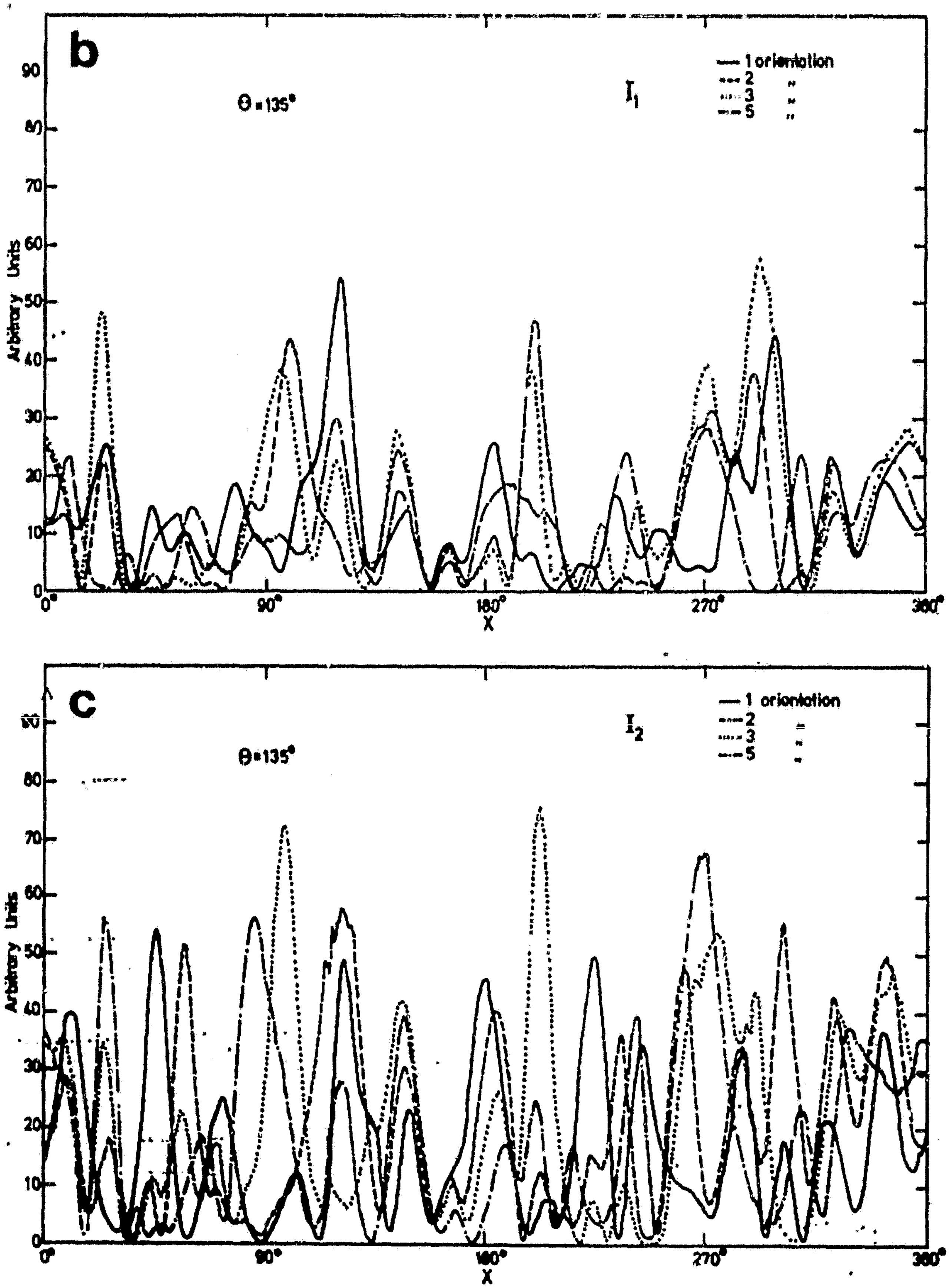

Fig. 4.2b and c Scattering intensity versus azimuthal angle for an ensemble of randomly aligned x = 0.47 acrylic cylinders (m = 1.61) with elongation 2:1. The cylinders are distributed within a "sphere" of radius 5.0 cm which is rotated about different axes.

b) I_1 = intensity for incident and received radiation polarized perpendicular to the scattering plane.

c) I_2 = intensity for incident and received radiation polarized parallel to the scattering plane.

4.1.2 The secondary scattering by T41A.

The secondary-scattering approximation derived in sec. 3.7 assumes that the near field around a scattering cylinder can be approximated by the far-field solution. It is seen from Fig. 4.5 that the secondary scattered intensity is overestimated by this approach. This conclusion is further supported by the fact that we see the deep dip in f_{22} around 90^0 that would tend to be filled in by multiple scattering. Note that the laboratory has a finite angular resolution.

4.1.3 Remarks and conclusions for T41A.

The individual cylinders have mirror symmetry in the scattering plane and thus do not by them self give rise to cross-polarization. The "bird's-nest" does not possess such symmetry, but the cross-polarization components were too small to be detected in the laboratory (< 1). In analogy to extinction by a very large object, such as an apple in visual light, the extinction cross section in the far field (twice the geometrical cross section for the apple) seems to be larger than in the near field (once the geometrical cross section). We thus tend to over-estimate the importance of multiple scattering. The single-scattering approximation however seems to satisfactory reproduce the experiment especially in the back-scattering hemisphere. At small scattering angles, Mie-theory (-Fraunhofer diffraction) gradually becomes a better approximation. The degree of polarization shown in Fig. 4.8 exhibits a number of oscillations at $\theta < 90^0$ that are attributed to the birefringent character of the ensemble.

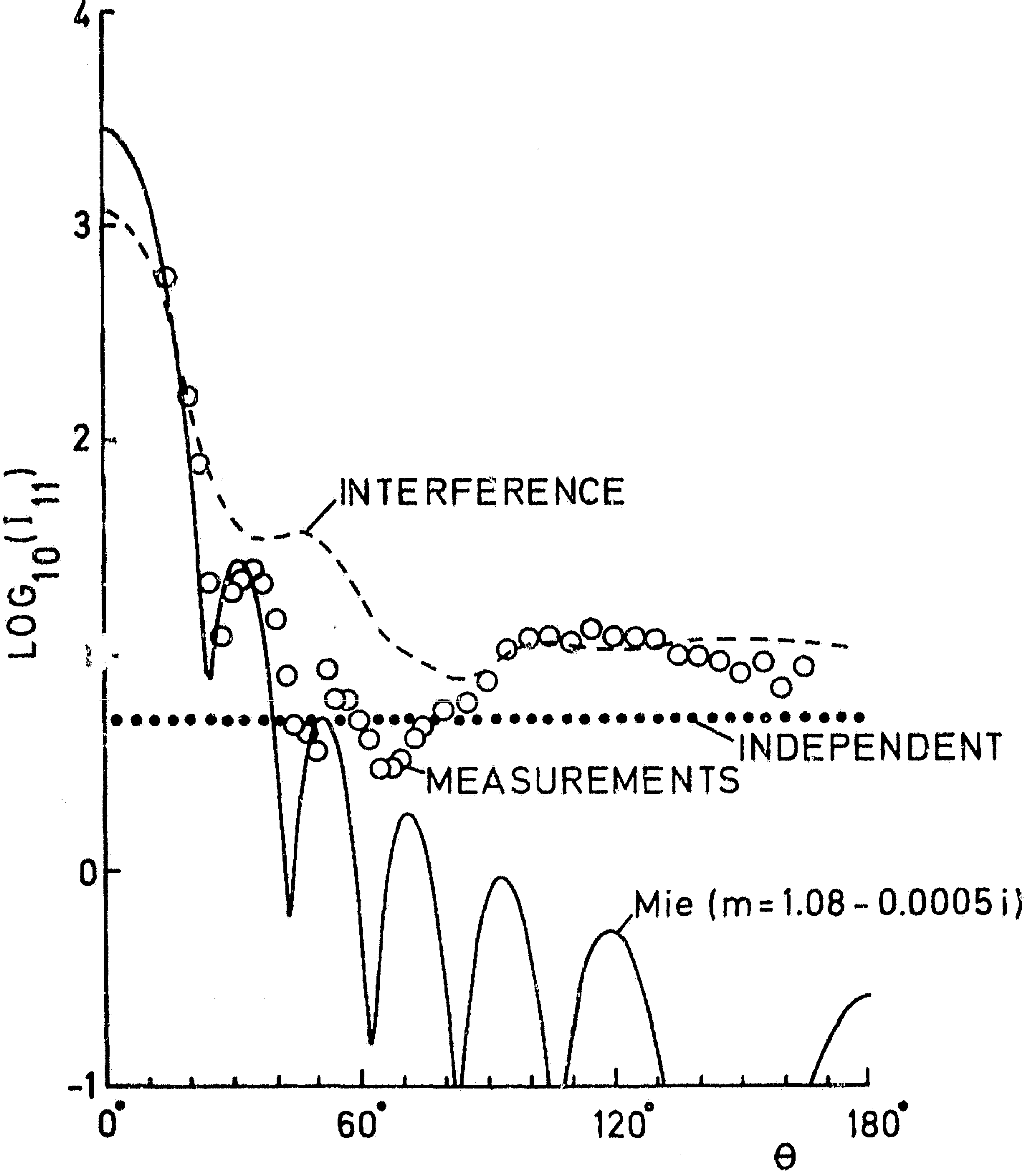

Fig. 4.3 Theoretical and experimental intensities versus scattering angle for the ensemble T41A of 4:1 elongation aligned cylindrical particles with size parameter $2\pi a/\lambda = 0.47$. I_{11} is the intensity for radiation polarized perpendicular to the scattering plane. Dotted curve is the arithmetic sum of individual particle scattering intensities; solid curve is the Mie theory result for the ensemble treated as a homogeneous sphere with an equivalent index of refraction (see Equations 4.7 - 4.9); dashed curve is for the ensemble scattering treated coherently and averaged statistically using the single scattering, "interference" approximation (see text for explanation) the scattering by individual cylinders has been approximated by that of equal volume spheriods using the Rayleigh approximation; circles are the experimental results.

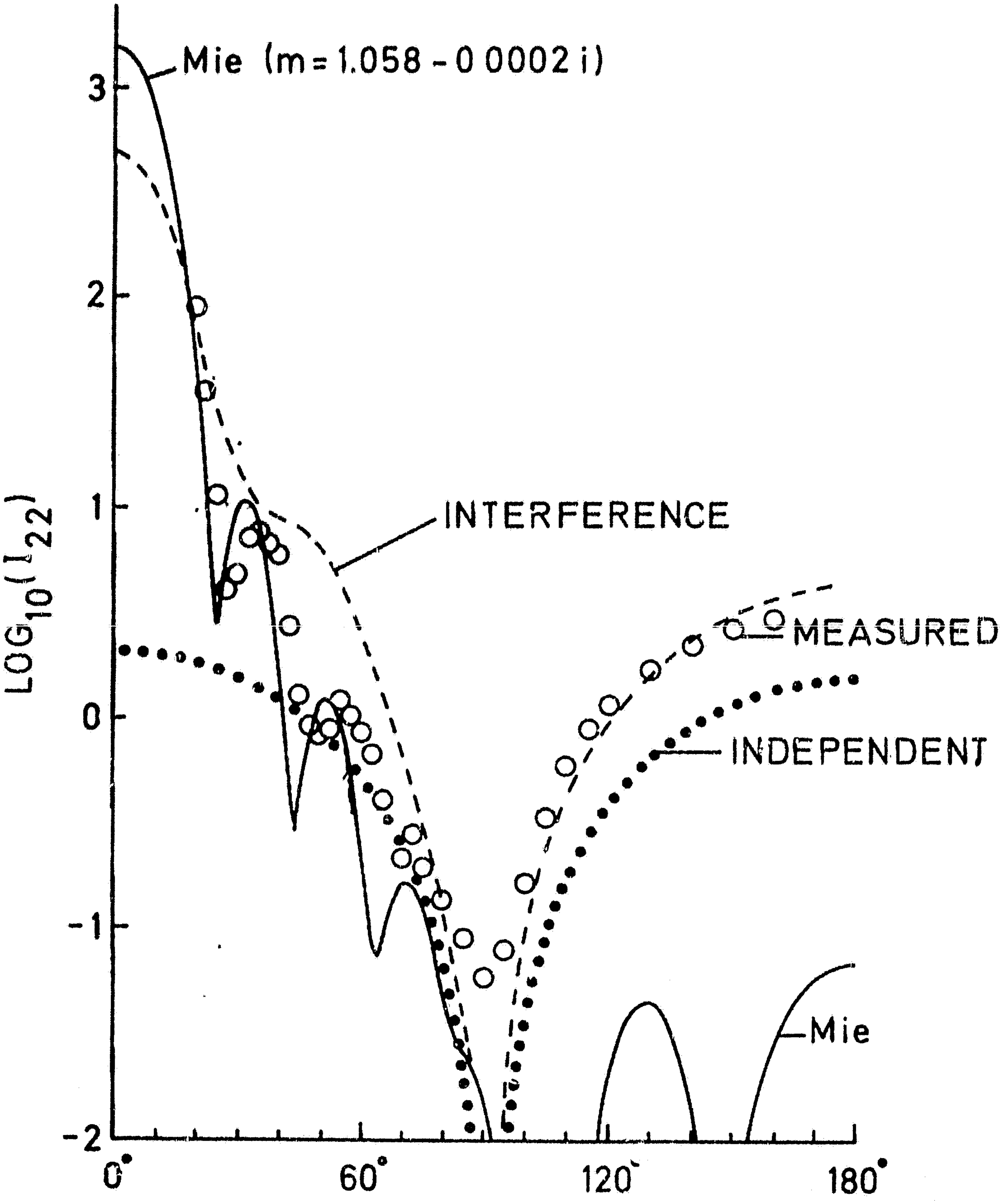

Fig. 4.4 Same as Fig. 4.3 except I_{22} is the intensity for radiation polarized in the scattering plane.

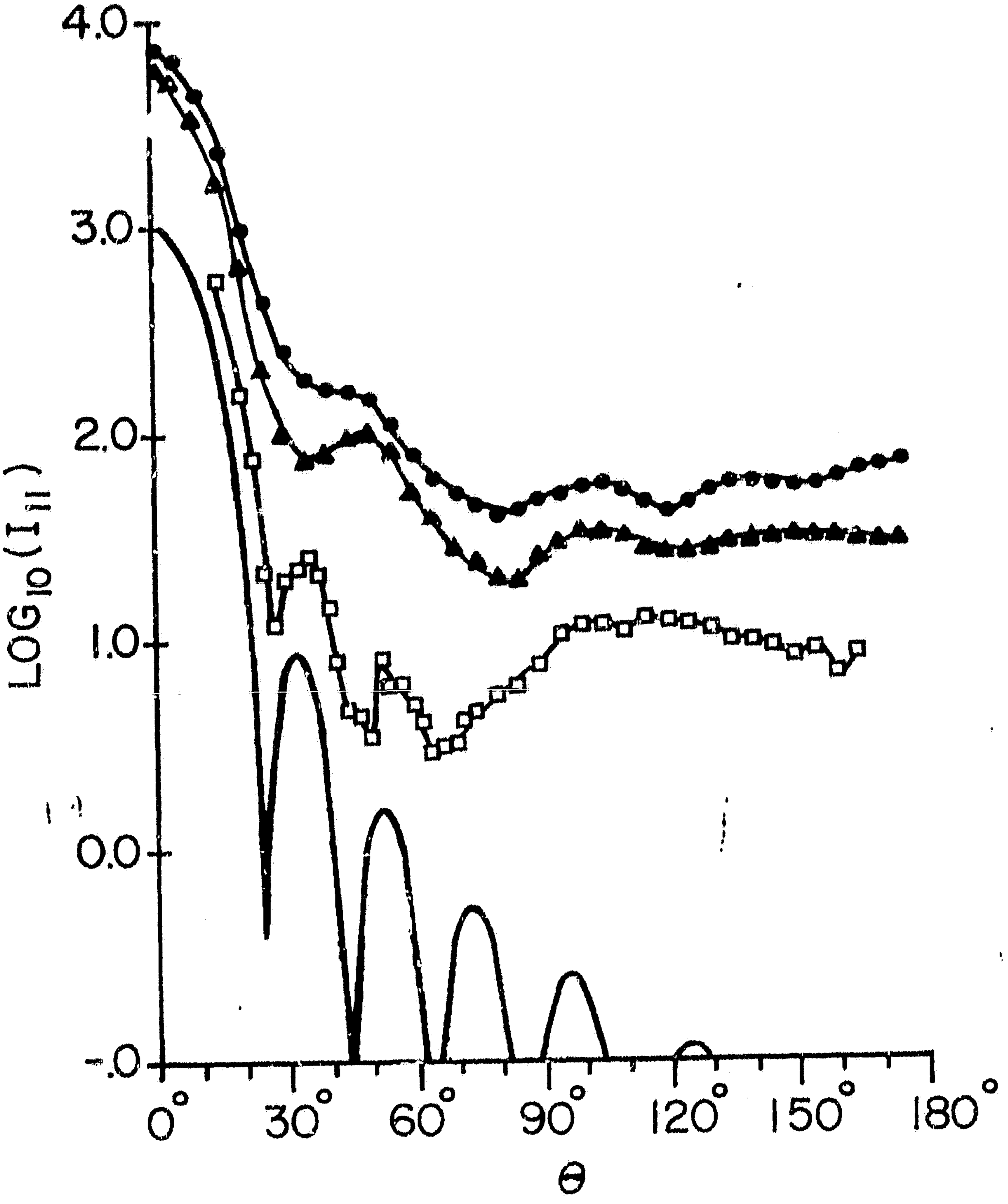

Fig. 4.5 Same as Fig.4.3 except in the theoretical computations the finite cylinders are approximated by equal length portions of infinite cylinders. The dots includes the secondary scattering approximation, triangles are the single scattering approximation and the solid curve the mie-computations using an index refraction given by eq. 3.2. Squares are the experimental results.

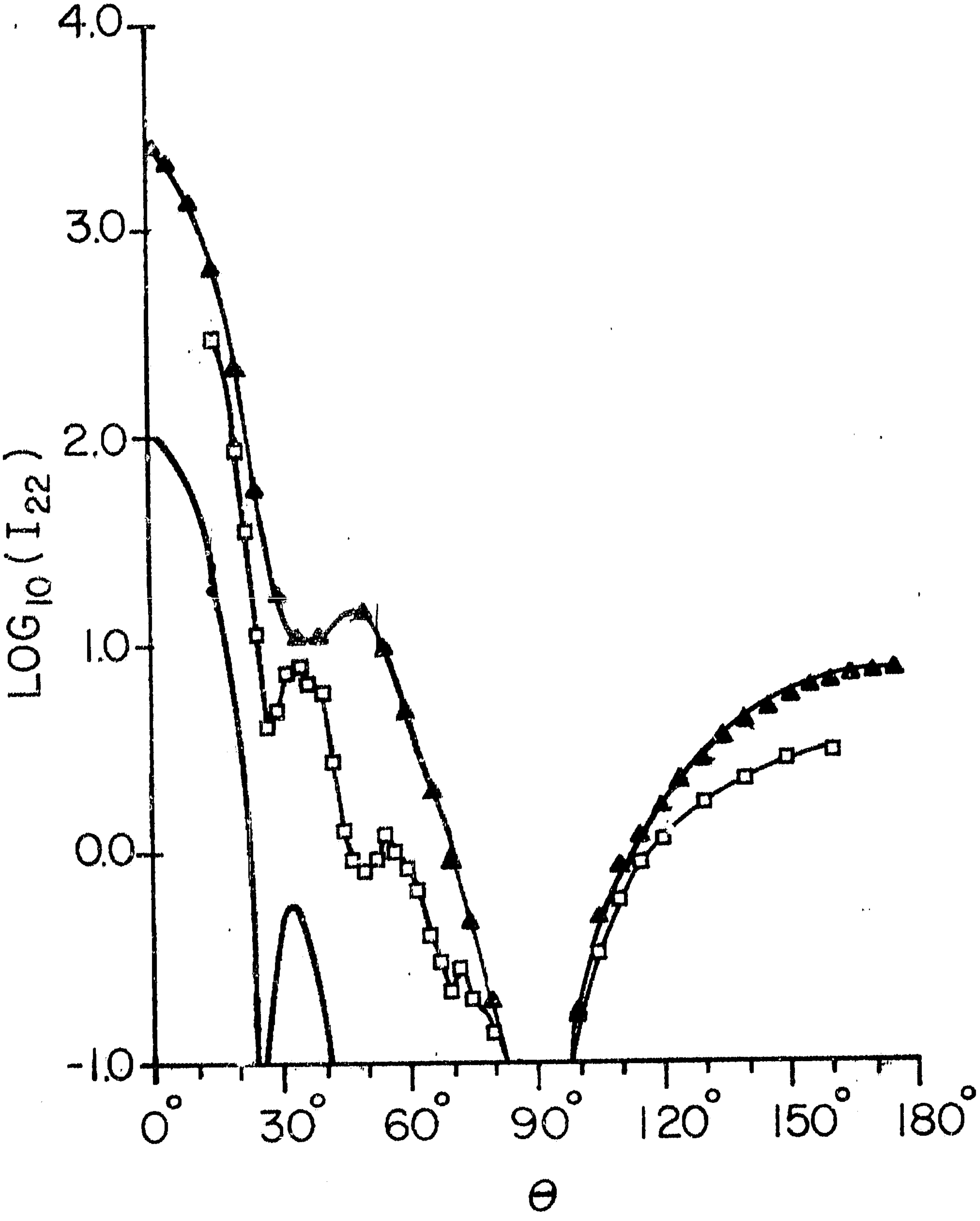

Fig. 4.6 Same as Fig. 4.5 except I_{22} is the intensity for radiation polarized in the scattering plane.

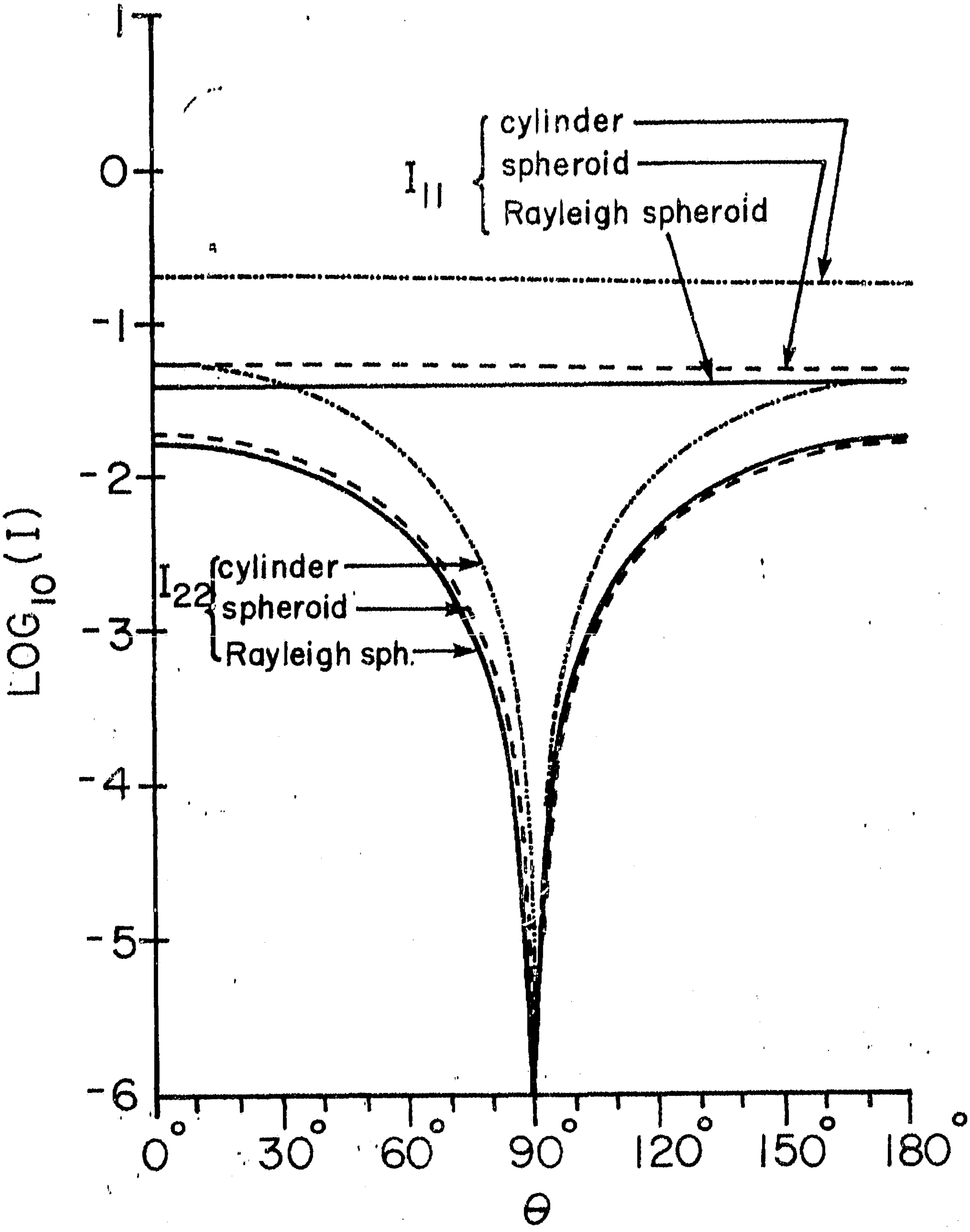

Fig. 4.7 Theoretical intensities versus scattering angle used to approximate the scattering by the finite cylinders at perpendicular incidence making up the ensemble T41A. For comparison the exact solution for the spheriod was computed using a computer code provided by R. Schaefer for details we refer to R. Schaefer, 1980.

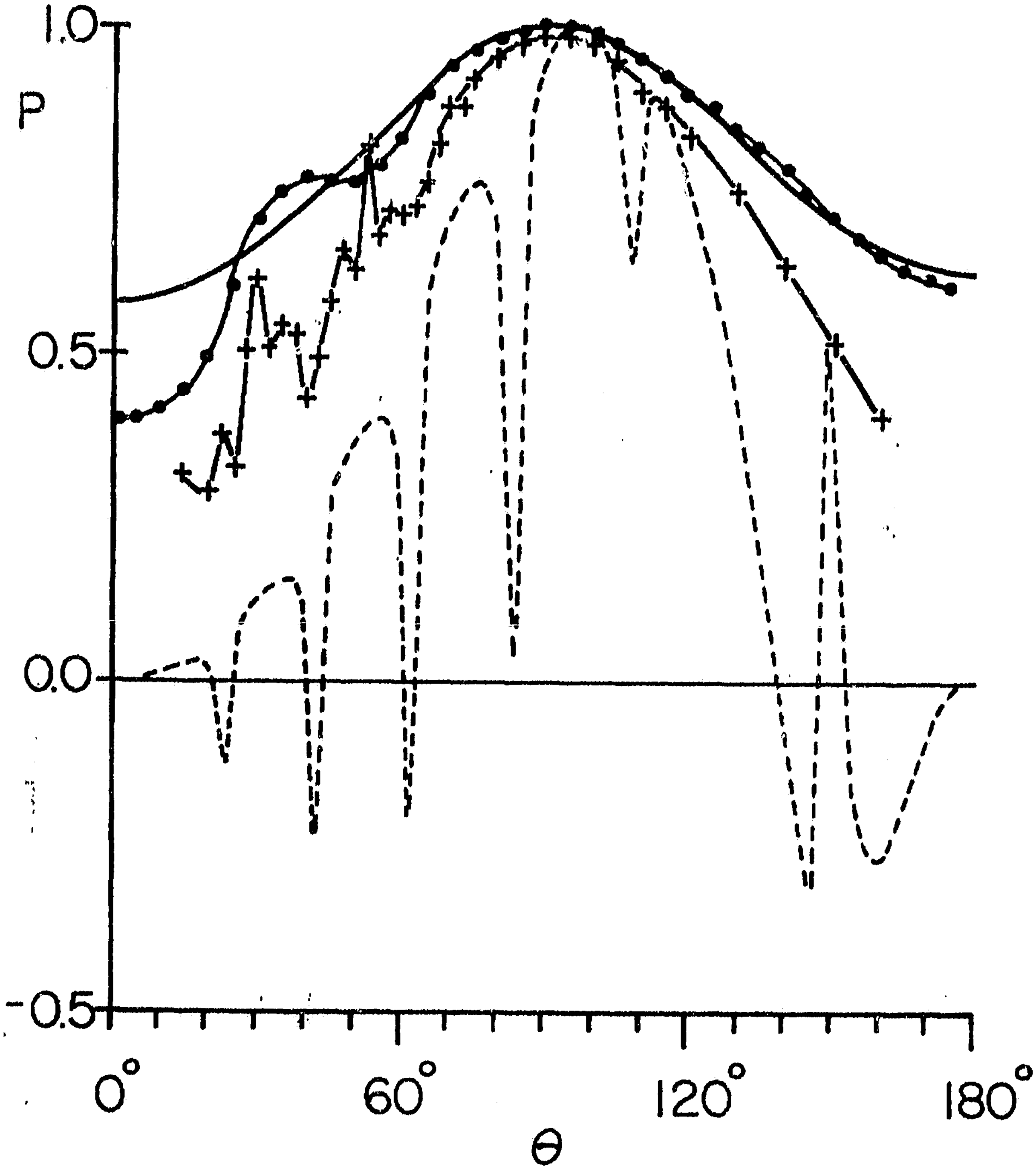

Fig. 4.8 Theoretical and experimental degree of polarization versus scattering angle for the ensemble T41A composed of 125, 4:1 elongation aligned cylinders. Solid curve is the arithmetic sum of scattering by individual particles; dashed curve is the Mie theory result for the ensemble treated as a sphere with a corresponding *isotropic* index of refraction obtained through eq. 3.12 dots are for the ensemble scattering approximated by the single scattering "interference" theory (see text for explanation) the cylinders have been approximated by equal volume Rayleigh spheroids; crosses are the experimental results.

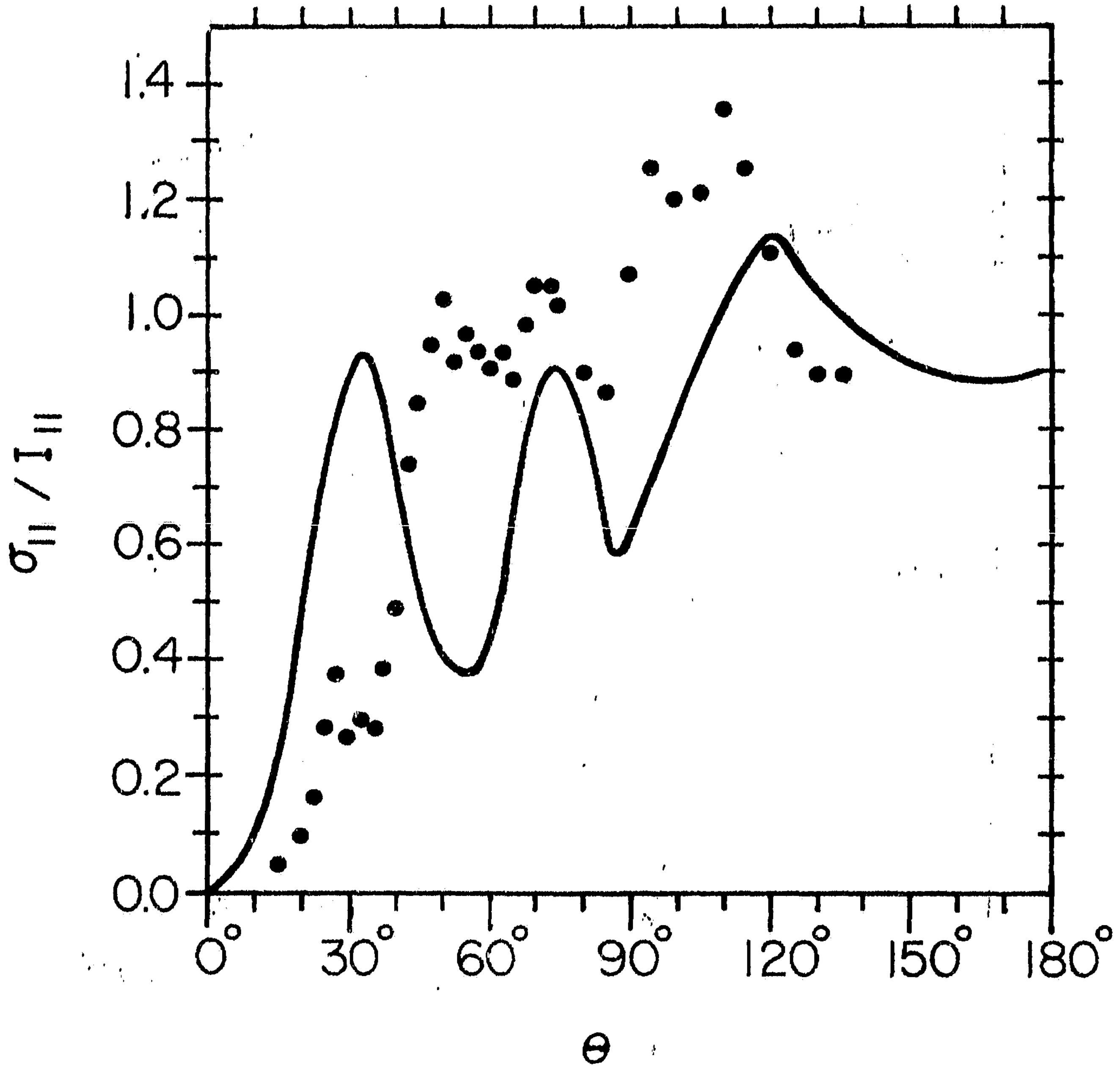

Fig. 4.9 Theoretical (solid line) and experimental (dots) normalized standard deviation of scattered intensity versus scattering angle from the ensemble T41A of 125, x = 0.47 aligned 4:1 elongation cylinders as the ensemble is rotated in azimuth. I_{11} is the intensity for radiation polarized perpendicular to the scattering plane.

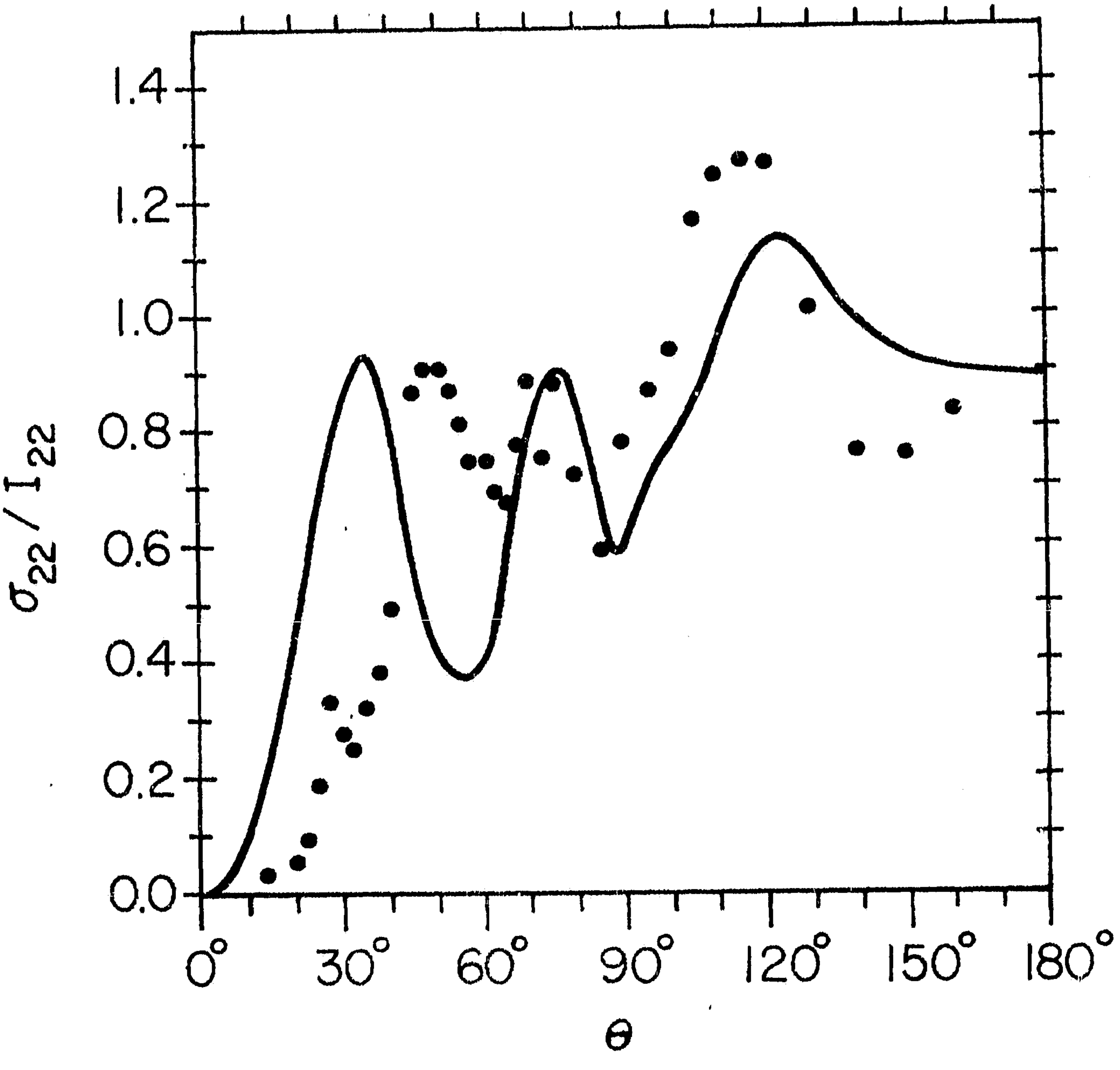

Fig. 4.10 Same as Fig. 4.9 except I_{22} is the intensity for radiation polarized in the scattering plane.

4.1.4 Scattering from P11, a two dimensional "bird's-nest"

P11: 156, $x = 0.47$, 1:1 -elongation homogeneous lucite cylinders randomly aligned within an $X = 19.76$ circular disc.

The scattering of each cylinder can be closely approximated by that of a single dipole. The simple geometry of the ensemble yield well separated predictions by single, multiple and by dependent scattering approximations.

Target P11 was first orientated such that the plane containing the scatterers was perpendicular to the scattering plane. The azimuth angle χ refers to the angle between the plane of the targets and the incident $\vec{k}_o$ vector (see Fig. 4.11).

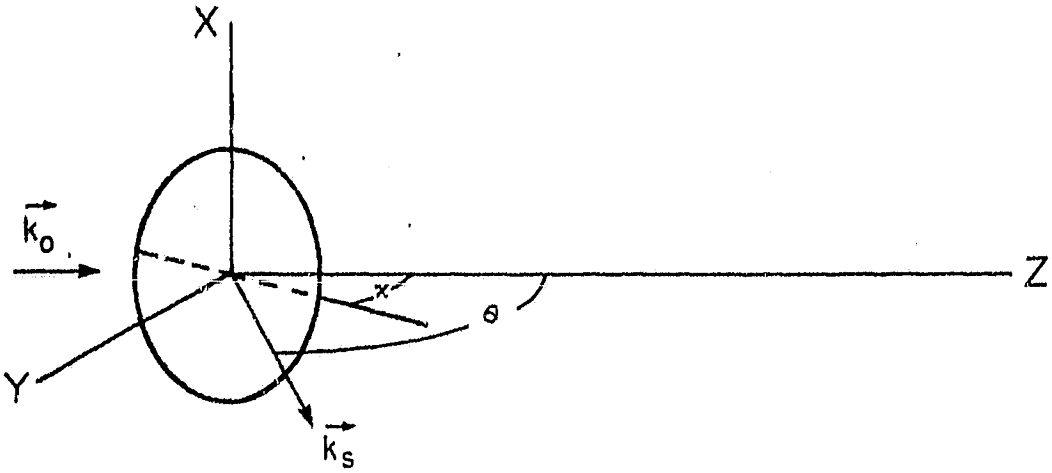

Fig. 4.11 Orientation of target P11 during measurements presented in Figs. 4.12 and 4.13. The plane containing the scatterers is perpendicular to the scattering plane $\vec{k}_o\vec{k}_s$ (YZ), χ is the angle in the scattering plane between the incident radiation $\vec{k}_o$ and the plane containing the scatterers.

In Fig. 4.12, the averages $\overline{I}_{11}(\chi)$ and $\overline{I}_{22}(\chi)$ over ψ are represented by the solid and dashed curves, respectively, at $\theta = 45^\circ$ and the same quantities at $\theta = 90^\circ$ are shown in Fig. 4.13. We see that in all cases a maximum occures at $\chi = \theta/2$. At this orientation, $\vec{k}_o\hat{n} = \vec{k}_s\hat{n}$ where n is the normal to the plane containing the scatterers. This is the well known condition for reflection from an infinite plane. As the plane is finite in our case, we expect interference patterns which simply correspond to the diffraction pattern that would be observed if the plane was homogeneous. The scattering pattern is therefore symmetrical around the maximum. At $\theta = 90^\circ$, the individual cylinders have a very sharp dip in I_{22}. Thus, observations of $I_{22}(\chi)$ at $\theta = 90^\circ$ yield information about the importance of multiple and dependent scattering. The $\chi = \theta/2$ orientation corresponds to the Brewster angle of an infinite plane. Thus, rather than the maximum at this orientation being seen for I_{11}, dependent scattering predicts a minimum in I_{22}. Dependent and multiple scattering are also expected to give rise to cross-polarization when the agglomerate does not possess mirror symmetry in the scattering plane. This occurs when the plane of the scatterers deviates from the scattering plane and does not contain the perpendicular to this plane. Significant cross-polarization could not be detected at any orientation, and it is seen in Fig. 4.13 that there is no dip in the I_{22} component at $\chi = 45^\circ$ and $\theta = 90^\circ$. We conclude that multiple and dependent scattering are much weaker than single scattering for this target.

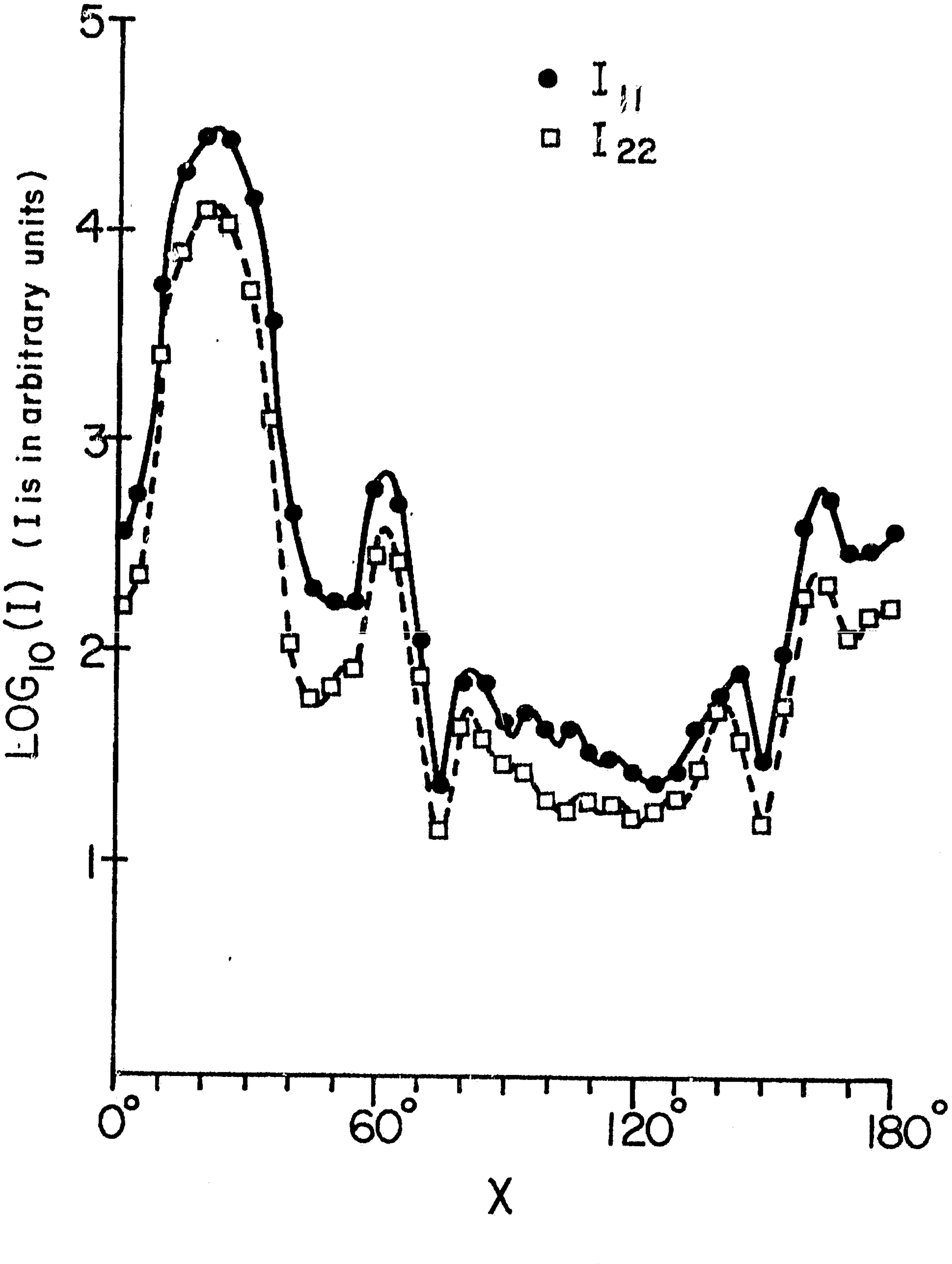

Fig. 4.12 Scattering averaged over Ψ at θ = 45° by the two dimensional ensemble of scatterers P11 shown in Fig. 4.11 as the ensemble is rotated in azimuth around the *X*-axis, solid curve is the I_{11} component of scattered intensity; dashed curve is the I_{22} component.

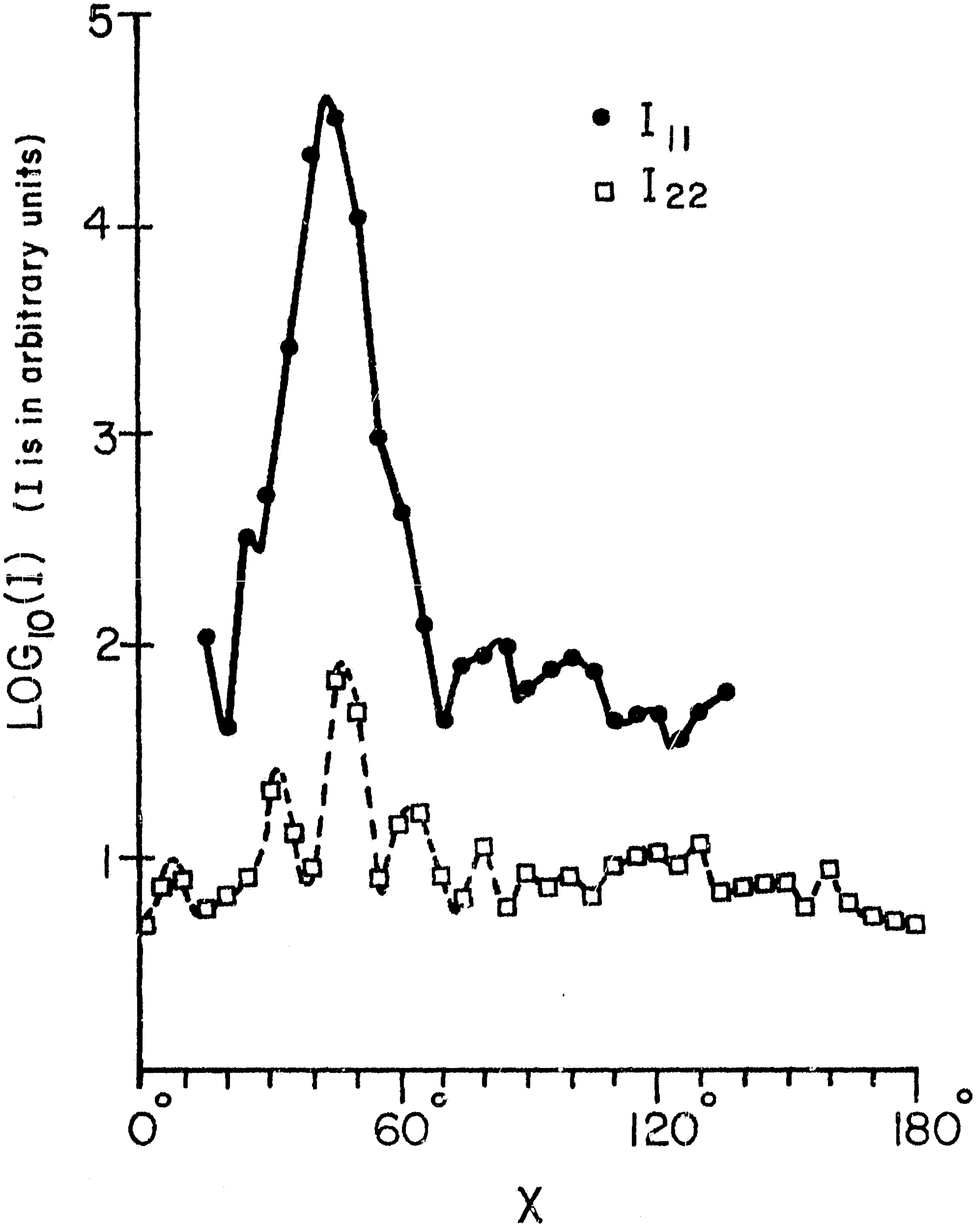

Fig. 4.13 Same as Fig. 4.12 except $\theta = 90^{\circ}$.

4.1.5 Scattering from U41A and C41

U41A: 43, x = 1.88, 4:1 -elongation homogeneous cylinders aligned parallel to each other within an X = 25.09 sphere.

C41: 1, x = 1.88, 4:1 -elongation homogeneous cylinder.

The differences between T41A and U41A are:

I) The cylinder size parameter x has been increased a factor 4, such that scattering from the individual cylinder C41 could be detected in the laboratory.

II) The "bird's-nest" size parameter X has been increased a factor 2.5.

III) The average polarizability per unit volume as determined by eq. 3.1, is increased by fitting 43 cylinders into the "bird's-nest" rather than 30.5 in the same volume.

It is evident from Fig. 4.14 that the ensemble does not act like a sum of the individual cylinders. The scattered intensity per cylinder is much lower for the agglomerated cylinders than for independent identical cylinders C41A in the range of θ covered by the experiment. A sharp rise in both I_{11} and I_{22} is expected both from constructive interference and from Fraunhofer diffraction at smaller θ's. This target seems to be well suited for investigation of multiple and/or dependent scattering effects that may have flattened out the angular distribution. As a result, the run of the degree of polarization with θ (Fig. 4.15) is flatter and generally lower than for individual cylinders. In an attempt to separate an eventual enchancement in I_{11} independent of the cylinder orientations, U41A was aligned such that the cylinder axes were parallel to the scattering plane ($\psi = 90^{\circ}$) and $\chi = 60^{\circ}$. The resulting angular distribution of the scattered light (Fig. 4.16b) has a double peak in I_{11} around $\theta = 100^{\circ}$ whereas a single peak can be seen in I_{22}. However, the observed peaks are much too weak to fill in the dip in I_{11} at perpendicular incidence and $\theta \approx 105^{\circ}$. For comparison the scattering by the similarly orientated single cylinder C41 identical to the 43 cylinders in U41A is shown in Fig. 4.16a. We note that the peak around $\theta = 2\chi = 120^{\circ}$ characteristic of elongated targets, has almost vanished for the spherical ensemble.

In conclusion, it seems probable that the scattering by the ensemble is smoothed out by multiple scattering with respect to that by individual cylinders.

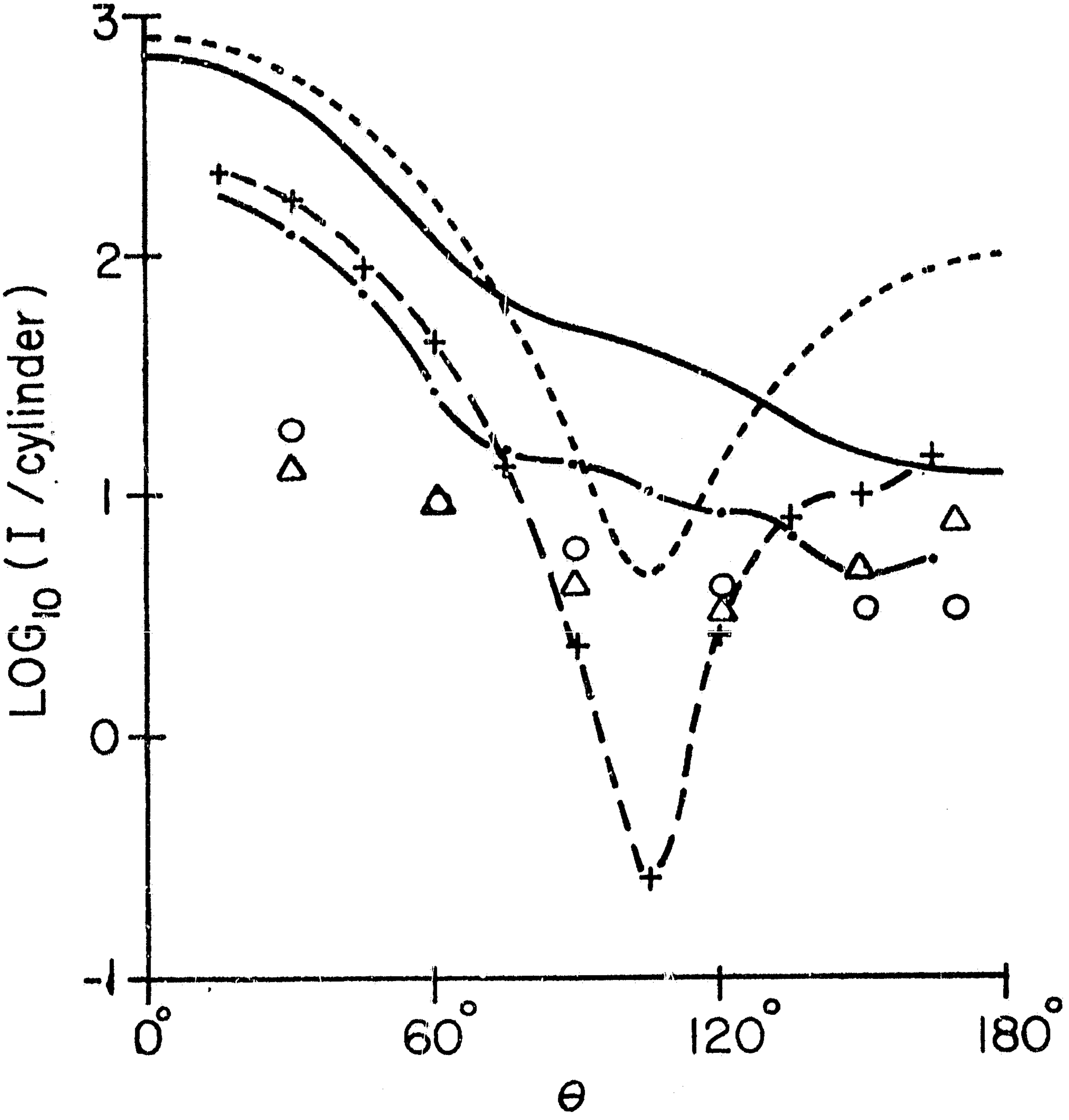

Fig. 4.14 Intensities per cylinder versus scattering angle for x = 1.88 cylinders. Dashed and solid curves are respectively computed I_1 and I_2 components for a 4:1 portion of an infinite cylinder at perpendicular incidence. For a similarly orientated single 4:1 -elongation cylinder crosses and dots are the experimental values for I_{11} and I_{22} respectively. The triangles are the experimental I_{11} component for the ensemble U41A, circles the I_{22} component.

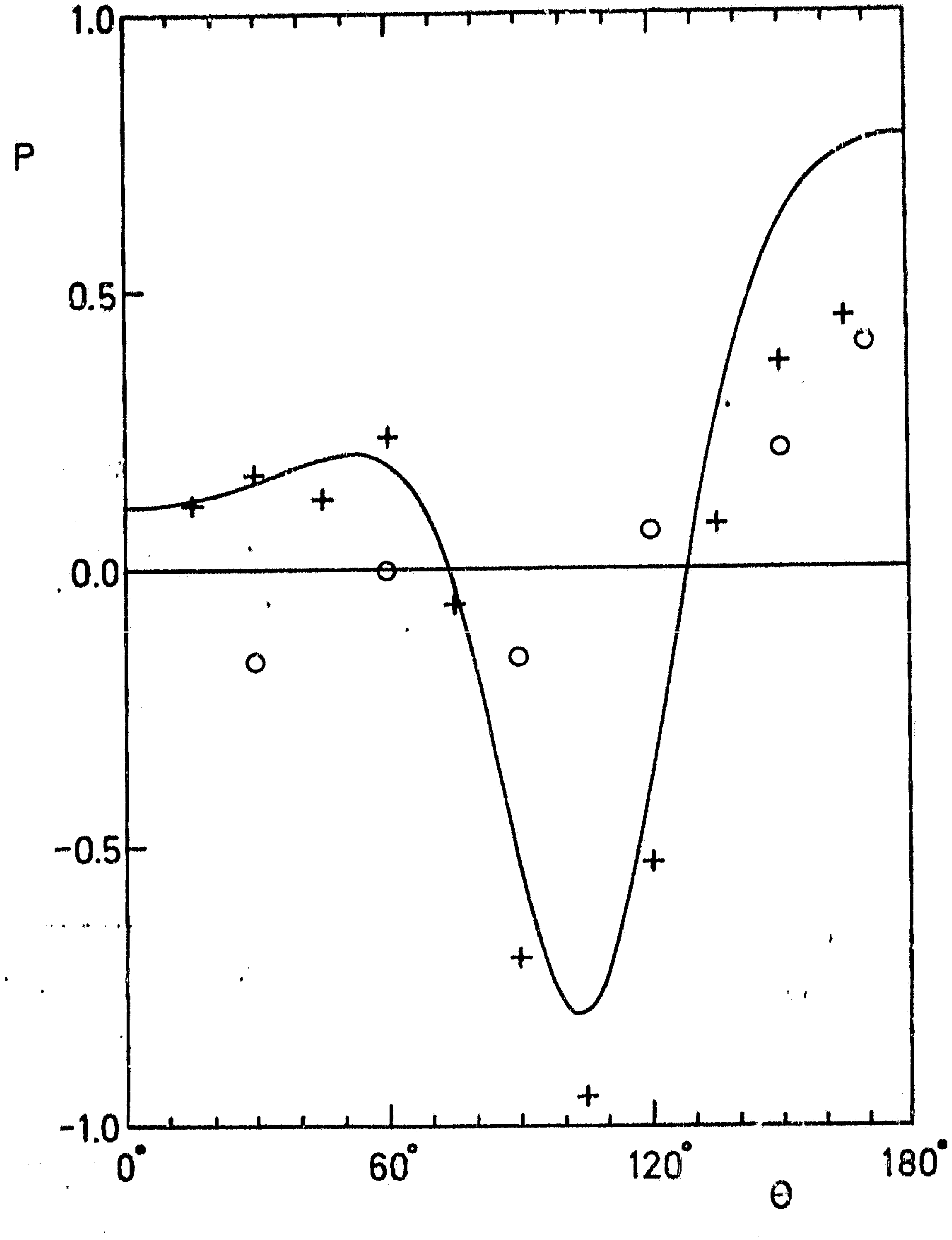

Fig. 4.15 Degree of polarization versus scattering angle for $x =$ [illegible].88 cylinders. Solid curve is computed for an infinite cylinder at perpendicular incidence. Experimental results are: pluses = single 4:1 cylinder at normal incidence (target C41A), circles are for the ensemble U41A of 43 aligned 4:1 cylinders.

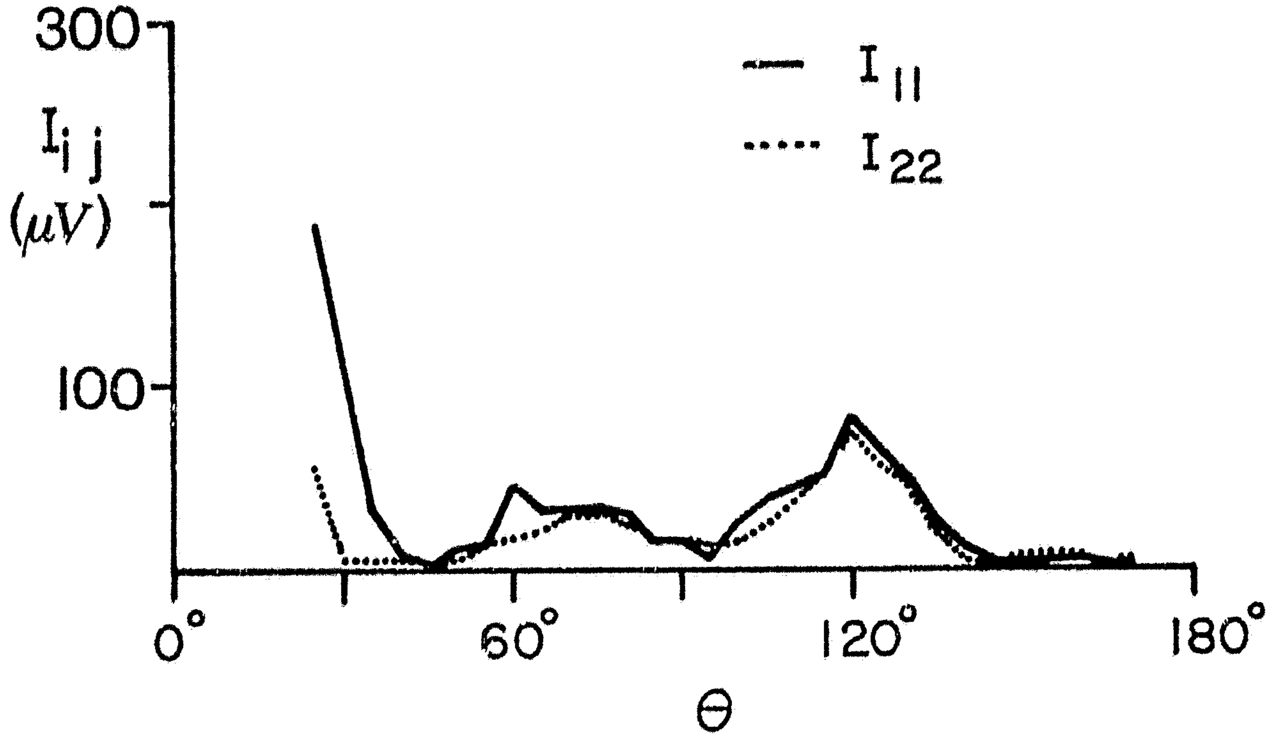

Fig. 4.16a Scattered intensities in units of the potential created over the detector versus scattering angle, from the 4:1 -elongation x = 1.88 cylinder C41. The axis of symmetry is contained in the scattering plane and makes an angle φ = 60° with the direction of the incident radiation $\vec{E}_0$. During this experiment the background was not compensated for. The uncompensated background radiation is displayed in the same units in appendi[illegible].

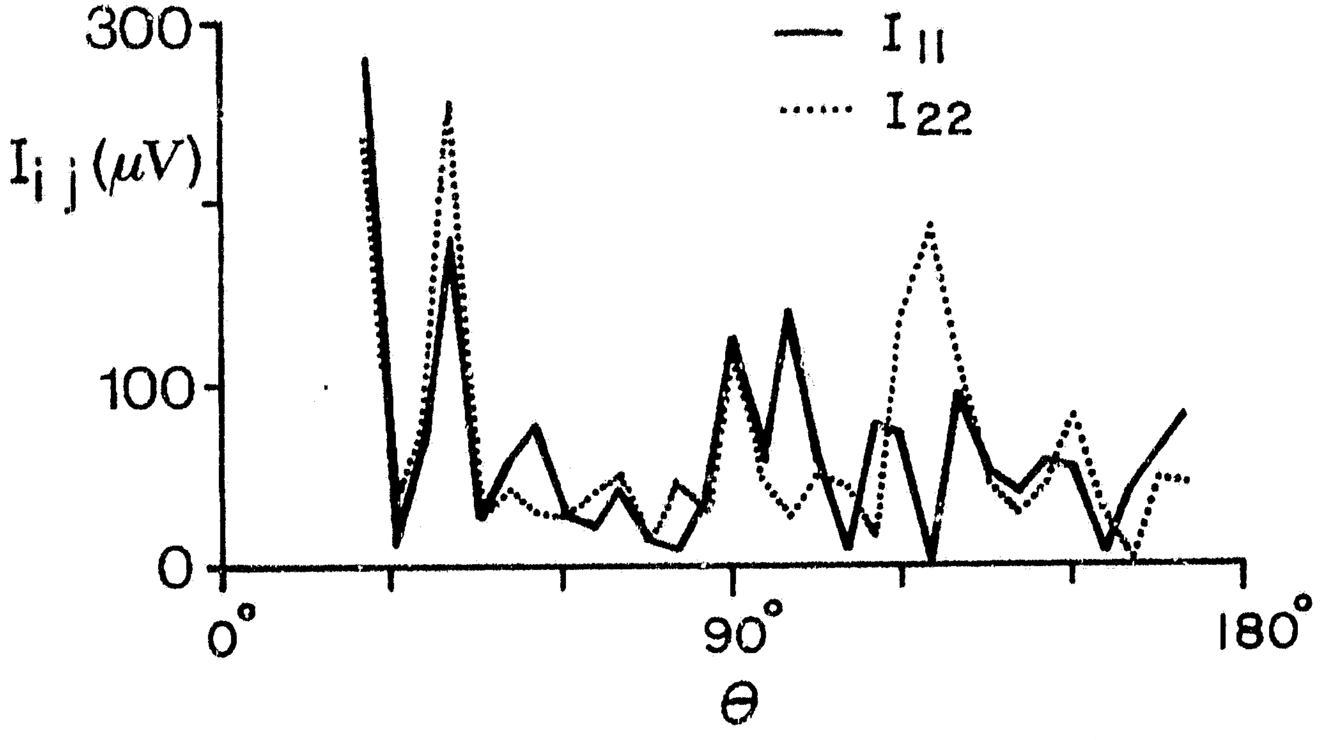

Fig. 4.16b Scattered intensities in units of the potential created over the detector versus scattering angle, from the 43 aligned x = 1.88, 4:1 -elongation cylinders confined into the ensemble U41A. φ = 60° for each individual cylinder. During the experiment the background was not compensated for. The uncompensated background radiation is displayed in the same units in appendix E.

4.1.6 U41R and C41R

U41R: 43, x = 1.88, 4:1 -elongation homogeneous cylinders randomly aligned within an X = 20.08 sphere.

C41R: 1, x = 1.88, 4:1 -elongation homogeneous cylinder, the averages are taken over random orientations.

The differences between U41R and U41A are:

I) The 43 cylinders are not only randomly located as in U41A but also randomly orientated rather than aligned perpendicular to the scattering plane.

II) The size of the spherical ensemble is decreased from X = 25.09 to 20.08.

The difference between C41R and C41A is:

I) The measurements C41R are performed over uniformly distributed orientations to simulated randomness. The actual target C41 is identical in the two experiments.

The angular dependence of the two polarization components I_{11} and I_{22} in experiment C41R are quite similar and approximately straight lines up to $\theta = 90^\circ$ on the logarithmic plot in Fig. 4.17. Although very shallow, the dip at $\theta \approx 105^\circ$ in I_{11} can still be seen. Otherwise the scattering curve is relatively flat with very little backscattering up to the last measurement at $\theta = 165^\circ$. This scattering curve is discussed in more detail by Schuerman at al. (1980) and compared to those for a selection of 28 targets of various size and shape. As the cylinders in target U41R are randomly aligned, the resulting averaged index of refraction over a portion of the agglomerate is independent of the polarization of the incident and scattered light. Thus, the single-scattering approximation predicts the same changes in all polarization components (shown in Fig. 4.18). Higher--order scattering and/or dependent scattering would add a polarization-dependent phase shift with respect to the single scattering. The difference in the degree of polarization of light scattered from the single cylinder and from the agglomerate respectively Fig. 4.19 thus illustrates the importance of these effects.

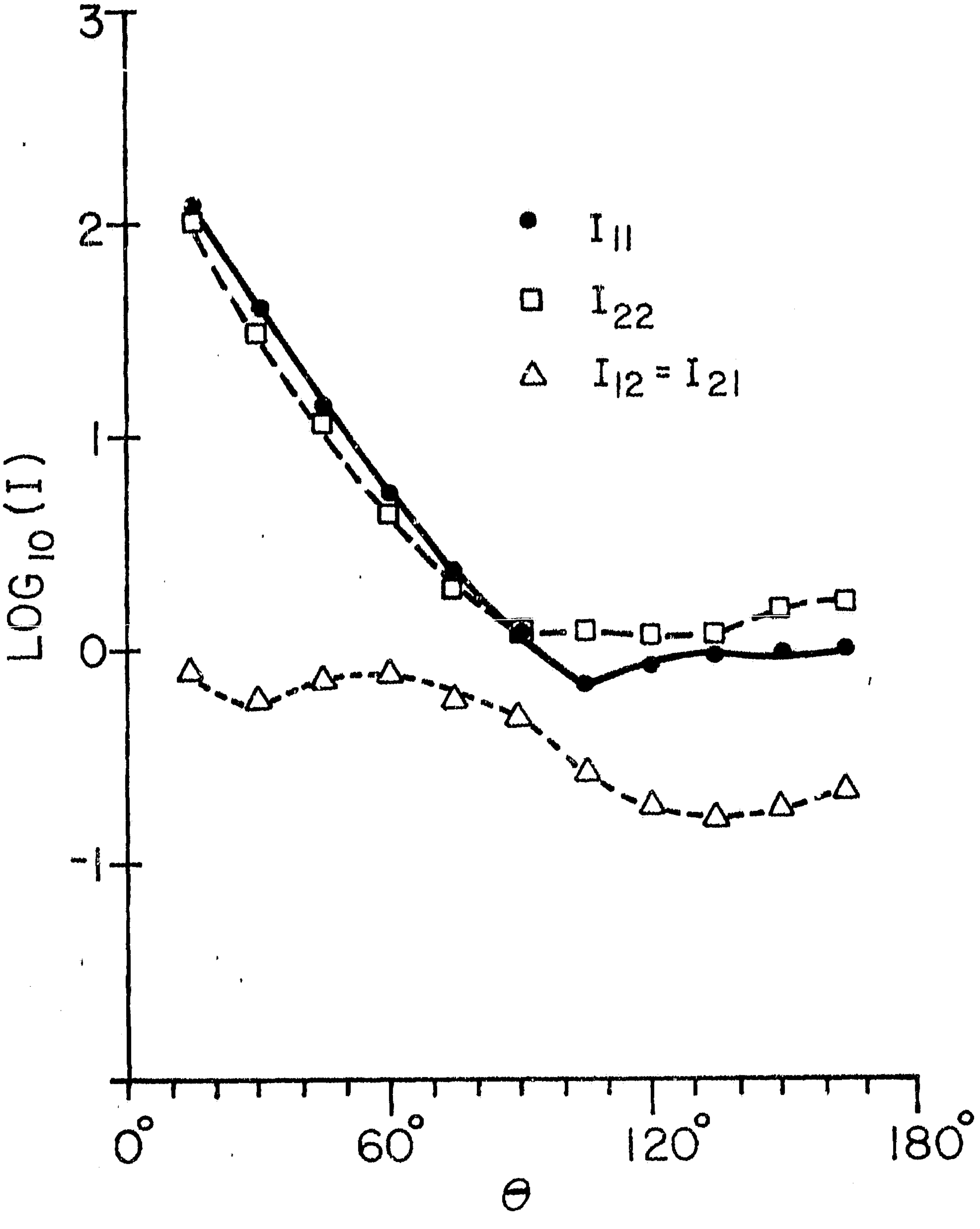

Fig. 4.17 Measured scattered intensities averaged over uniform orientations versus scattering angle for the x = 1.88, 4:1 -elongation homogeneous cylinder C41R.

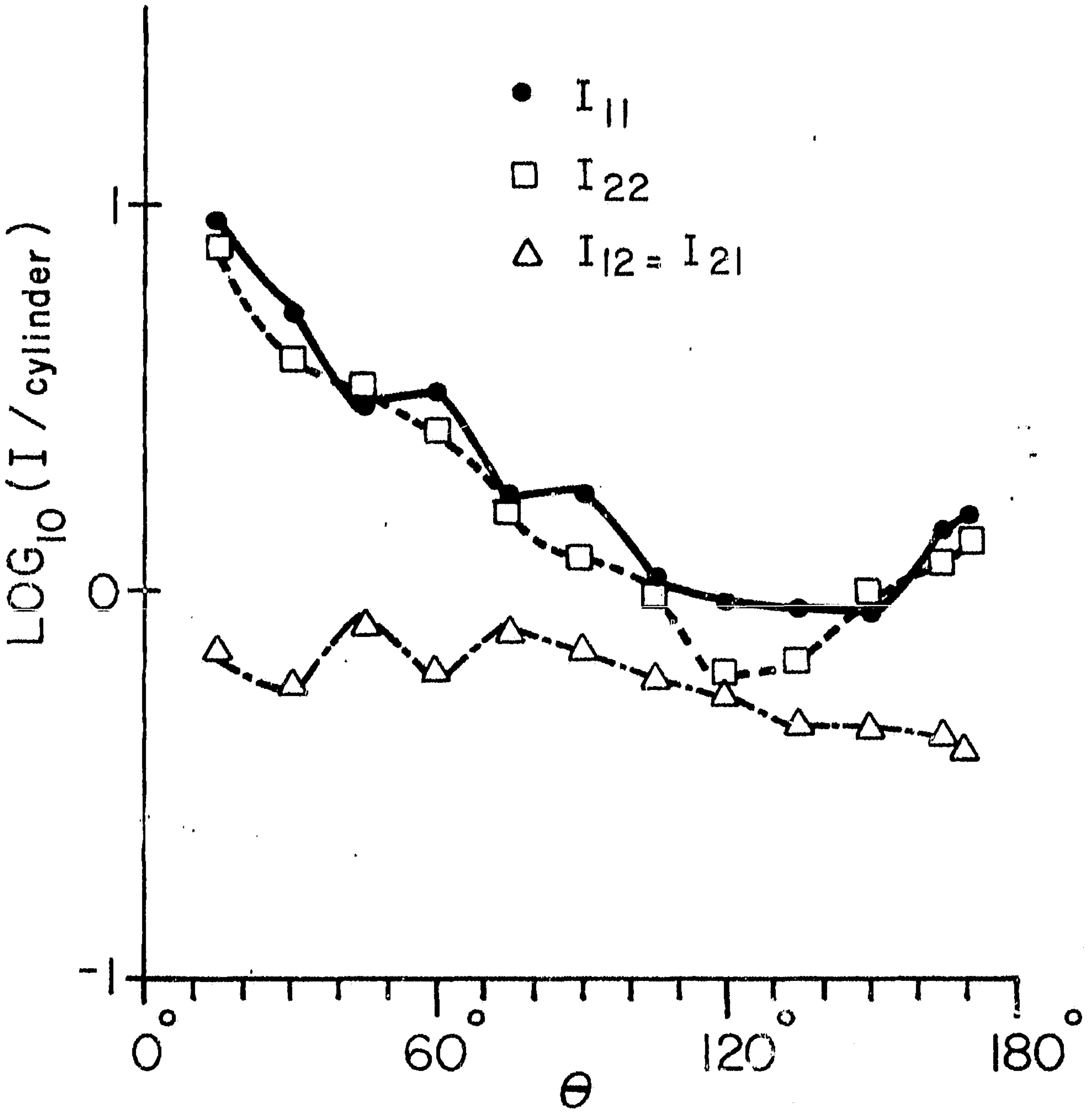

Fig. 4.18 Measured scattered intensities per cylinder versus scattering angle for 43, x = 1.88, 4:1 -elongation cylinders randomly located and orientated in the X = 20.08 spherical ensemble U41R averaged over uniform orientations, of the agglomerate.

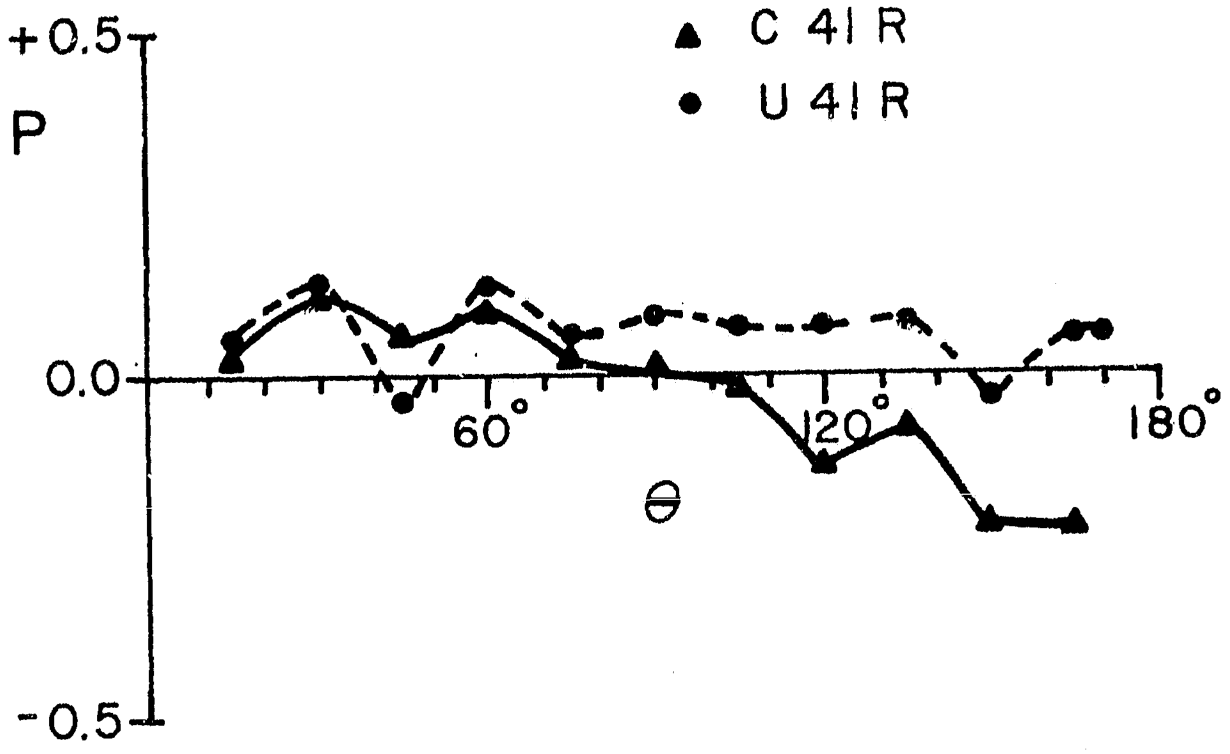

Fig. 4.19 Measured degree of polarization averaged over uniform orientations versus scattering angle for the x = 1.88, 4:1 -elongation single cylinder C41R and for the "spherical" X = 20.08 ensemble U41R of 43 such cylinders.

4.1.7 Dependence on cylinder elongation

T41R: 125, $x = 0.47$, 4:1 -elongation homogeneous cylinders randomly aligned within an $X = 10.04$ sphere.

B41R: 125, $x = 1.74$, 4:1 -elongation homogeneous cylinders randomly aligned within an $X = 37.25$ sphere.

T21R: 240, $x = 0.47$, 2:1 -elongation homogeneous cylinders randomly aligned within an $X = 10.04$ sphere.

B21R: 240, $x = 1.74$, 2:1 -elongation homogeneous cylinders randomly aligned within an $X = 37.25$ sphere.

T11R: 539, $x = 0.47$, 1:1 -elongation homogeneous cylinders randomly aligned within an $X = 10.04$ sphere.

B11R: 539, $x = 1.74$, 1:1 -elongation homogeneous cylinders randomly aligned within an $X = 37.25$ sphere.

T41R, T21R and T11R represent three agglomerates differing in the length-to-diameter ratio of the individual cylinders, the average polarizability is kept constant by varying the number of cylinders. B41R, B21R and B11R are the same targets, respectively, but the measurements were performed at the millimeter-wave laboratory at Bochum. T41R and B41R are compared in the next section (4.1.8) for colour effects. It seems from Figures 4.20, 4.21, 4.22 and 4.23 showing the scattering functions as a function of θ for T41R, T21R, T11R and B41R, B21R and B11R, respectively, that the cylinder elongation has a negligible effect on the scattered intensities averaged over all target orientations. However, the dependence on orientation described by the standard deviation σ of the 272 measurements should be a measure of the target isotropy. In Fig. 4.24 the normalized standard deviation σ/I is plotted as a function of θ. It is seen that σ/I generally decreases with the length of the silicate rods, which are thus more evenly distributed. Scattering in the forward direction is dominated by the Fraunhofer diffraction, which is almost independent of the orientation of the spherical agglomerate. We note also that the phase of the scattered radiation from individual cylinders and therefore the resulting interference pattern depends most heavily on m_{eq} and the size of the agglomerate at sufficiently small scattering angles. In the case discussed here, $X(m_{eq} - 1) \ll \lambda$, and therefore the interference is generally constructive; i.e., the dependence on target orientation is small. At larger scattering angles, on the other hand, the phase depends more heavily on locations of the particles within the ensemble. It is therefore widely differing from particle to particle. The interference pattern as the target T21P is successively rotated around a few axes perpendicular to the scattering plane is shown at 135° scattering angle in Figures 4.2b and 4.2c, on p. 42.

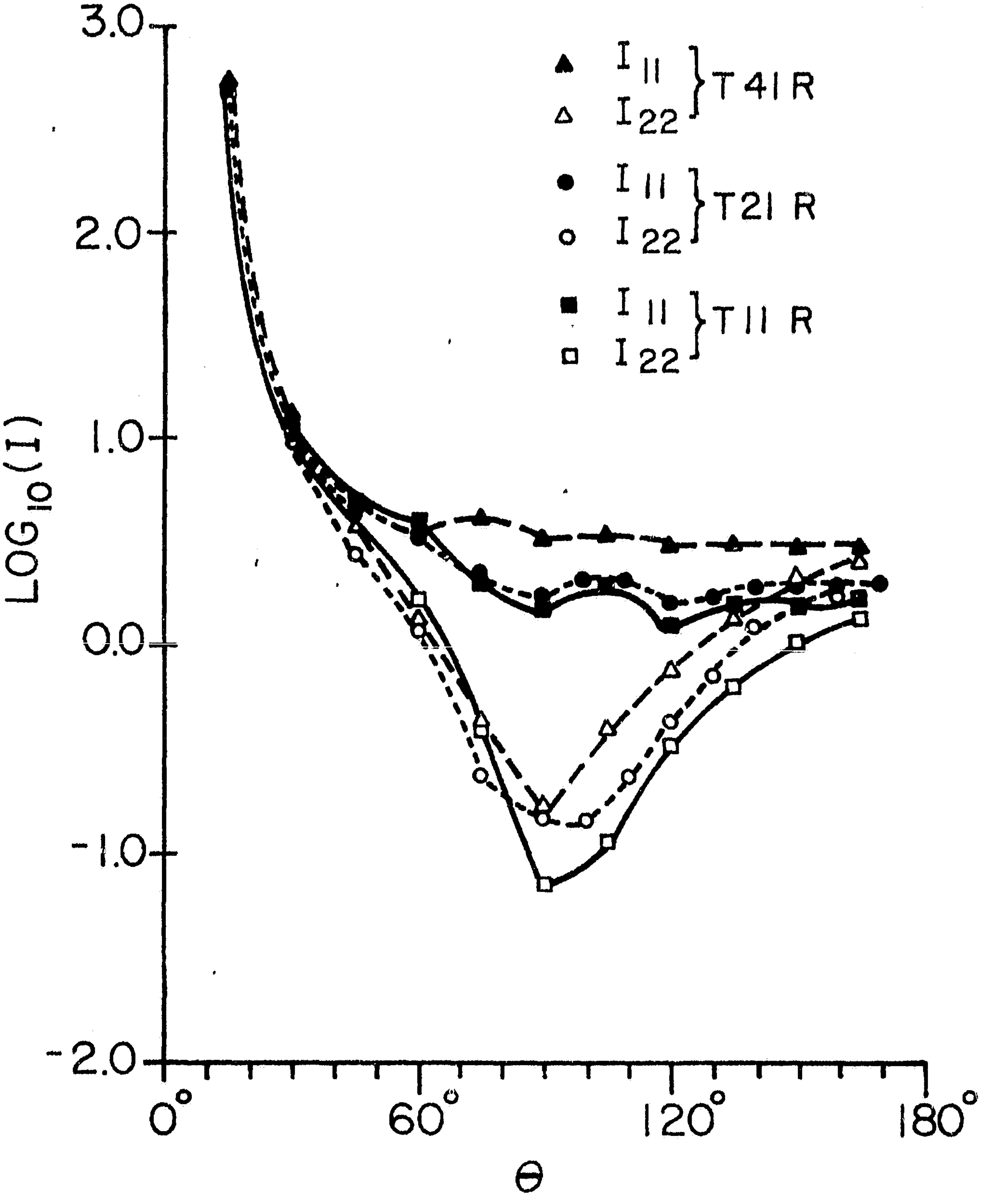

Fig. 4.20 Measured scattered intensities averaged over uniform orientations versus scattering angle for three X = 10.04 "spherical" ensembles of randomly orientated x = 0.47 cylinders. There are 125, 4:1 -elongation cylinders in target T41R, 240, 2:1 -elongation cylinders in T21R and 539, 1:1 -elongation cylinders in T11R. I_{12} were too small ($\lesssim 0.1$) to give reliable data.

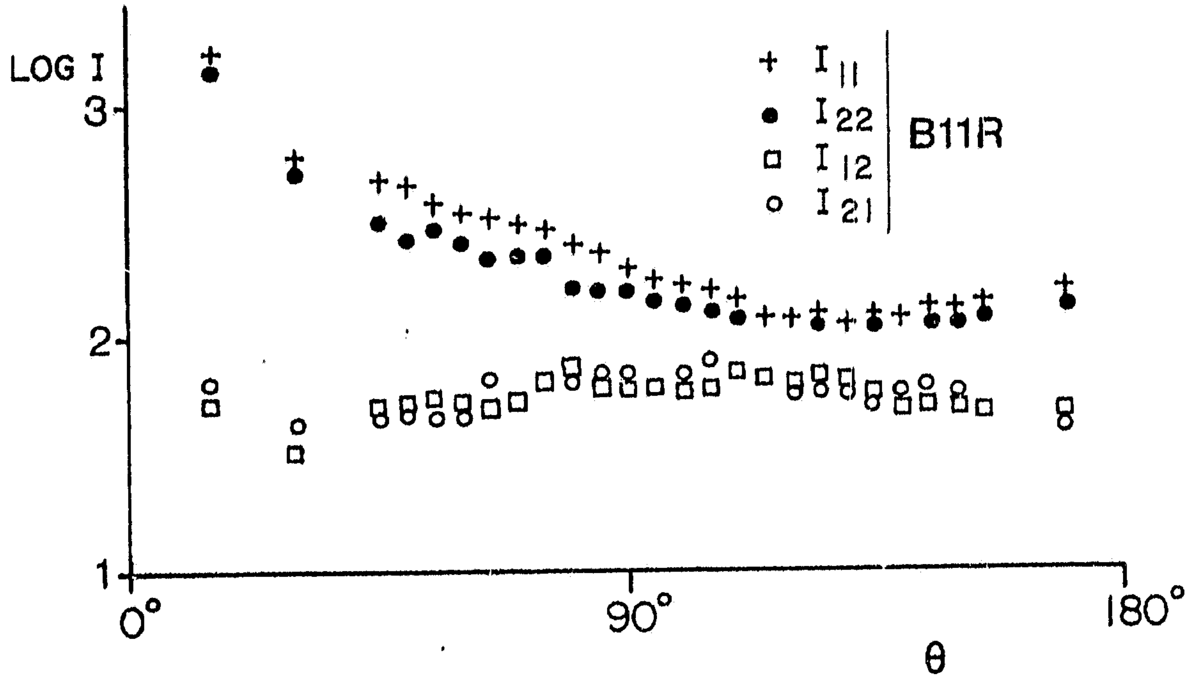

Fig. 4.21a Measured scattered intensities averaged over rotation in azimuth about five different axes of the target in experiment B11R. The X = 37.25 ensemble of 539, x = 1.74, 1:1 -elongation randomly located and orientated cylinders is the same target as T11R but irradiated by the λ = 8.6 mm (35 GHz) waves of the μ-wave laboratory at Bochum rather than the 3.18 cm (9.4 GHz) at Albany. When dots and crosses coincide only crosses are shown, similarly only squares are shown when they coincide with circles.

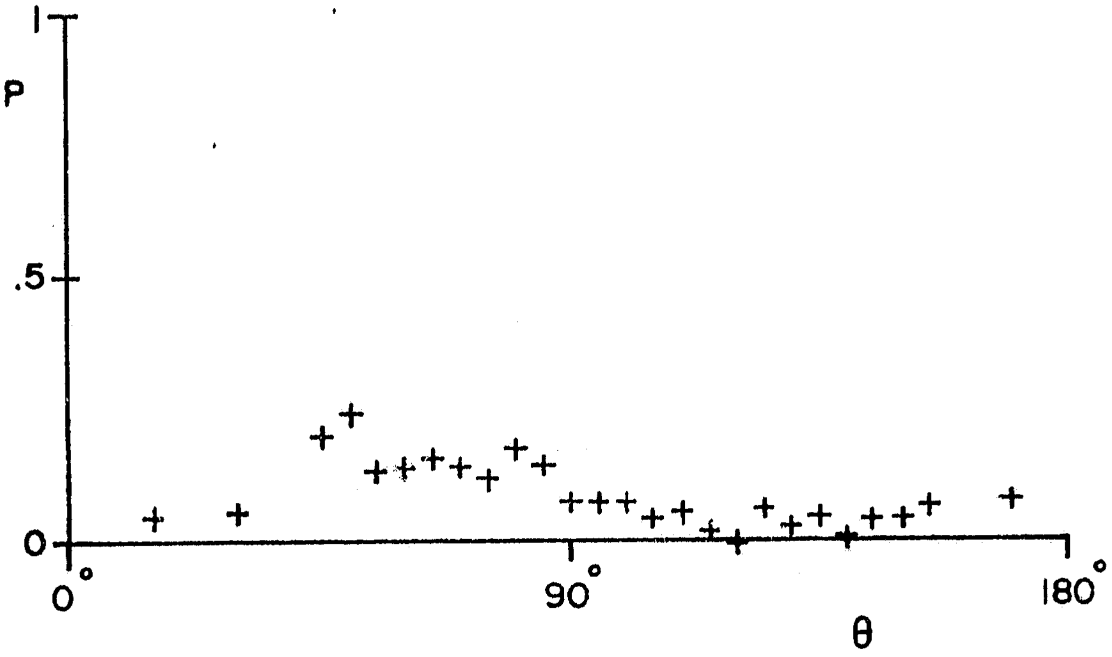

Fig. 4.21b Measured run of the degree of polarization in experiment B11R.

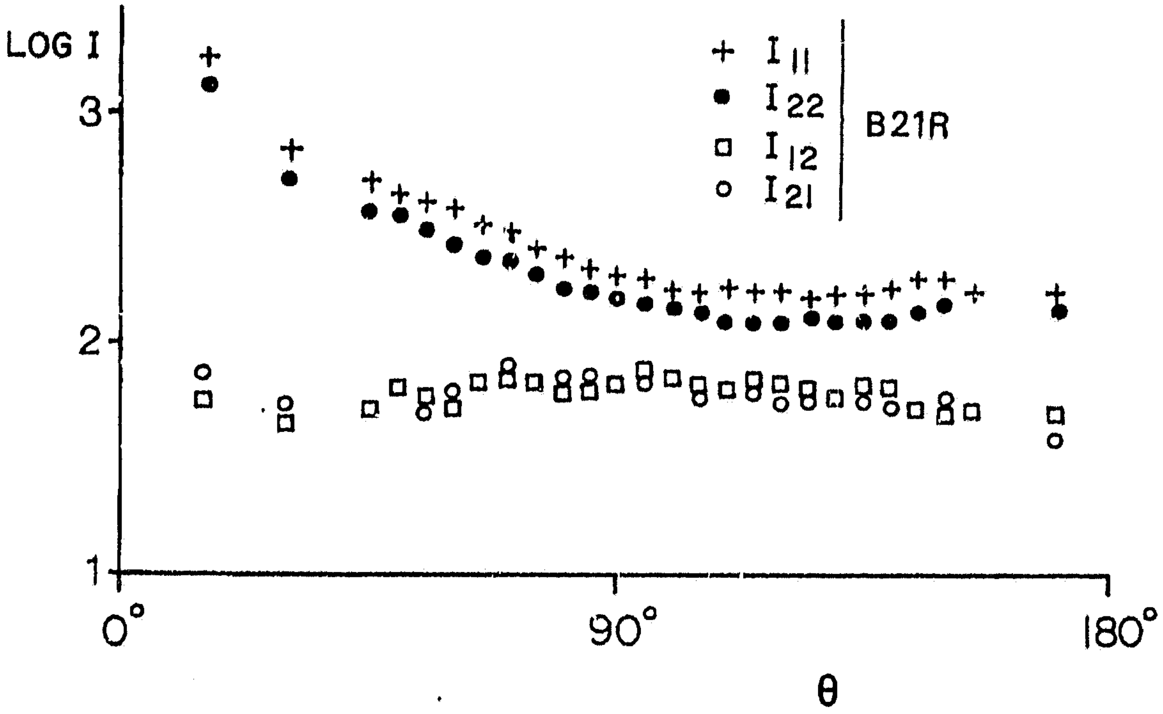

Fig. 4.22a Measured scattered intensities averaged over rotation in azimuth about five different axes of the target in experiment B21R. The X = 37.25 ensemble of 240, x = 1.74, 2:1 -elongation randomly located and orientated cylinders is the same as target T21R but irradiated by the λ = 8.6 mm (35 GHz) waves of the μ-wave laboratory at Bochum rather than the 3.18 cm (9.4 GHz) waves at Albany. When dots and crosses coincide only crosses are shown, similarly only squares are shown when they coincide with circles.

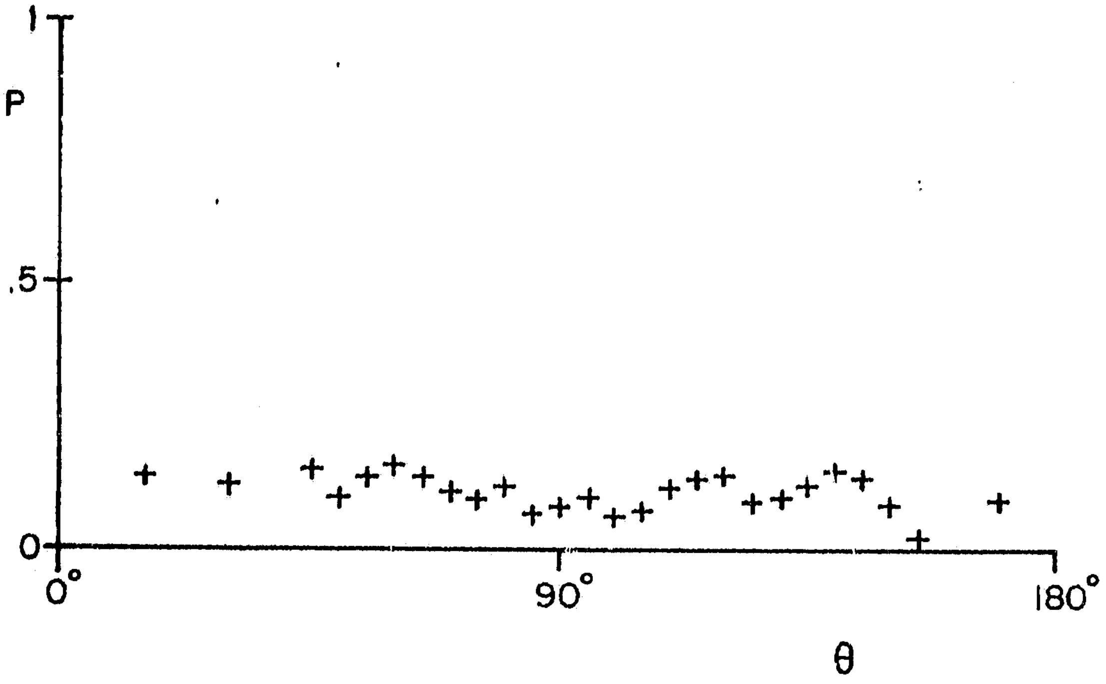

Fig. 4.22b Measured run of the degree of polarization in experiment B21R.

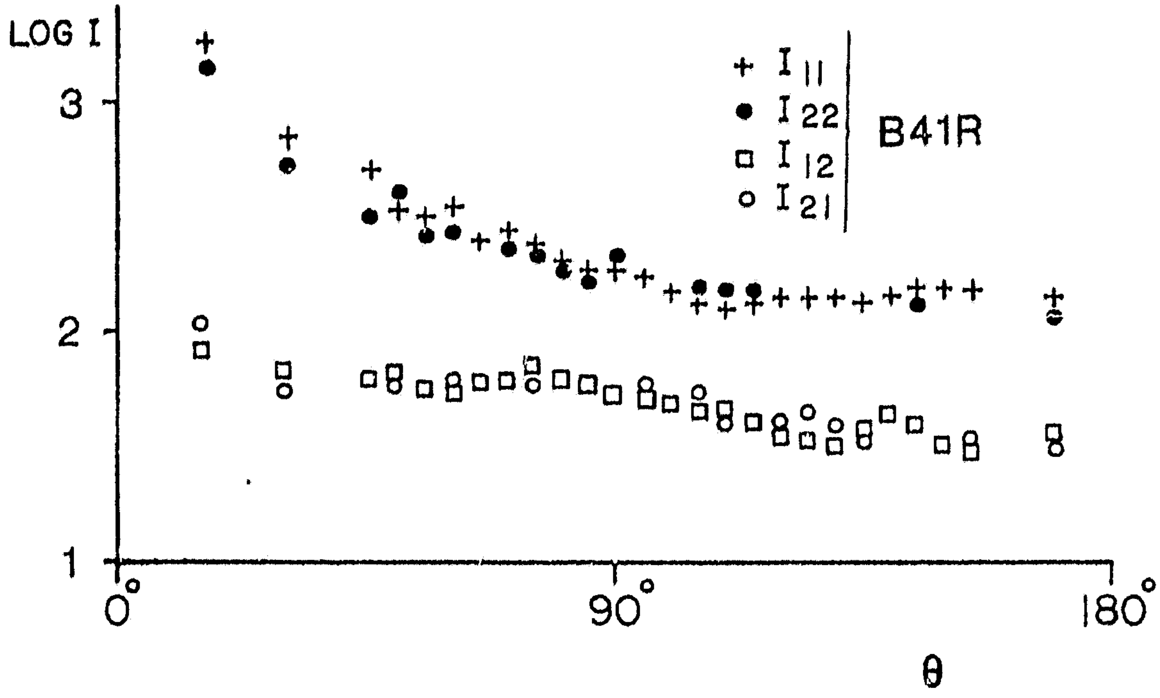

Fig. 4.23a Measured scattered intensities averaged over rotation in azimuth about five different axes of the target in experiment B41R. The X = 37.25 ensemble of 125, x = 1.74, 4:1 -elongation randomly located and orientated cylinders is the same target as T41R but irradiated by the λ = 8.6 mm (35 GHz) waves of the μ-wave laboratory at Bochum rather than the 3.18 cm (9.4 GHz) waves at Albany. When dots and crosses coincide only crosses are shown, similarly only squares are shown when they coincide with circles.

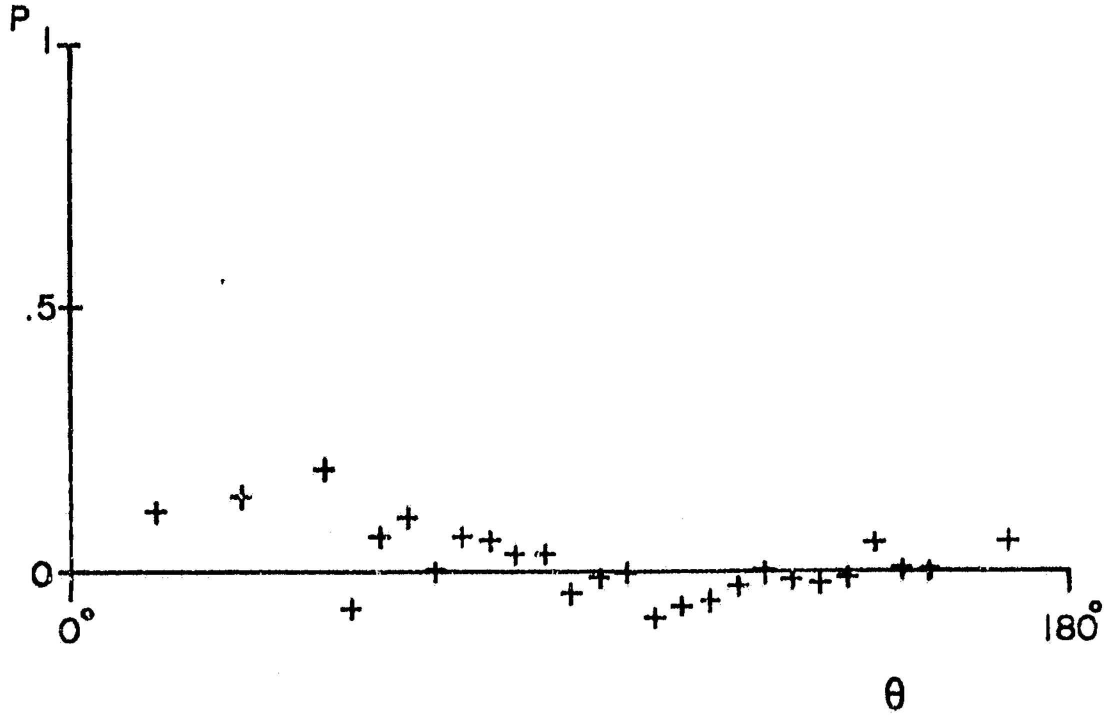

Fig. 4.23b Measured run of the degree of polarization in experiment B41R.

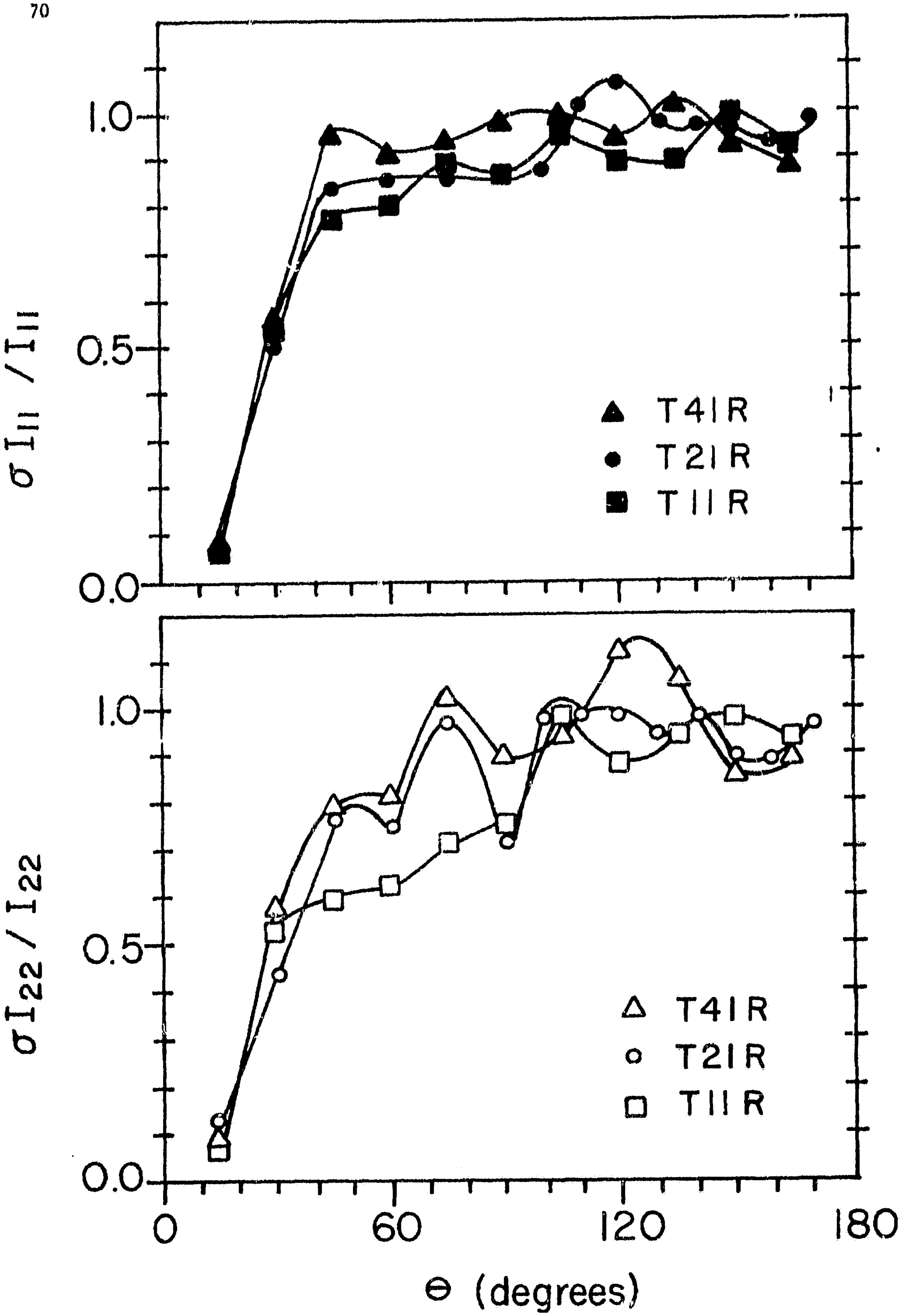

Fig. 4.24 Measured normalized standard deviation of scattered intensities versus scattering angle for targets; T41R, T21R and T11R consisting of 125 4:1, 240 2:1 and 539 1:1 cylinders respectively.

4.1.8 Colour dependence for the agglomerates of silicates

B41R: 125, $x = 1.74$, 4:1 -elongation homogeneous cylinders randomly aligned within an $X = 37.25$ sphere.

U41R: 43, $x = 1.88$, 4:1 -elongation homogeneous cylinders randomly aligned within an $X = 20.08$ sphere.

T41R: 125, $x = 0.47$, 4:1 -elongation homogeneous cylinders randomly aligned within an $X = 10.04$ sphere.

Experiments T41R and B41R were performed using the same target but at different wavelengths. Thus, the differences are, save for a differing averaging technique, truly colour effects. The measurement B41R was performed at the laboratory at Bochum operating at 35 GHz (8.57 mm). If we let T41R represent a particle in yellow light, B41R would represent the same particle near the wavelength of Lyman α. The dip in I_{22} at the longer wavelength of T41R in Fig. 4.20 is only reduced with respect to that of single cylinders by multiple or dependent scattering. At the shorter wavelength of B41R, however, the single cylinders exhibit only a very shallow dip which vanishes in the scattering of the "bird's-nest" Fig. 4.23. The phase function for $x = 1.74$ and $x = 1.88$ cylinders are not expected to differ very much. The total brightness for infinite and randomly orientated cylinders is shown in Fig. 4.25 and for the agglomerates in Fig. 4.26. Thus a comparison between the B41R and U41R measurements Figures 4.23 and 4.18 merely reflect the difference in agglomerate size and a small change in the average index of refraction as 43 rather than 30.5 cylinders were fitted in the $X = 20.08$ hollow eccofoam sphere to make up "bird's-nest" U41R. There are few differences in the runs of $I_{11}(\theta)$ and $I_{22}(\theta)$ as given by the two sets of measurements, but the relative importance of cross-polarization in B41R is surprisingly low. No measurements for the $x = 1.74$ single cylinder was performed to provide an adequate comparison, note also that the cross-polarized components were not rigorously calibrated as these components vanish for the spheres used as standard (see also section 2.5.6).

We conclude that in this case the size of the agglomerate does not seem to have a decisive effect on the shape of the scattering function, and that the magnitude is approximately proportional to the number of scattering particles. Whereas the colour dependence of the individual scatterers is still quite important for agglomerates of this size the effect is expected to be reduced by dependent scattering which increases in importance as the size of the agglomerate grows.

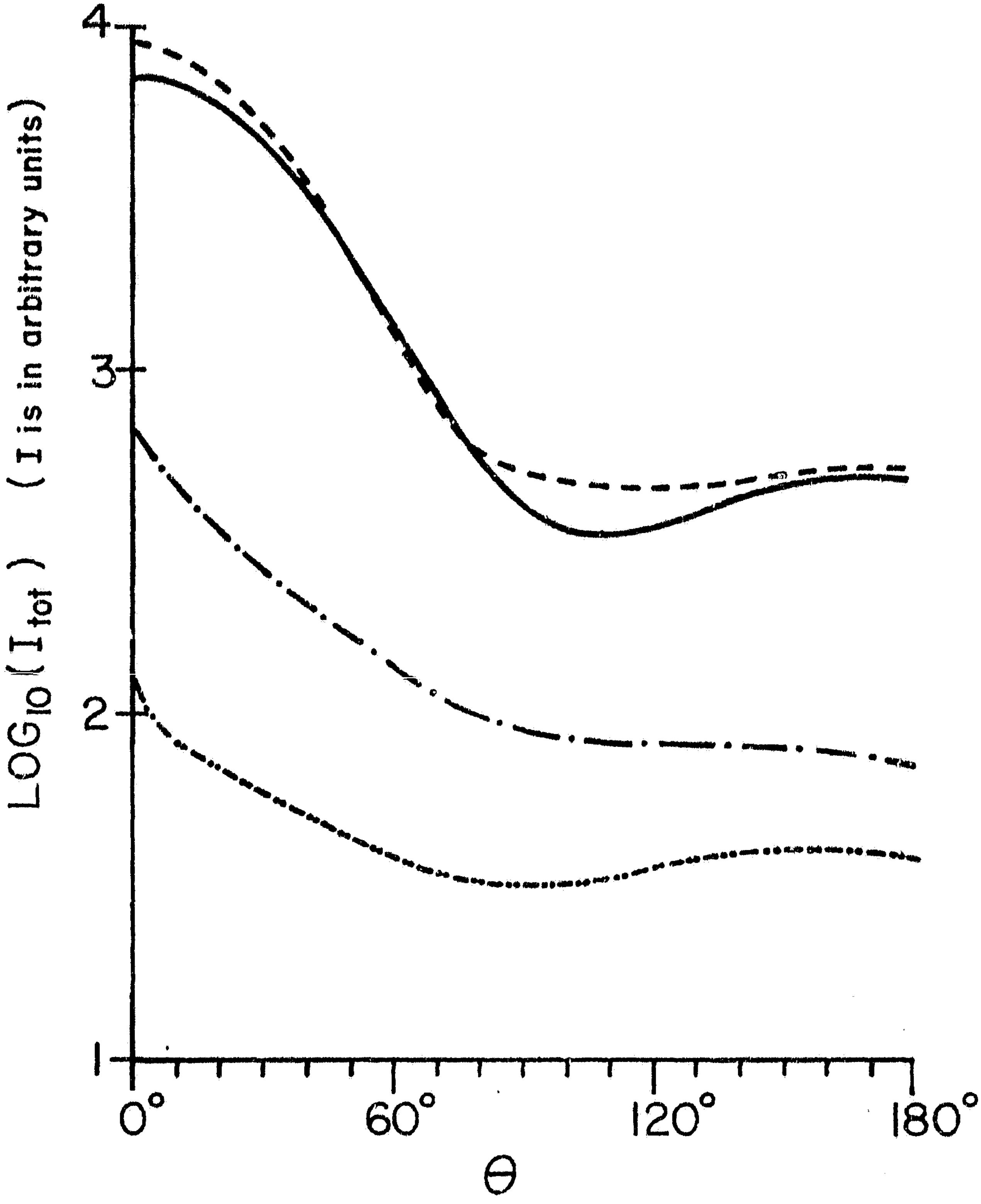

Fig. 4.25 Theoretical relative brightness versus scattering angle for independently scattering infinite cylinders averaged over random orientation for m = 1.618 - 0.005i and size parameter x = 0.47; dash-dot-dot, x = 0.78; dash-dot, x = 1.74; solid, and x = 1.88; dashed curve.

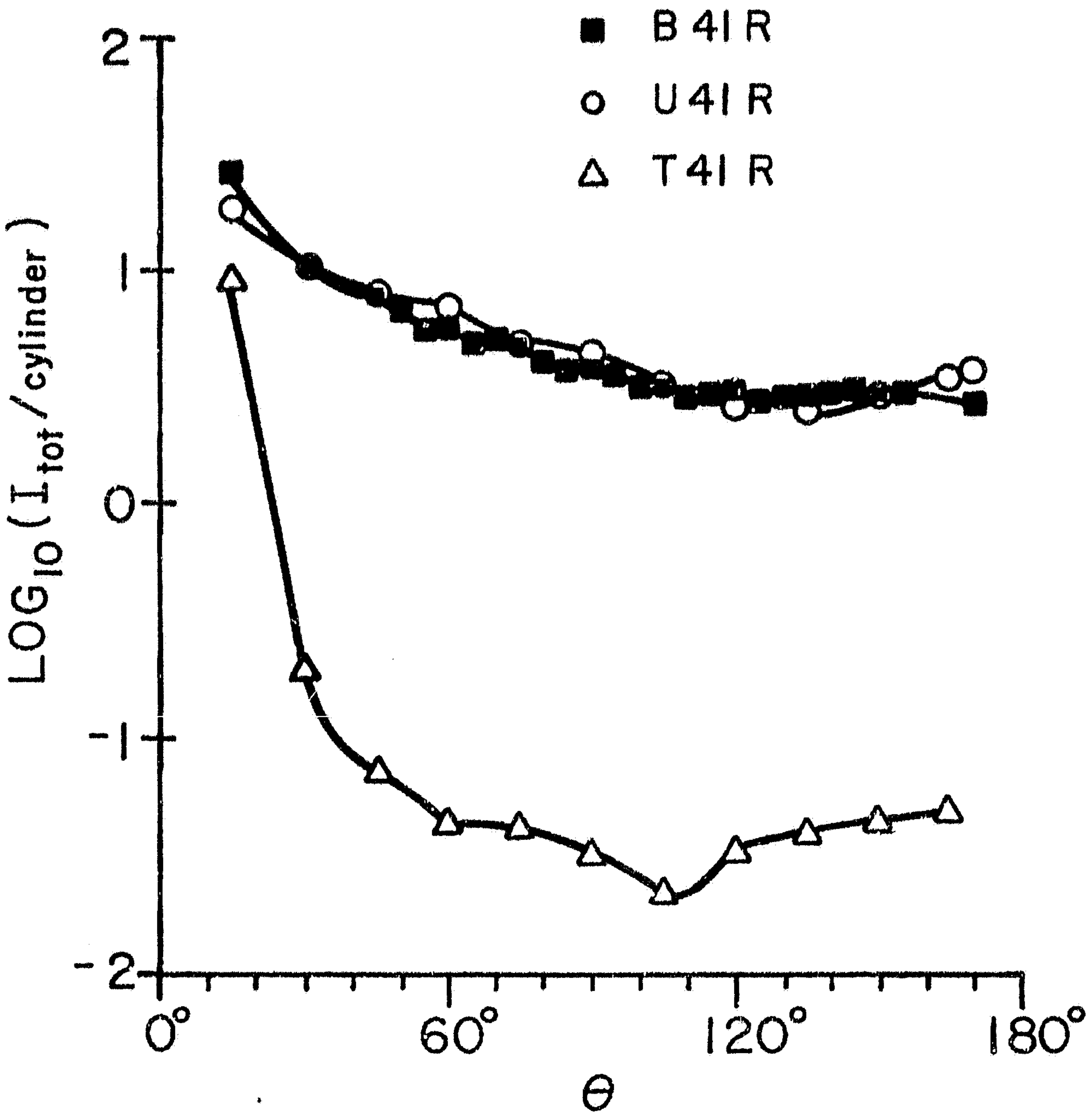

Fig. 4.26 Measured angular distribution of brightness per cylinder for the ensembles T41R consisting of 125, 4:1 -elongation x = 0.47 cylinders in an X = 10.04 "sphere", U41R; 43 4:1 -elongation x = 1.88 cylinders in an X = 20.08 "sphere" and B41R consisting of 125 4:1 -elongation x = 1.74 cylinders in an X = 37.25 "sphere" respectively.

4.1.9 Dependence on particle number density.

T21R: 240, $x = 0.47$, 2:1 -elongation homogeneous cylinders randomly aligned within an $X = 10.04$ sphere.

TC21R: 204, $x = 0.47$, 2:1 -elongation homogeneous cylinders randomly aligned within an $X = 15.81$ sphere.

V21R: 44, $x = 0.78$, 2:1 -elongation homogeneous cylinders randomly aligned within an $X = 15.81$ sphere.

The Fraunhofer diffraction concentrates towards the forward direction as the size of the ensemble increases. It is thus expected that the side scattering from TC21R is more closely represented by the pure "interference" approximation than the more closely packed T21R. This approximation also predicts a concentration towards small θ's for the expanded ensemble (see section 3.6.3). The dependence on orientation χ, ψ, (α,β) and therefore σ/I is expected to be smaller for TC21R at $\theta \cong 0$ but to increase more rapidly with θ (fig. 4.28) whereas the resulting scattered intensity (fig. 4.27) decreases more rapidly. This can be seen from eq. 3.21 in the limit $m_{eq} \to 1$. Target V21R occupies the same volume as TC21R, but the scattering material has been concentrated in larger cylinders. The side scattering pattern, (fig. 4.27), mostly reflects the difference in scattering functions for the individual cylinders. This can be seen by comparing the total brightness measured for TC21R and V21R (fig. 5.5) to the computed brightness for the respective cylinders (portions of infinite cylinders) independently scattering the incident light (see fig. 4.25). The "fluctuations" in the phase of the scattered signal from each cylinder as a function of orientations is expected to vary more heavily for V21R than for the more "homogeneous" TC21R. That effect is seen in Fig. 4.28 as a flatter θ dependence for V21R than for TC21R.

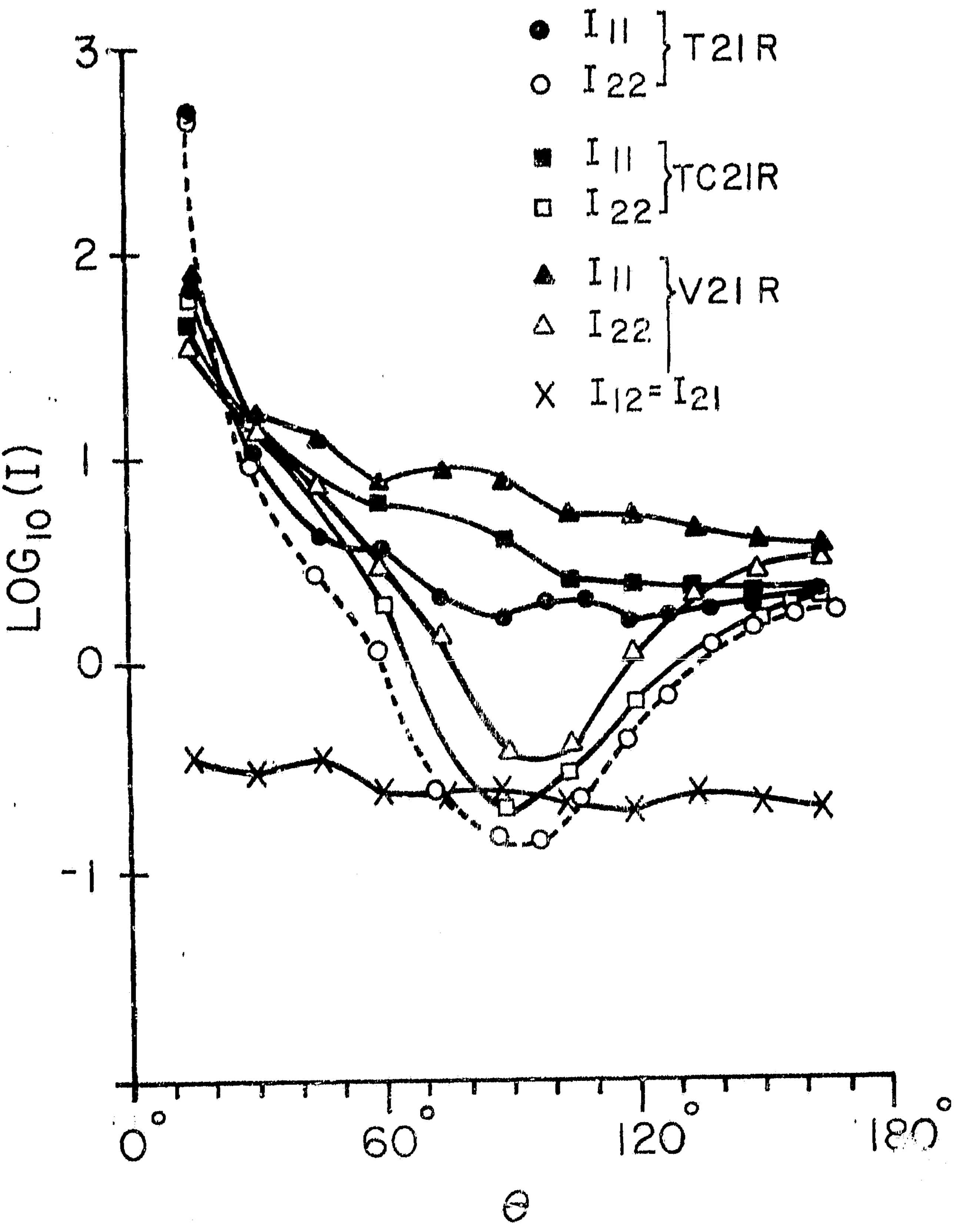

Fig. 4.27 Measured polarized intensity components as a function of scattering angle for the ensembles T21R, TC21R and V21R consisting of 240 x = 0.47 2:1, 204 x = 0.47 2:1 and 44 x = 0.78 2:1 elongation cylinders in X = 10.04, 15.81 and 15.81 "spherical" ensembles respectively.

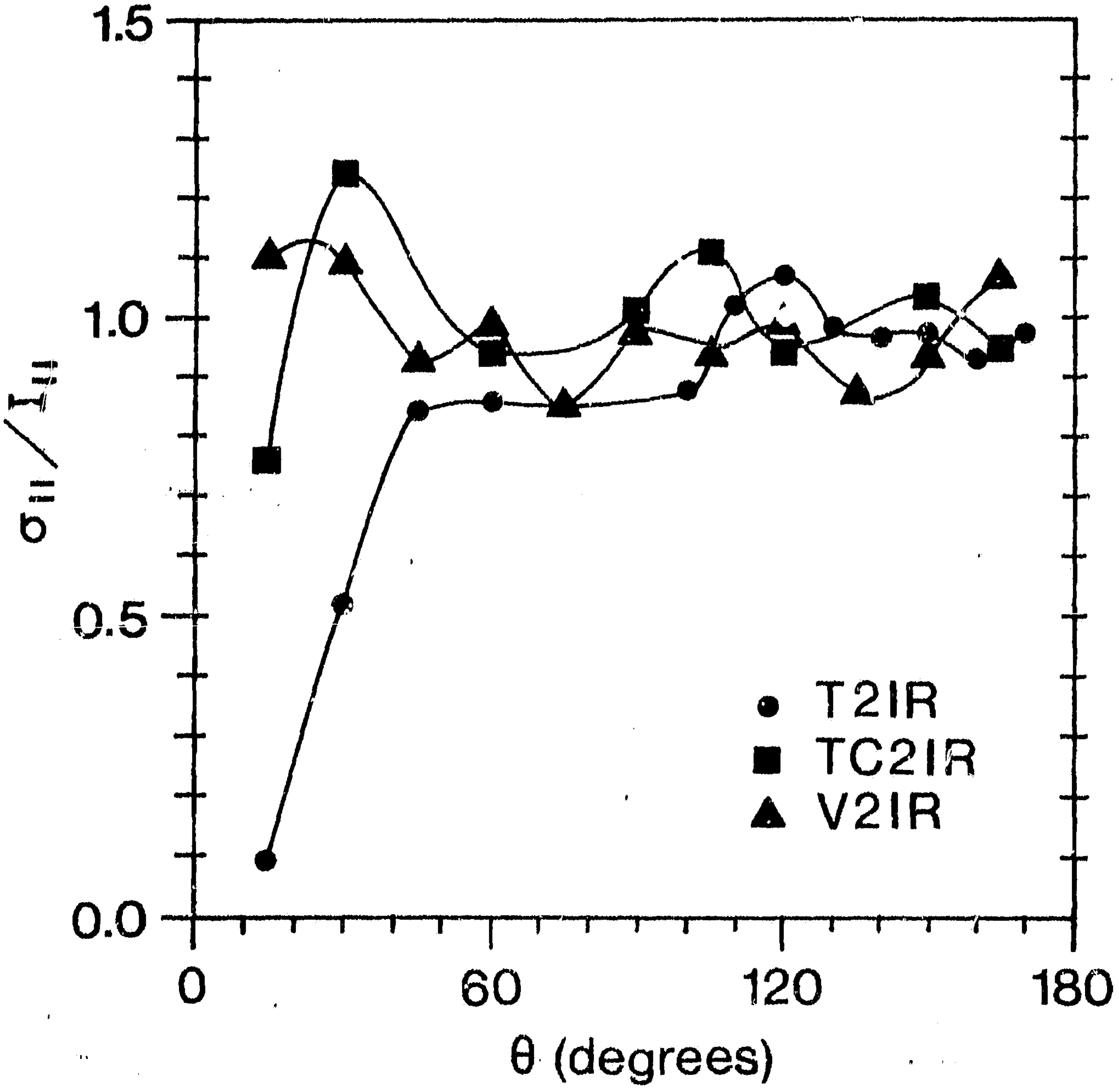

Fig. 4.28 Measured and normalized standard deviation of scattered intensities versus scattering angle for targets; T21R consisting of 240 x = 0.47 2:1 elongation cylinders, TC21R:204 x = 0.47 2:1, V21R: 44 x = 0.78 2:1 elongation cylinders in X = 10.04, 15.81 and 15.81 "spherical" ensembles respectively.

4.2 Silicate Core - "Ice" Mantle Cylinders

The scattering by the ensemble IC3b, is compared to that by IC4b and IC4c for colour effects in sections 5.2.2 and 5.2.3. The ensemble IC1a is also discussed in the same sections. The run of the polarized intensity components are shown separately in Figures 4.37 and 4.38 for IC3b and IC1a respectively.

4.2.1 Dependence on the size of the agglomerate

IC4d: 80, $x_m = 2.45$ ($\sigma_x = .07$), 1.96 ($\sigma_e = .04$) to 1 mean elongation eccofoam 1.7 mantles and $x_c = 0.78 \sim 2$ to 1 elongation lucite core cylinders randomly aligned within an $X = 19.3$ sphere.

IC4c: 44, $x_m = 2.45$ ($\sigma_x = .06$), 1.97 ($\sigma_e = .04$) to 1 mean elongation eccofoam 1.7 mantles and $x_c = 0.78 \sim 2$ to 1 elongation lucite core cylinders randomly aligned within an $X = 15.8$ sphere.

IC4b: 23, $x_m = 2.45$ ($\sigma_x = .06$), 1.96 ($\sigma_e = .05$) to 1 mean elongation eccofoam 1.7 mantles and $x_c = 0.78 \sim 2$ to 1 elongation lucite core cylinders randomly aligned within an $X = 12.6$ sphere.

12R: 1, $x_m = 2.44$, 1.954 to 1 elongation eccofoam 1.7 mantle and a $x_c = 0.78 \sim 2$ elongation lucite core cylinders. The averages are taken over random orientations.

The run of the scattered polarized components I_{11}, I_{22} and I_{12} with scattering angle was measured for the single core-mantle cylinder "12" representing a single interstellar grain. The scattering averaged over "uniformly" distributed orientations (as described in section 2.7.1) to simulate randomly orientated cylinders is shown in Figure 4.29. The single scattering approximation described in chapter 3 is applied to the equal density agglomerates of 23, 44 and 80 grains respectively, all of which are reproductions of "12". The average scattering efficiencies over random orientations were substituted for that of each of the randomly orientated cylinders. The detected signal from "12" at some combinations of polarization, scattering angle and orientation were close to the noise level ($\approx 10^{-2}$) although version C of the laboratory apparatus was used. The thus introduced errors propagate to the single scattering approximation (see Chapter 3). It is possible that the oscilliations seen in the computed run of I_{11} around 110° scattering angle are caused by this effect. The dots in Figures 4.30 to 4.35 are the results of the single scattering computations as well as the open triangles, circles and squares in Figure 4.36 the dashed curves corresponding to the dots are added for illustration purposes only, as are the curves in Figure 4.36. It is seen in the Figures 4.30 to 4.35 that the scattering at small angles approaches the diffraction pattern discussed in section 3.3. The diffraction pattern is approximated by that for a homogeneous sphere with "equivalent" index of refraction as given by Equation 3.1 after averaging the dipole moments per unit volume (P). Towards higher scattering angles the single scattering approximation is approached. The cross-polarization components $I_{12} = I_{21}$ over uniform distribution of orientations are compared in Figure 4.36, the diffraction does not polarize. It is therefore expected that the experimental results follow the single scattering approximation at all scattering angles. Note that the measured scattering by the single cylinder "12", on which the "interference" theory relies, might be subject to large experimental errors.

It was concluded in section 4.1.1 that the scattering by the 125 aligned cylinders in target T41A were closely reproduced by the single scattering approximation at $\theta > 90^o$ and approach the diffraction pattern at lower θ's. We may draw the same general conclusion for targets IC4b, IC4c and IC4d except that the magnitude of the I_{11} component is lower for the larger agglomerates than predicted by the theory. This leads to a lower degree polarization for agglomerates than for individual cylinders and moves the maximum degree of polarization to lower scattering angles for the bigger agglomerates.

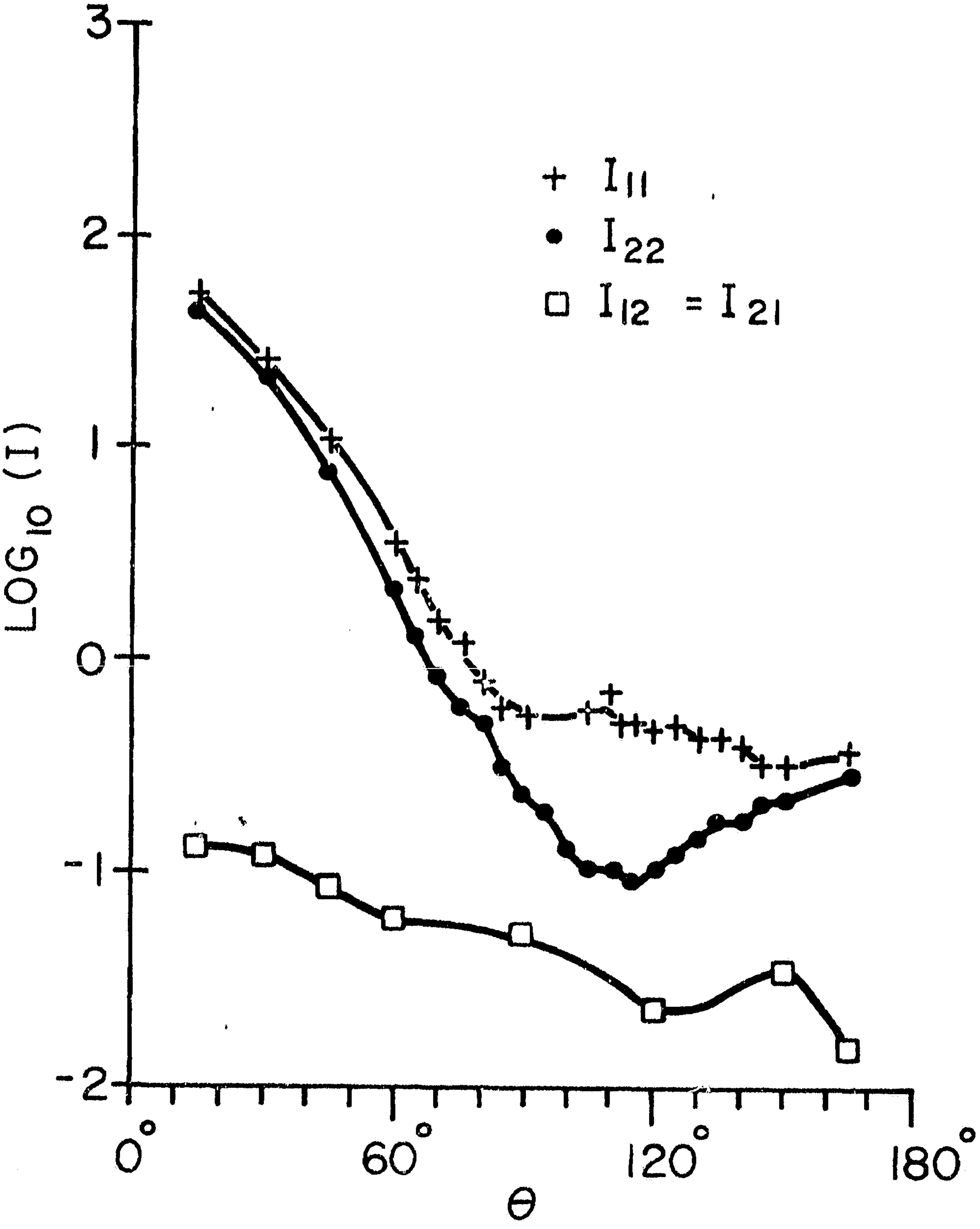

Fig. 4.29 Measured intensities scattered off a single silicate-core-"ice"-mantle cylinder of 2:1 elongation modelling an interstellar dust grain. The intensities are averaged over "uniformly" distributed orientations (see section 2.7.1 for explanations). The connecting curves are added for illustration purposes only.

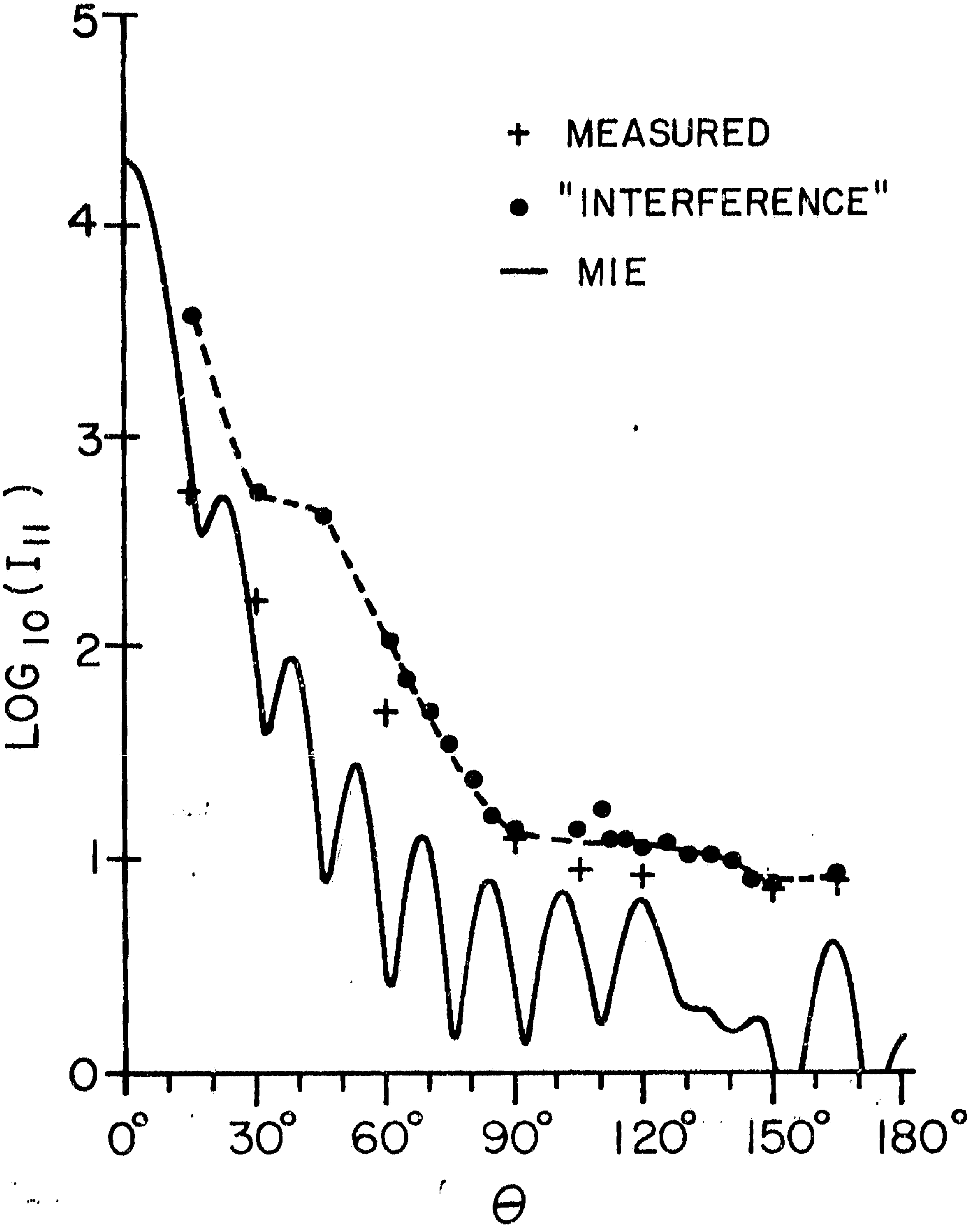

Fig. 4.30 Theoretical and experimental intensities versus scattering angle for ensemble IC4b consisting of 23 randomly located and orientated core-mantle cylinders with $x_c = 0.78$, $x_m = 2.45$ and close to 2:1 elongation within an X = 12.6 "sphere". I_{11} is the intensity for radiation polarized perpendicular to the scattering plane. Solid curve is the Mie theory result for the ensemble treated as a homogeneous sphere with an equivalent index of refraction (see equation 3.1); dashed curve is for the ensemble scattering treated coherently and averaged statistically using the single scattering "interference" theory (see text for explanation) the scattering by individual cylinders was determined experimentally and is shown separatly in Fig. 4.29; crosses are the experimental results for the ensemble.

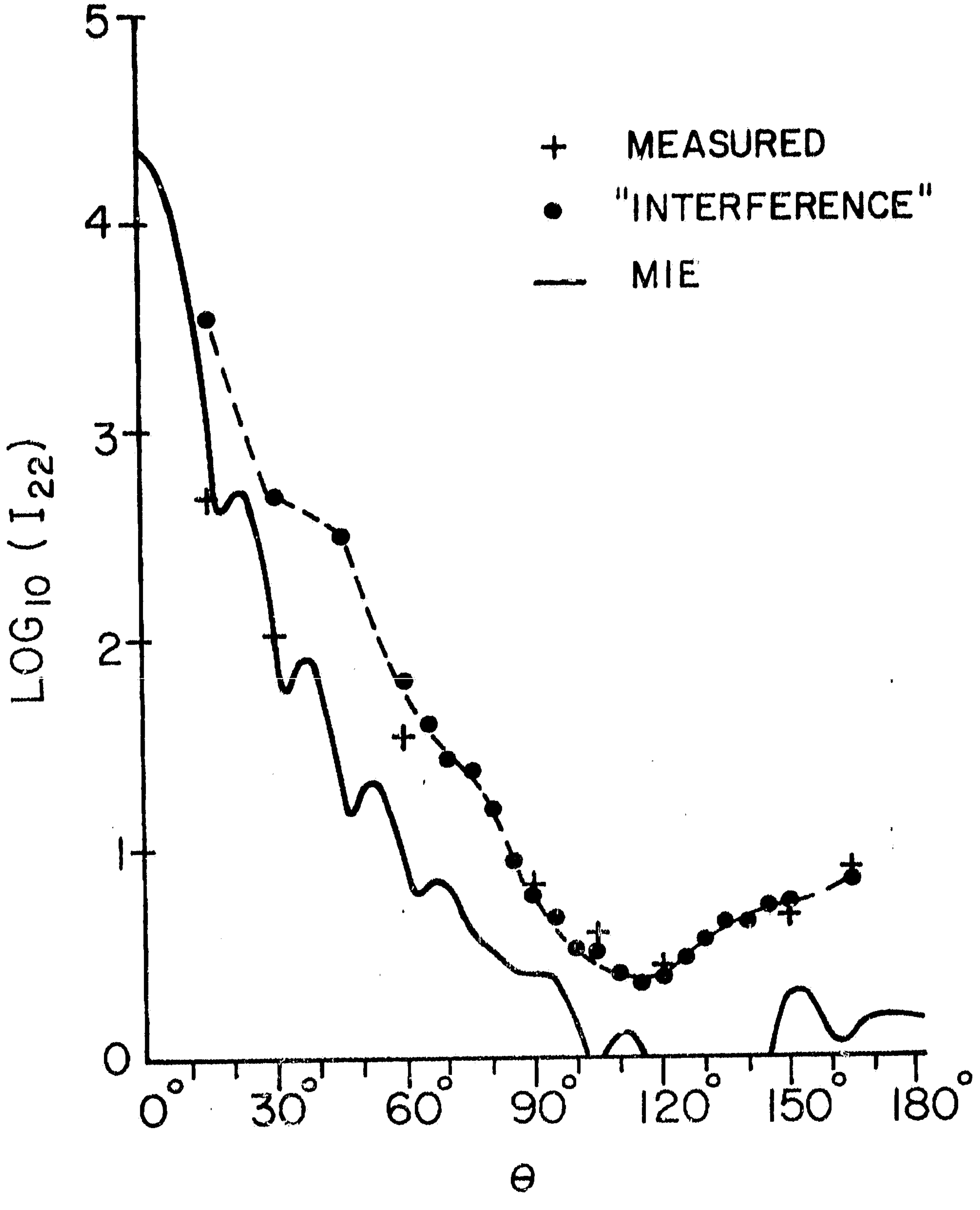

Fig. 4.31 Same as Fig. 4.30 except I_{22} is the intensity for radiation polarized in the scattering plane.

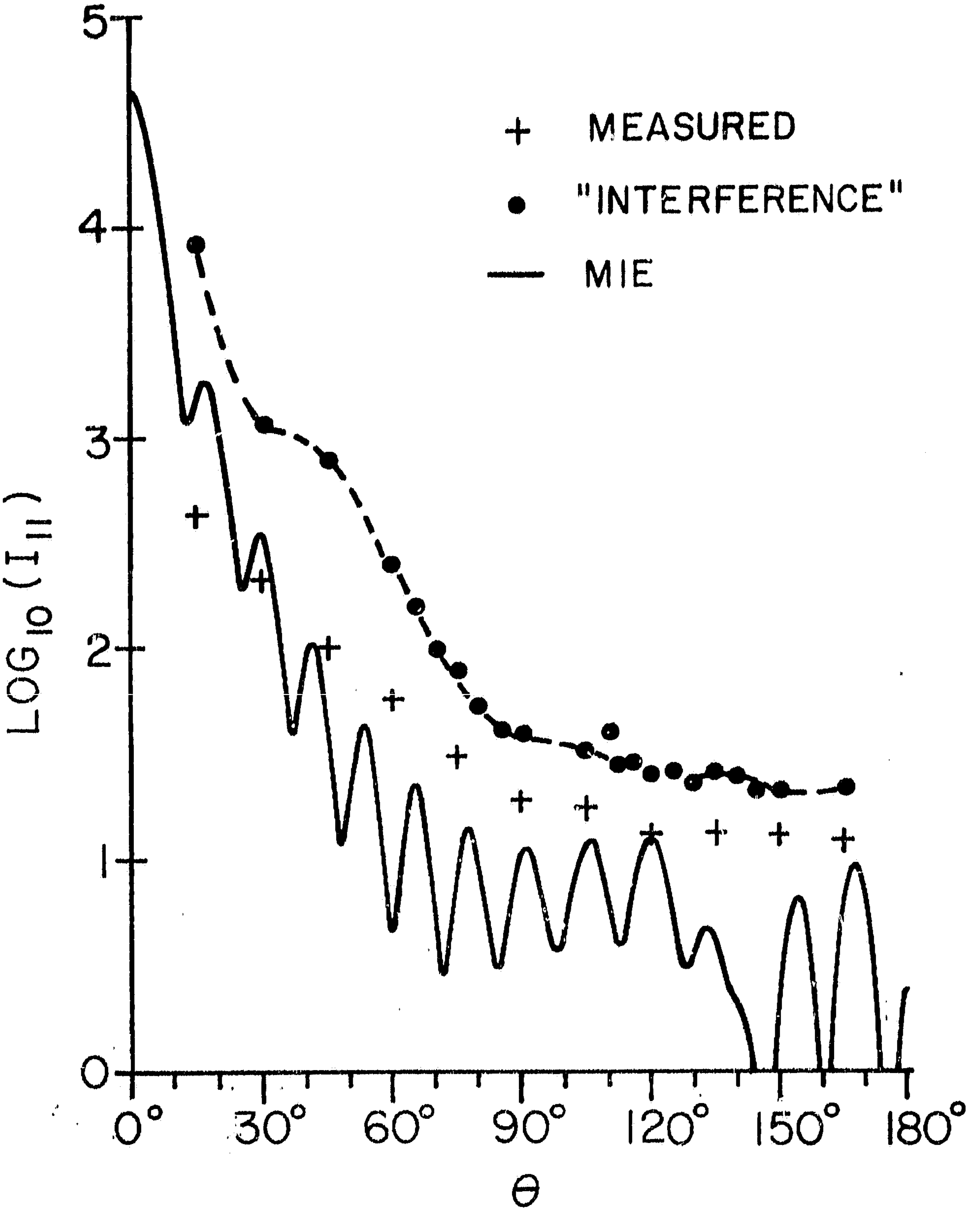

Fig. 4.32 Theoretical and experimental intensities versus scattering angle for ensemble IC4c consisting of 44 randomly located and orientated core-mantle cylinders with $x_c = 0.78$, $x_m = 2.45$ and close to 2:1 elongation within an $X = 15.81$ "sphere". I_{11} is the intensity for radiation polarized perpendicular to the scattering plane. Solid curve is the Mie theory result for the ensemble treated as a homogeneous sphere with an equivalent index of refraction (see equation 3.1); dashed curve is for the ensemble scattering treated coherently and averaged statistically using the single scattering "interference" theory (see text for explanation) the scattering by individual cylinders was determined experimentally and is shown seperately in Fig. 4.29; crosses are the experimental results for the ensemble.

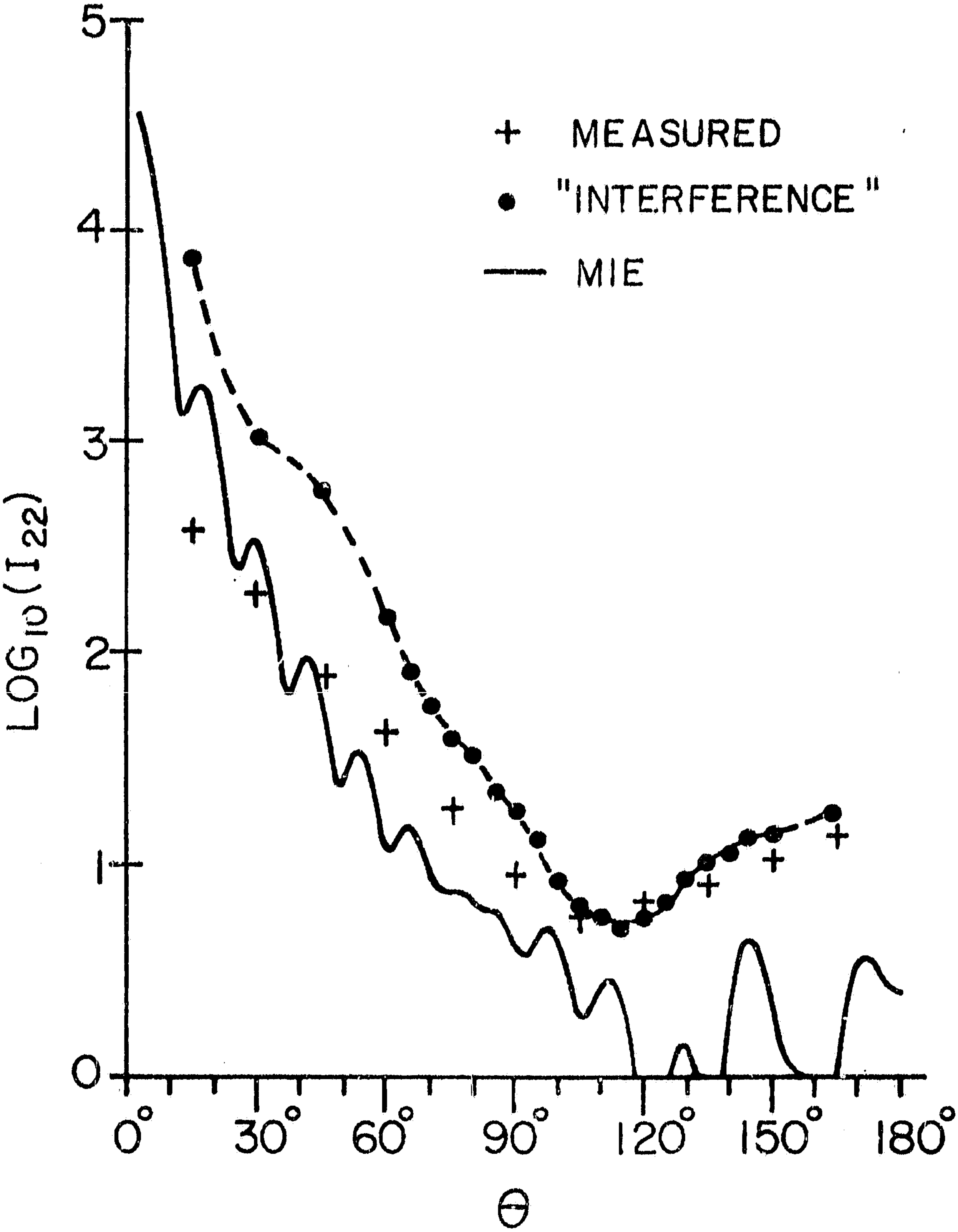

Fig. 4.33 Same as Fig. 4.32 except I_{22} is the intensity for radiation polarized in the scattering plane.

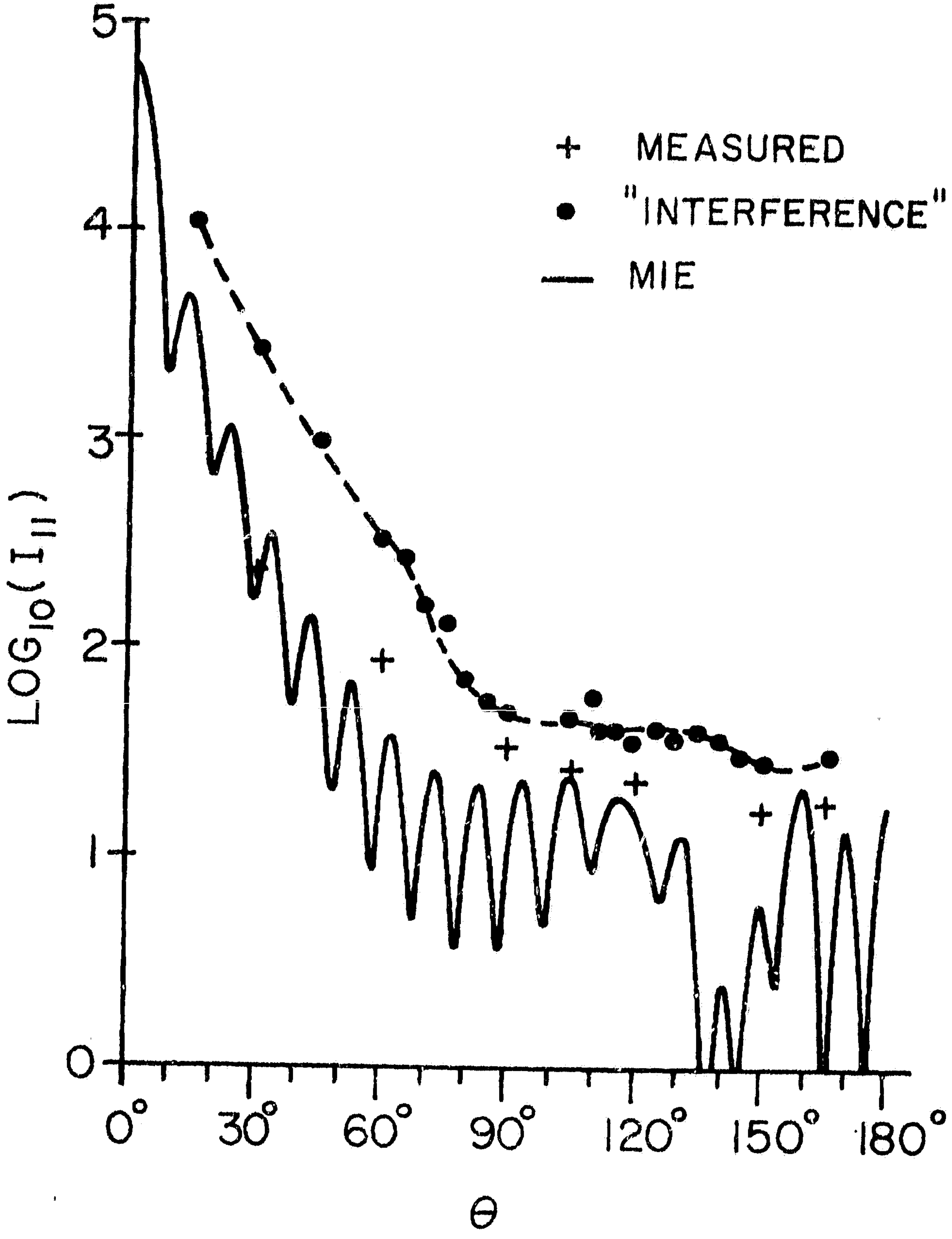

Fig. 4.34 Theoretical and experimental intensities versus scattering angle for the ensemble IC4d consisting of 80 randomly located and orientated core-mantle cylinders with $x_c = 0.78$, $x_m = 2.45$ and close to 2:1 elongation within an $X = 19.29$ "sphere". I_{11} is the intensity for radiation polarized perpendicular to the scattering plane. Solid curve is the Mie theory result for the ensemble treated as a homogeneous sphere with an equivalent index of refraction (see equation 3.1); dashed curve is for the ensemble scattering treated coherently and averaged statistically using the single scattering "interference" theory (see text for explanation) the scattering by individual cylinders was determined experimentally and is shown separately in Fig. 4.29; crosses are the experimental results for the ensemble.

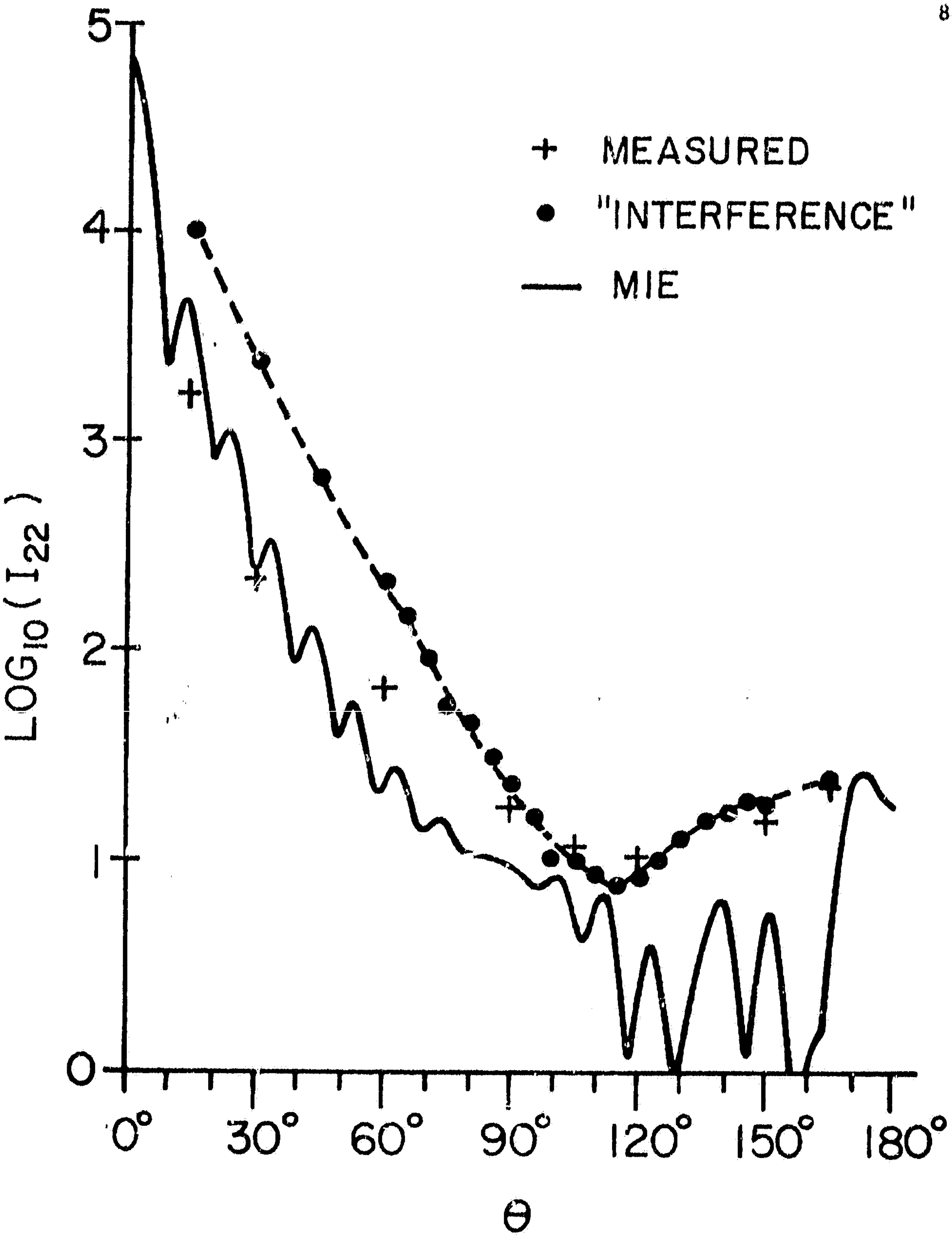

Fig. 4.35 Same as Fig. 4.34 except I_{22} is the intensity for radiation polarized in the scattering plane.

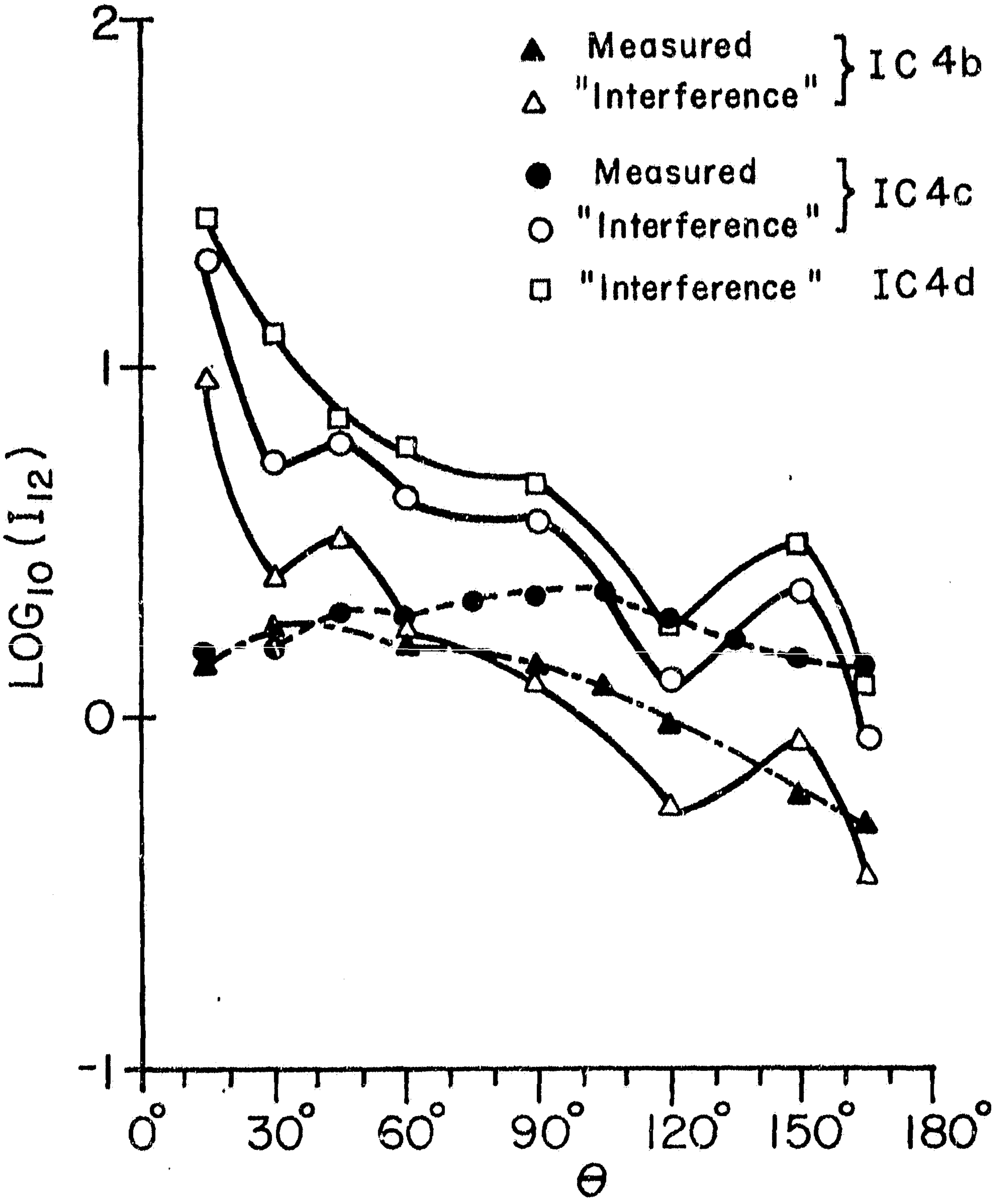

Fig. 4.36 Theoretical and experimental results for the cross-polarized intensities versus scattering angle. The open triangles are for the ensemble scattering treated coherently and averaged statistically using the single scattering "interference" theory (see text for explanation).

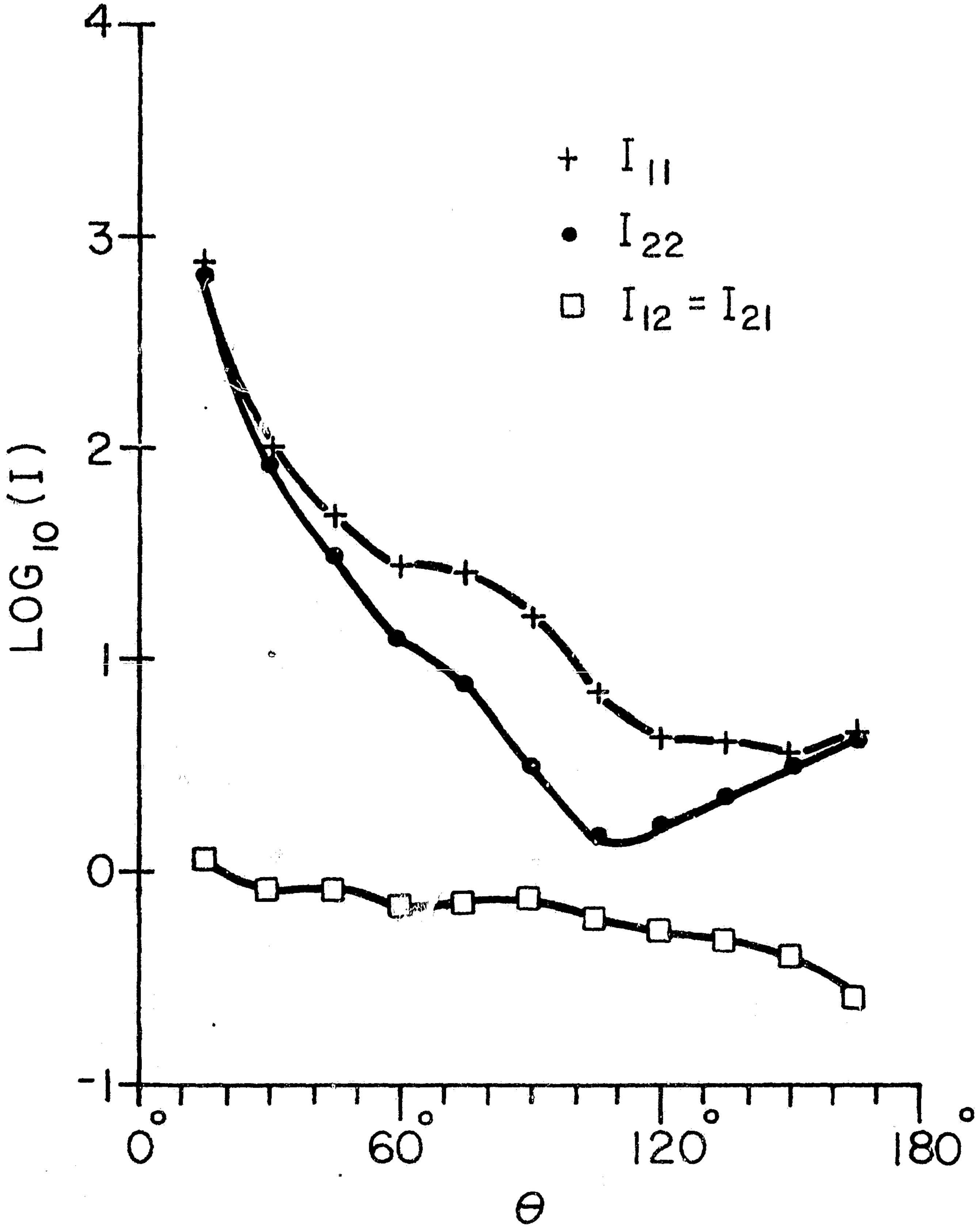

Fig. 4.37 Measured polarized intensity components versus scattering angle for target ID.; IC3b consisting of 40 $x_c = 0.63$, $x_m = 1.95$, lucite core, eccofoam 1.7 mantle cylinders with mean elongation 2.01:1 in an $X = 12.65$ "spherical" ensemble.

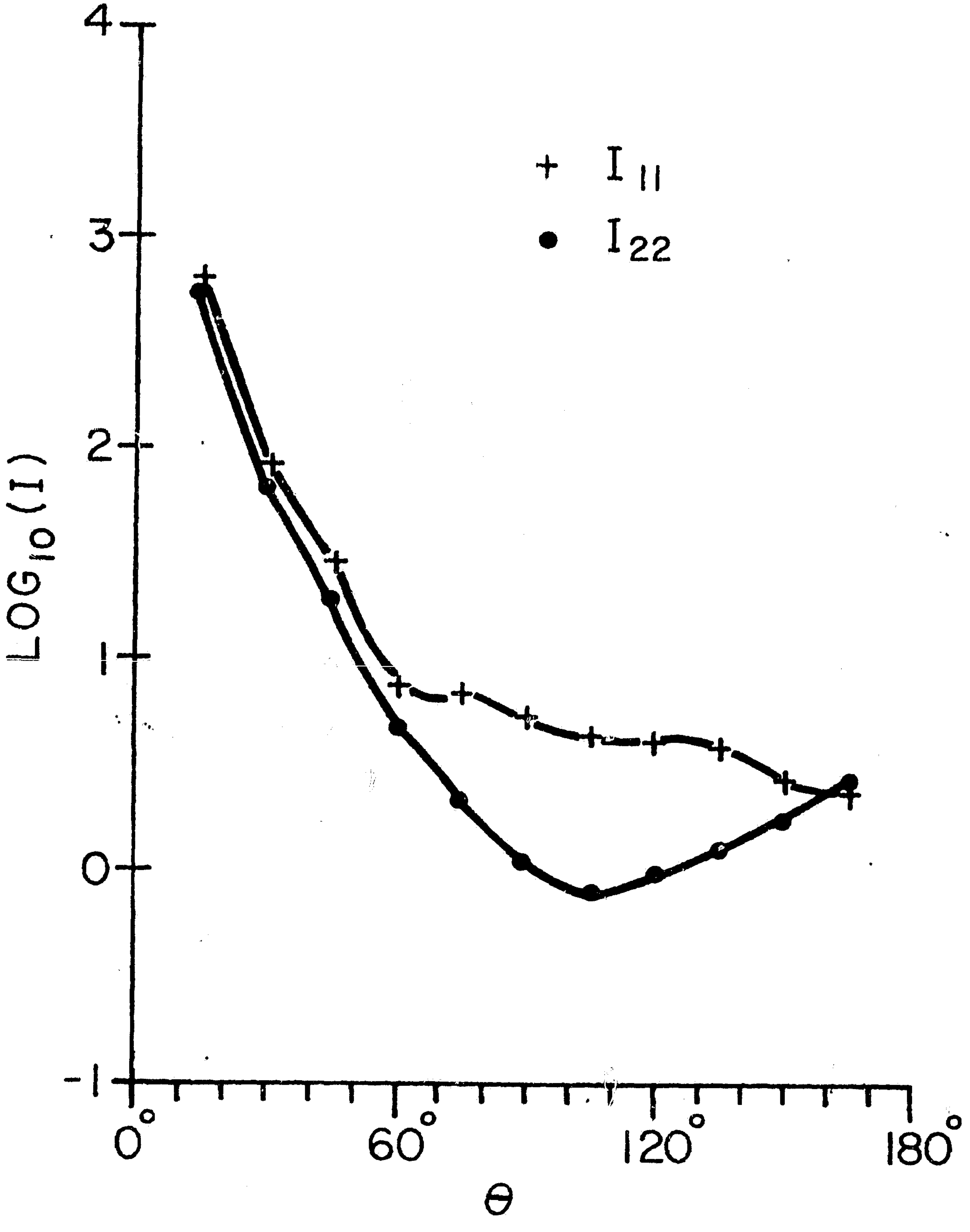

Fig. 4.38 Measured polarized intensity components versus scattering angle for target IC1a consisting of 243 x = 0.47, 2:1 elongation lucite cylinders and "waste" material from the manufacturing of the eccofoam 1.7 (m ≈ 1.3) mantles, in an X = 10.04 "spherical" ensemble.

Chapter 5

COMPARISON WITH ASRTRONOMICAL OBSERVATIONS

5.1 Introduction

Observations of comets as well as of the zodiacal light yield information about the sum of scattered intensities off the contributing scatterers, integrated along the line of sight. The geometry of the system in which the observations are made are related to the laboratory system as shown in fig. 5.1. The translation of observable quantities between the two systems is not readily made and is discussed elsewhere (see Dumont 1976 for references). ε is the angle between the direction to the light source and the line of sight. The plane defined by the location of the observer, scatterer and the Sun which is approximately a point source, is the scattering plane with respect to which the direction of polarization is defined (see section 2.3).

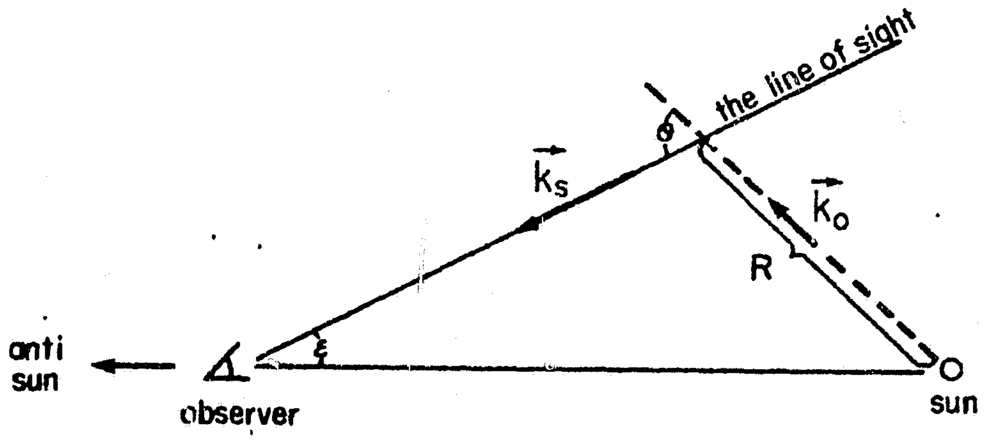

Fig. 5.1 The geometry for observations of scattering by particles in the interplanetary medium.

The widest coverage in angular (θ) distribution is found in zodiacal light measurements. Translation of the observations into quantities that can be measured in the laboratory involves assumptions regarding the particle number density distribution in the scattering plane. It has traditionally and for simplicity been assumed that the particle number-density (n) is proportional to a power of heliocentric distance R ($n \propto R^{-\nu}$) and that the light scattering functions are independent of location. As pointed out by Schuerman (1980), this last assumption has no theoretical support whatsoever. On the contrary, a segregation is expected as a function of heliocentric distance. Bearing in mind that these assumptions are not verified by observations from the Pioneer 10 spacecraft (Schuerman, 1980, refered to above) we might compare the angular dependence of the brightness (I_{tot}) and degree of polarization (P) of the zodiacal light per unit volume to the laboratory data for our models of cometary debris. The most complete surveys of the zodiacal light along the ecliptic were transformed to the laboratory geometry by Dumont (1976).

5.2 Comparison to the Zodiacal light

The zodiacal light has been found to have approximately the colour of the Sun (for references see Weinberg and Sparrow, 1978). We are therefore first discussing the general characteristics of the zodiacal light in sections 5.2.1 and 5.2.2, while colour effects are discussed in section 5.2.3. Figures 5.2 and 5.8 are reproduced from Dumont (1976) by permission from Springer-Verlag.

5.2.1 Brightness

The total brightness ($I_{\text{tot}} = I_{11} + I_{12} + I_{22} + I_{21}$) deduced by Dumont from measurements at Haleakala (Weinberg, 1964) and Tenerife (Dumont 1965, Dumont and Sánchez 1975), is shown in Fig. 5.2 where $\nu = 1.2$ was used. I_{tot} reaches a local maximum at $\theta \approx 33^{\circ}$ and becomes roughly isotropic from 50° to 130° after which it rises in backscattering. The local maximum at 33° scattering angle is shown in greater detail by Dumont (1976 fig. 5).

Although appearing in both the Tenerife and the Haleakala data, and making a smooth connection to the rocket data by Leinert et al. (1974) that probes the local minimum around $\theta = 20^{\circ}$, the very existence of the peak is dubious. This is both because the accuracy of the inversion method and the reliability of the observations decrease with scattering angle. This region is labeled poorly reliable by Dumont. It is, however, noteworthy that a similar peak is seen in the laboratory data for target T41A. It is also predicted by the "interference" theory for most "bird's-nest" particles, but the angular resolution of the laboratory data is too low to more than hint at its existence (see figures 5.3 to 5.6).

(A second peak around $\theta \approx 55^\circ$ in the data for T41A is also seen in Dumont's Fig. 3, 1975.) Dumont (1976) writes;

> "The variations of σ from $\theta = 50^\circ$ to $\theta = 130^\circ$ are probably within a factor of 2, and this conflicts with many theoretical scattering functions which show variations by a factor of 5 to 10 in the quoted range of scattering angle."

σ is the total brightness (I_{tot} in this text). Most of the laboratory data were taken with 15° intervals, so that I_{tot} was measured at $\theta = 45^\circ$, 60° and 120°, 135° but not at 50° and 130°. It is seen in table 2 that scattering by "bird's-nests" is generally closer to isotropy in this range than scattering by individual cylinders and that the agglomerates of cylinders with eroded mantles have a flatter run of I_{tot} with θ in this region than the agglomerates of "ice" coated cylinders. Dumont estimates the variation in the whole interval of $\theta = 20^\circ$ to 180° to be within a factor of 5, and writes;

> "Such a flatness can agree with few of the scattering functions reported by Wickramasinghe (1973) for Mie particles, or by Giese (1970, 1971), Giese et. al. (1974) for elaborate mixtures of homogeneous or mantle-core particles: most of these curves exhibit a much stronger forward scattering. Some agreement may perhaps be sought with absorbing particles, for which the ratio $\sigma_{max} / \sigma_{min}$ is generally of the order of 10 in the $20^\circ < \theta < 180^\circ$ range, but can be as low as 2 or 3. On the other hand, the curves of figs 4 and 5 seem very hard to reconcile with dielectric particles, for which the same ratio is between 20 and 200 or more."

Fig. 4 in Dumont's article is here Fig. 5.2, the 10° to 60° range is shown in more detail in Dumont's Fig. 5. Although none of the scattering functions for the "bird's-nests" actually investigated in the laboratory show quite such an isotropy in this range of scattering angle, we note that some agglomerates that are dielectric as are all "bird's-nests" reported on in this study, show $I_{max} / I_{min} < 5$. Agglomerates of more realistic sizes for typical zodiacal-light particles are currently being studied, using the "interference" theory.

In the backscattering region $160^\circ < \theta \leq 180^\circ$ there is a rise in I_{tot} (Fig. 5.2). Dumont estimates the ratio $I_{tot}(180^\circ) / I_{tot,min}$ to 1.7 for the Tenerife data and to 1.9 for the Haleakala data. A rise with a corresponding slope is evident in several of the scattering functions for "bird's-nests", where $1 < I_{tot}(165^\circ) / I_{tot,min} \lesssim 1.3$ (see Figs. 5.3 to 5.6).

In agreement with Dumont's Fig. 6 in the same reference, the I_1 component ($\perp$ in Dumont's Fig.) is flatter than the I_2 component (//) for all "bird's-nests" in this study.

TABLE 2

Target Id. #	type of cylinders single	 agglomerate	 homogeneous	 core-mantle	range in θ (degrees)	$I_{tot,max}$ / $I_{tot,min}$ less than
T11R		X	X		45 - 135	13
					60 - 135	5.6
T21R		X	X		45 - 135	3.5
					60 - 135	2.5
T41R		X	X		45 - 135	2.5
					60 - 135	1.5
TC21R		X	X		30 - 150	11
					60 - 150	3
V21R		X	X		45 - 135	3
					60 - 135	2
12	X			X	45 - 135	30
					60 - 135	10
IC4b		X		X	30 - 150	22
					60 - 150	7
IC4c		X		X	45 - 135	9
					60 - 135	5
IC4d		X		X	30 - 150	15
					60 - 150	5
IC3b		X		X	45 - 135	12
					60 - 135	7
IC1a		X			45 - 135	10
					60 - 135	2.5
C41R	X		X		45 - 135	13
					60 - 135	5

(continue)

TABLE 2 (continue)

Target Id. #	single	agglomerate	homogeneous	core-mantle	range in θ (degrees)	$I_{tot,max} / I_{tot,min}$ less than
T41A		X	X		50 - 130	4.5
U41A		X	X		60 - 150	2.5
					30 - 150	4.5
U41R		X	X		60 - 135	3
					45 - 135	3.5
C41R	X		X		45 - 135	13
					60 - 135	5
B11R		X	X		50 - 130	2.5
B21R		X	X		50 - 130	2.3
B41R		X	X		50 - 130	3

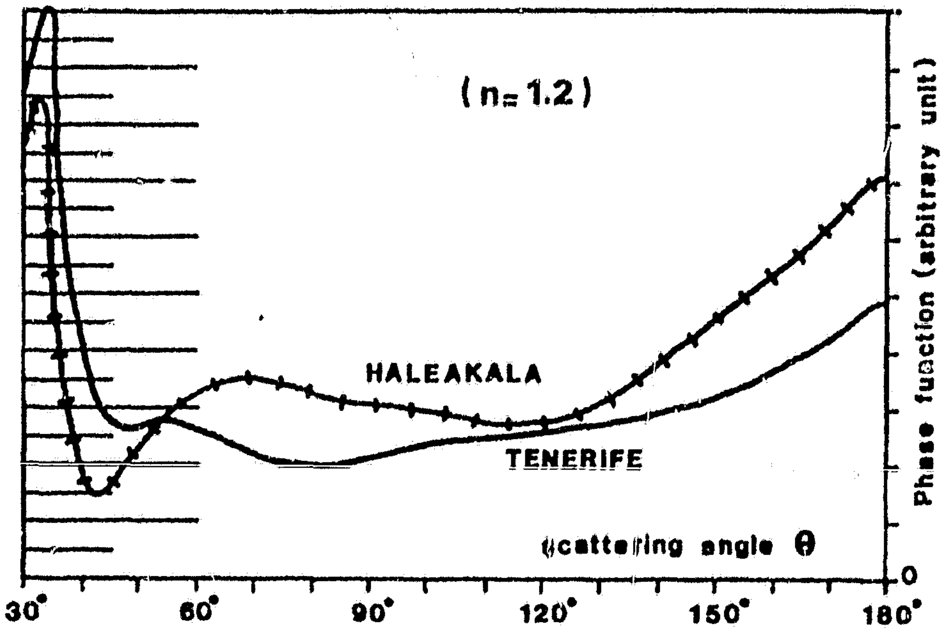

Fig. 5.2 Reproduced by permission given by Springer-Verlag, from Dumont (1976, Fig. 4, p. 92). The phase function for interplanetary dust deduced from the Tenerife (Dumont 1965, Dumont and Sánchez 1975) and Haleakala (Weinberg, 1964) photometric surveys. The number density n given by $n \propto R^{-\nu}$ where R is the heliocentric distance and $\nu = 1.2$ was assumed.

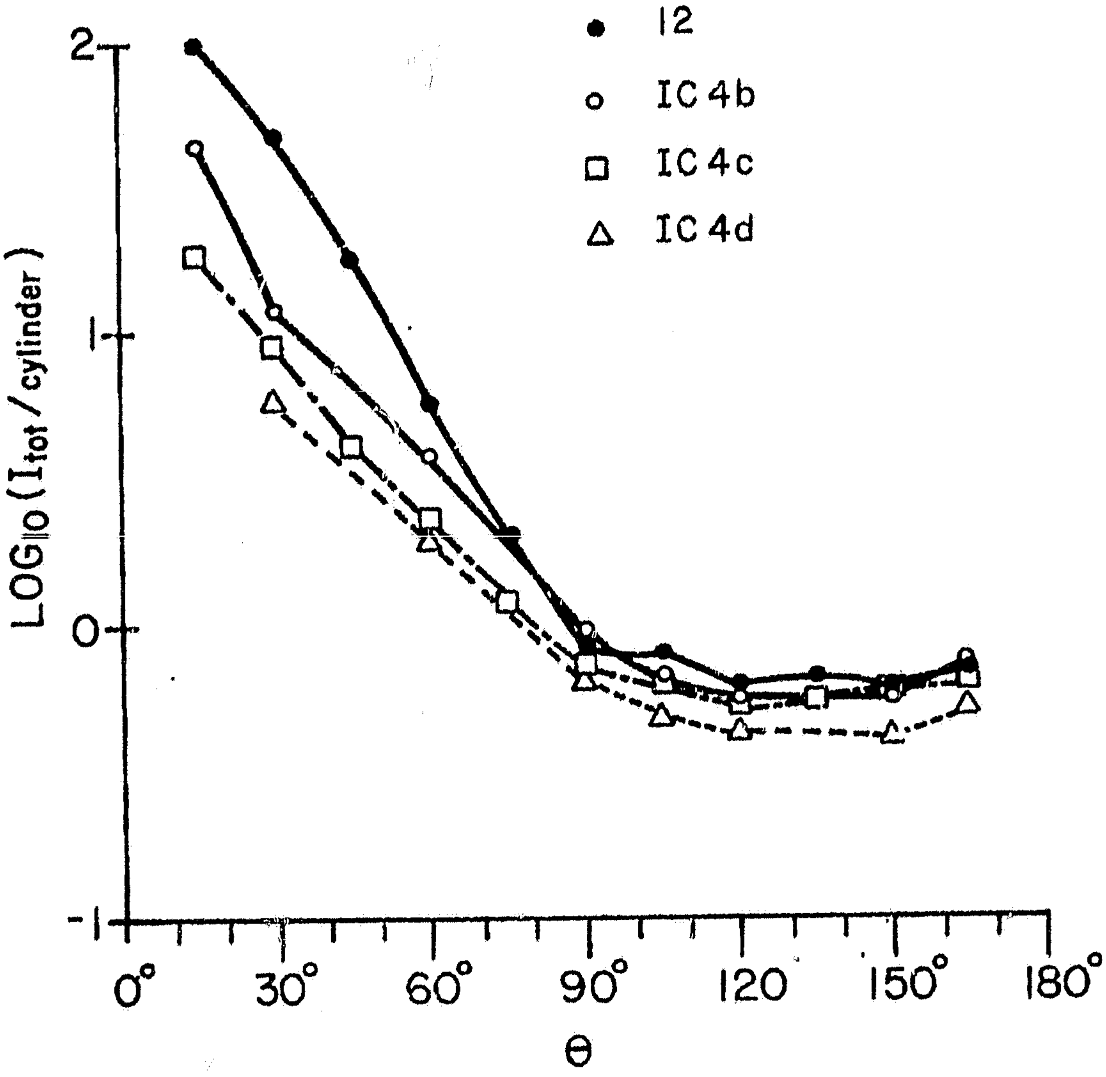

Fig. 5.3 Measured total brightness per cylinder versus scattering angle for the single core-mantle grain "12" and the agglomerates IC4b, IC4c and IC4d of similar grains. For target parameters see the fold out page. The connecting curves are added for illustration purposes only.

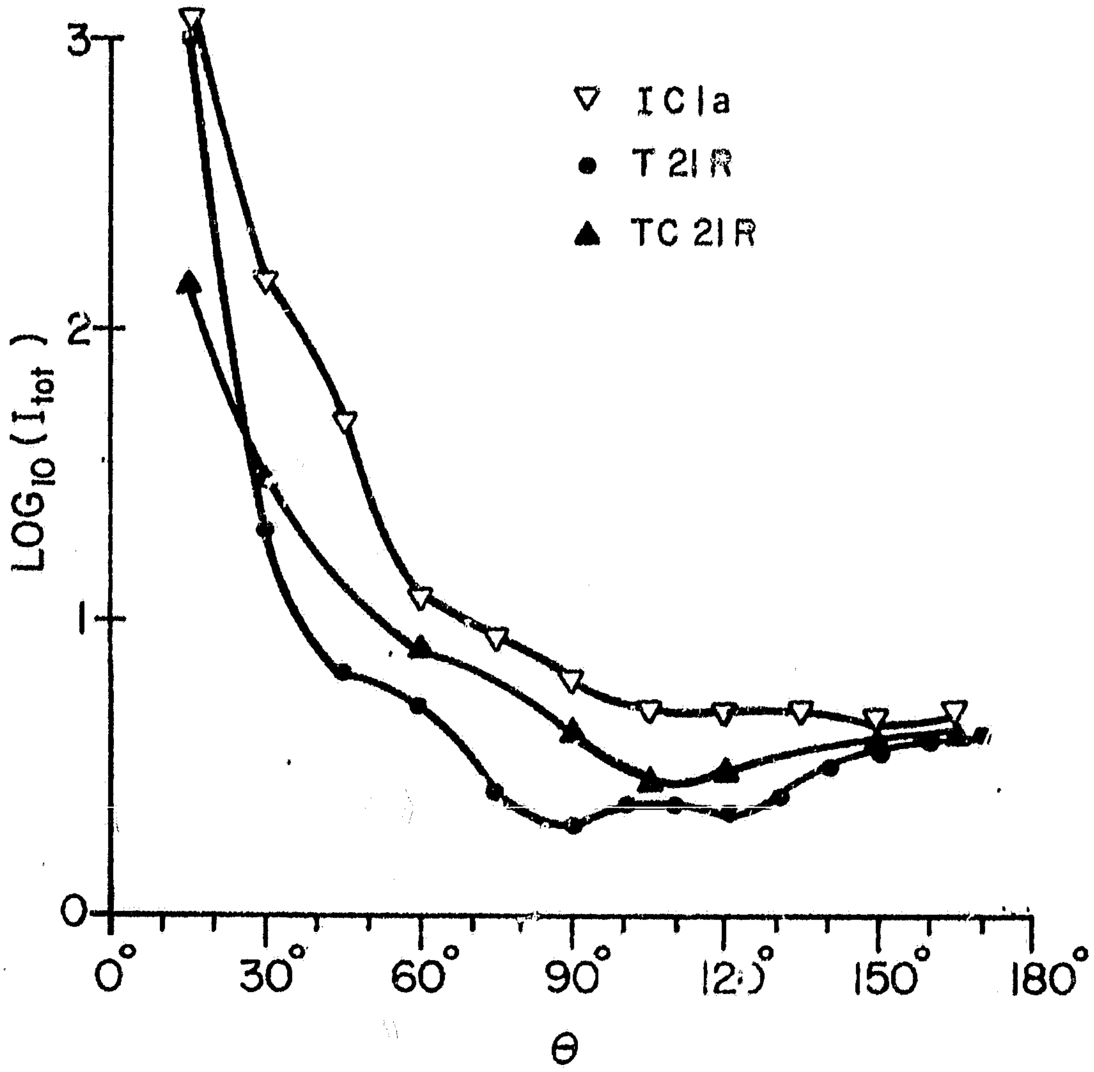

Fig. 5.4 Measured total brightness versus scattering angle for agglomerates TC21R and T21R differing in the silicate grain number-density and for the agglomerate IC1a containing a mixture of silicate cylinders and "ice"-type material. See the fold out page for target parameters.

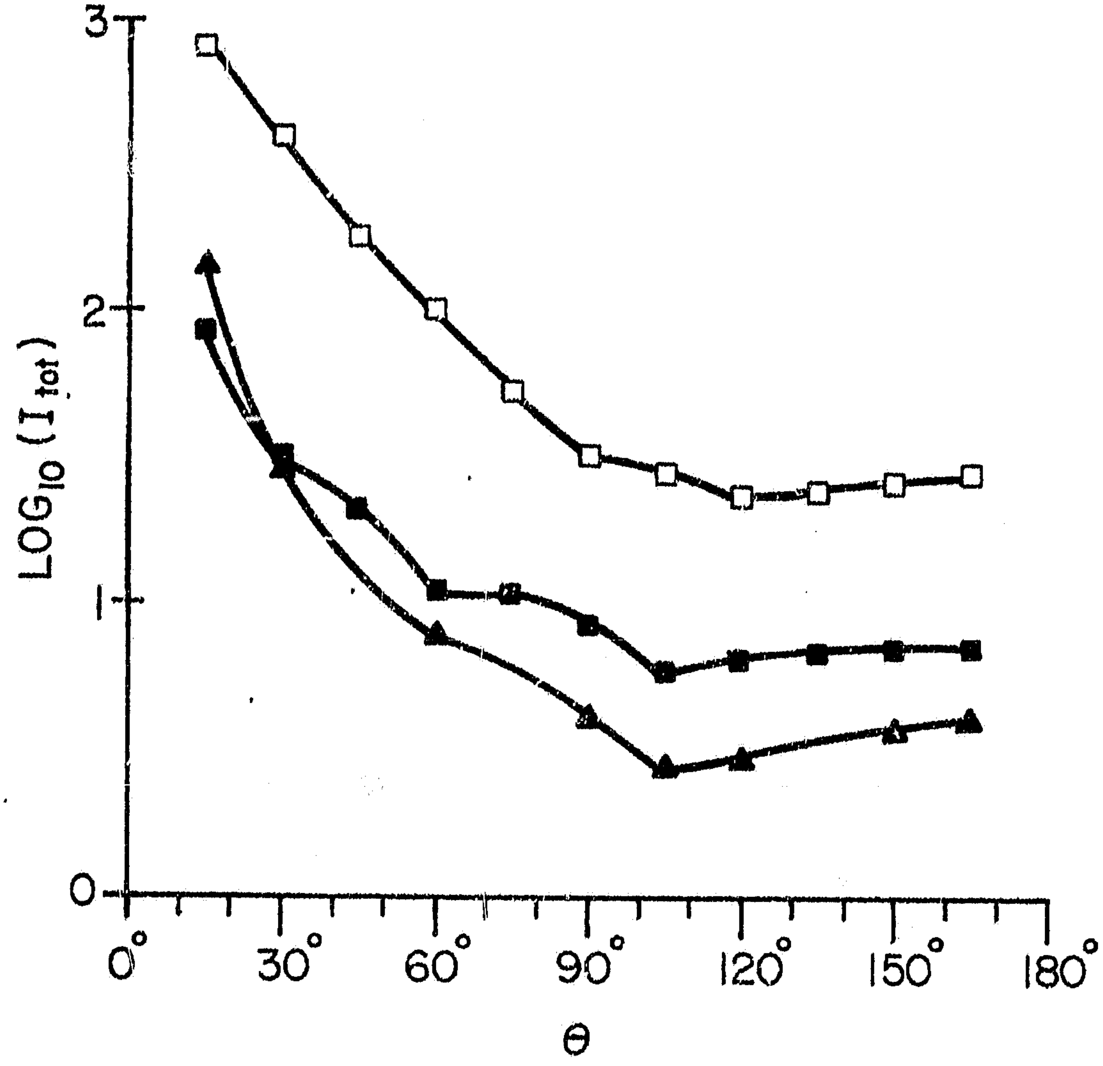

Fig. 5.5 Measured total brightness versus scattering angle for the equal volume "bird's-nests" TC21R; triangles, V21R; squares and IC4c; open boxes. See the fold out page for target parameters.

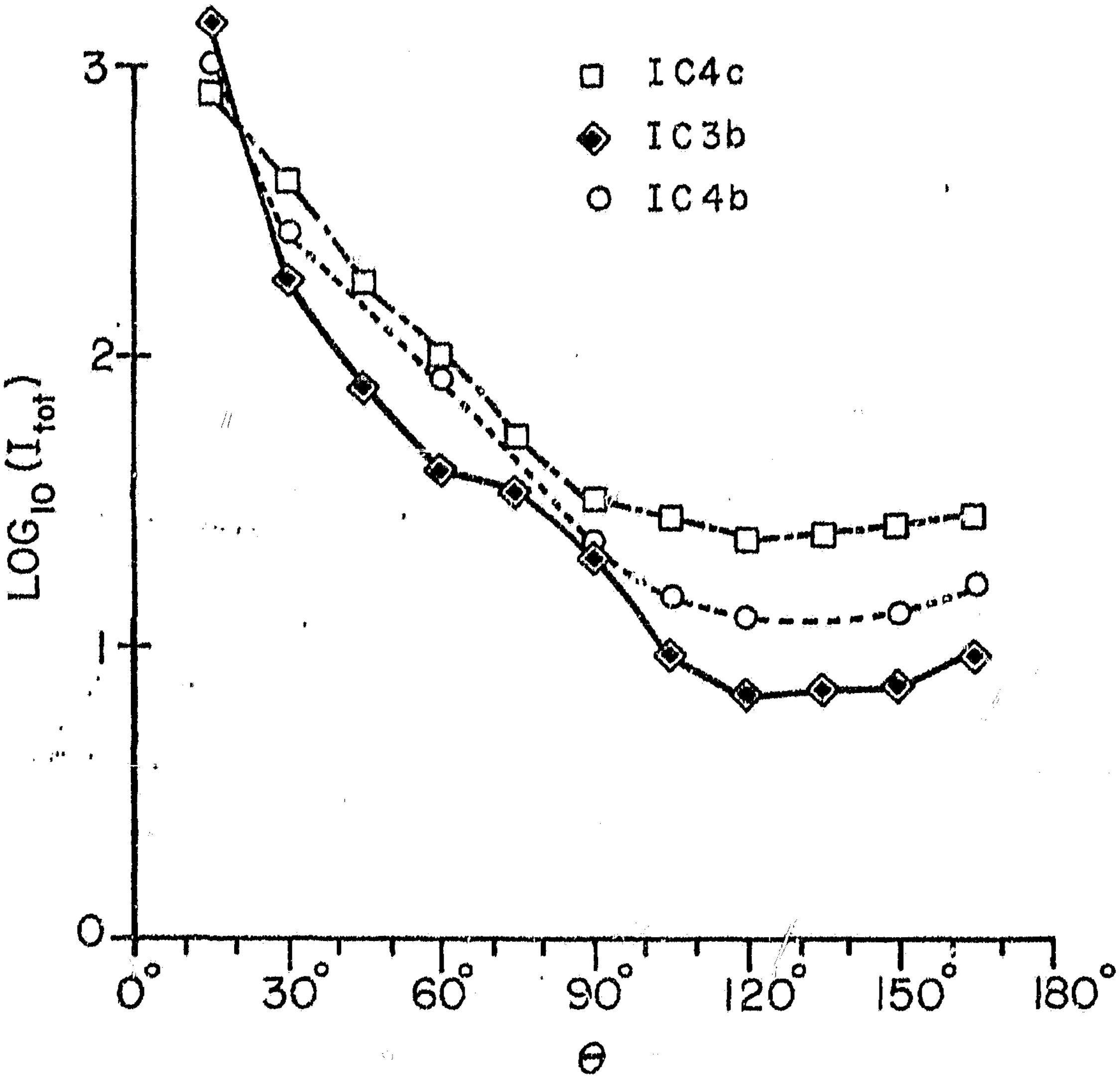

Fig. 5.6 Measured total brightness versus scattering angle for the agglomerates IC4b, IC3b and IC4c consisting of core-mantle cylinders. For target parameters see the fold out page.

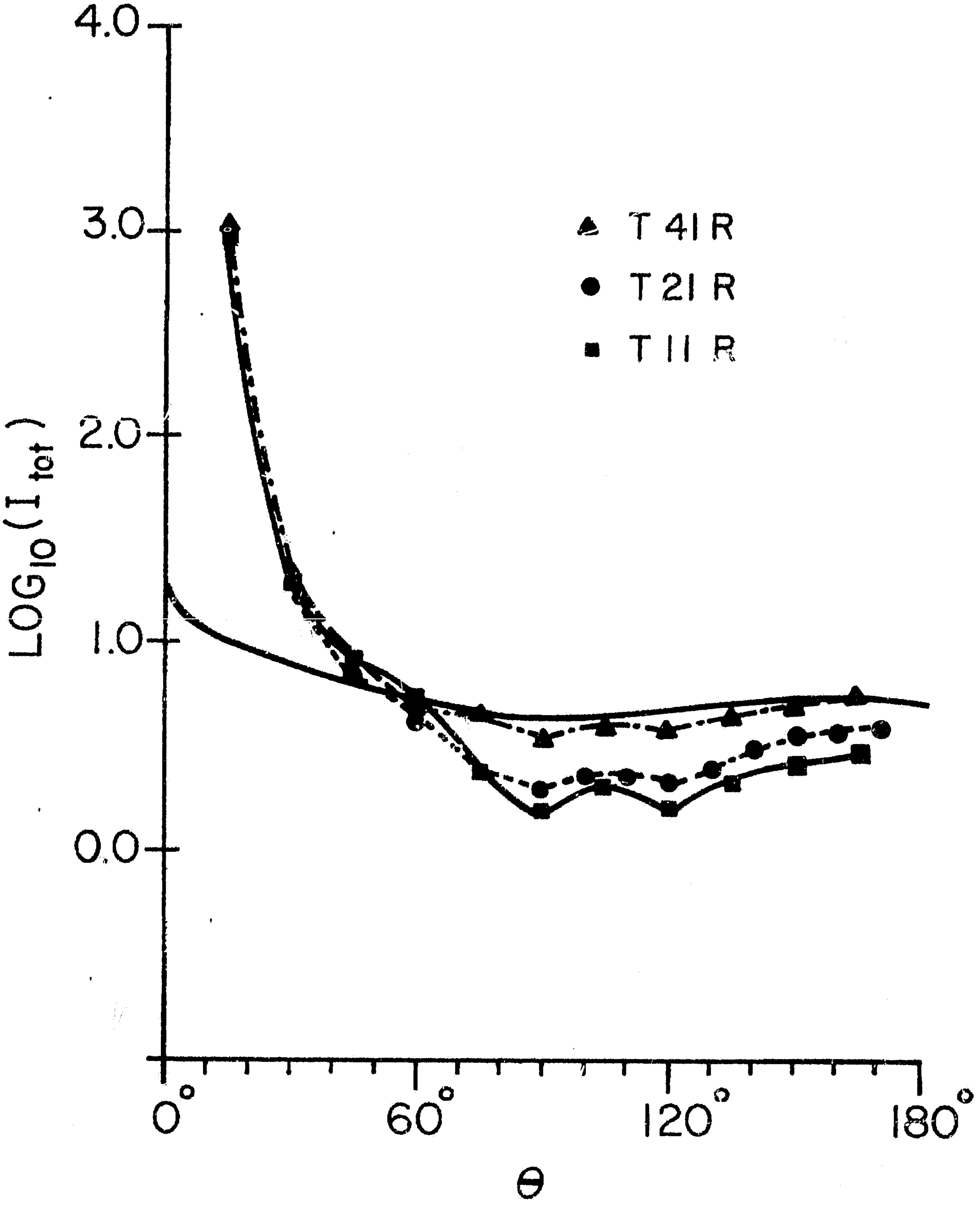

Fig. 5.7 Measured total brightness versus scattering angle for the ensembles T41R, T21R and T11R consisting of $x = 0.47$ silicate type material cylinders, differing only in elongation. For target parameters see the flod out page. The solid line is the theoretical computation of the scattered brightness from an equal mass portion of an $x = 0.47$, $m = 1.618 - 0.005i$, infinite cylinder averaged over "random" orientations.

5.2.2 Degree of Polarization

The similarly deduced degree of polarization ($P(\theta)$) is less sensitive to the value assigned to ν than the photometric curves (Dumont and Sánchez, 1975, fig. 5). In fig. 5.8 $P(\theta)$ is reproduced from Dumont (1976, fig. 7), where the same value for ν (1.2) is used as for inversion of the intensities. P is generally positive at $\theta > 60^{\circ}$, the apparent large negative degree of polarization from the Haleakala data in the poorly reliable left part of the figure is not believed to be genuine by Dumont. From Dumont's fig. 6 it appears that both curves join in a neutral point at $\theta \approx 35^{\circ}$. The maximum degree of polarization, $P_{max} \approx 0.4$ occurs close to $\theta = 90^{\circ}$ in the Haleakala inversions and closer to 80° for the Tenerife data, with $P_{max} \approx 0.35$. The values of these curves at $\theta = 90^{\circ}$ and $\theta = \varepsilon_m$ are of special importance because they are independent of ν (Dumont 1972, 1973). ε_m is the elongation of the maximum degree of polarization, $55^{\circ} - 75^{\circ}$.

It can be seen in fig. 5.9 to 5.13 that the general shape of these curves are reproduced by the "bird's-nests". P is generally positive, the magnitude is close to that measured for the agglomerates IC4b, IC4c and IC4d (fig. 5.9) of "ice"-coated silicate, for which the two points $P(\varepsilon_m)$ and $P(90^{\circ})$ are in excellent aggreement with the observations. The maximum however occurs at higher θ's but is expected to shift towards smaller θ's with the Fraunhofer diffraction as the "bird's-nests" size increases. P_{max} for all the agglomerates with eroded mantles is substantially higher than those of fig. 5.8 but the maximum occurs closer to P_{max} in the inverted observations.

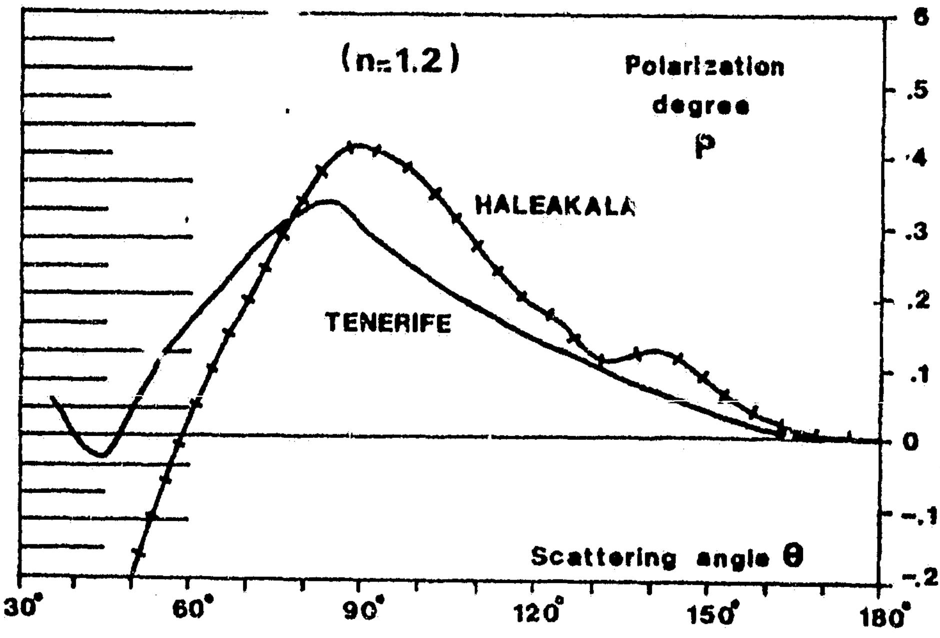

Fig. 5.8 Reproduced by permission given by Springer-Verlag, from Dumont (1976, Fig. 7, p. 95). The degree of polarization versus scattering angle for interplanetary dust deduced from the Tenerife (Dumont 1965, Dumont and Sánchez 1975) and Haleakala (Weinberg, 1964) photometric surveys. A number density n given by $n \propto R^{-\nu}$ where R is the heliocentric distance in A.U. and $\nu = 1.2$ was assumed. The left side of the figure is labelled poorly reliable by Dumont.

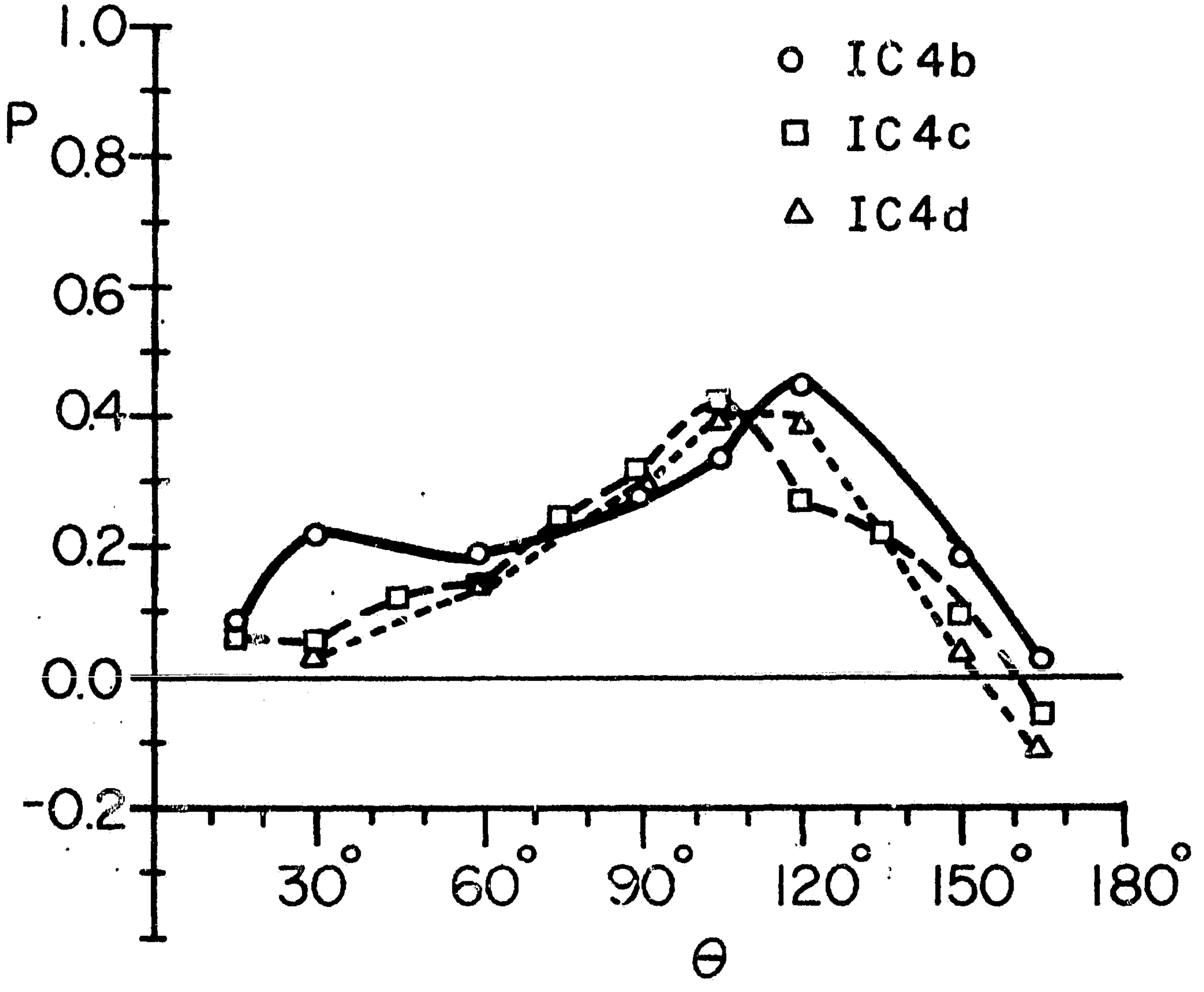

Fig. 5.9 Measured degree of polarization versus scattering angle for the ensembles IC4b, IC4c and IC4d of similar core-mantle cylinders. See the fold out page for target parameters.

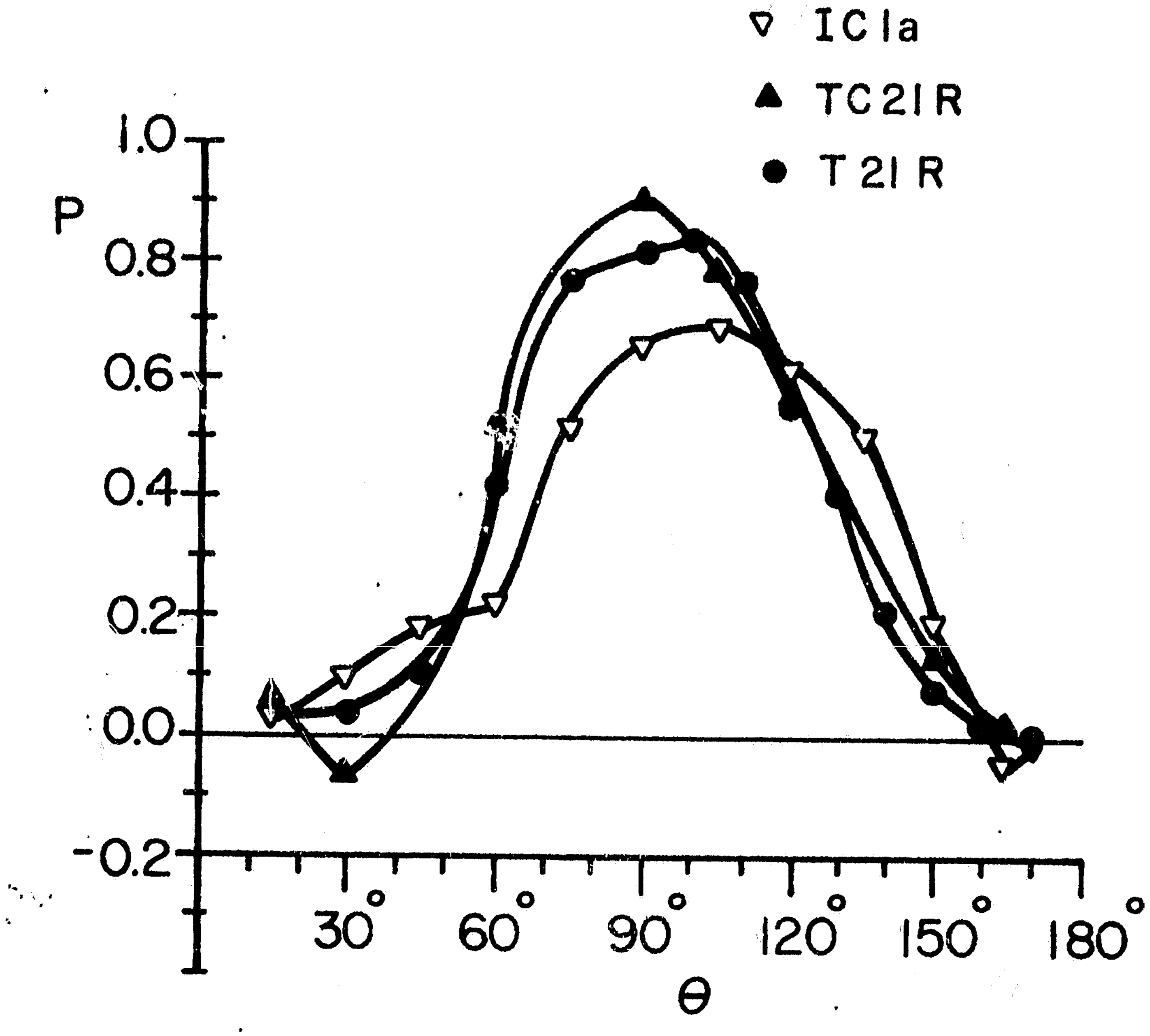

Fig. 5.10 Measured degree of polarization versus scattering angle for agglomerates TC21R and T21R differing in the silicate grain number density and for the agglomerate IC1a containing a mixture of silicate cylinders and "ice"-type material. See the fold out page for target parameters.

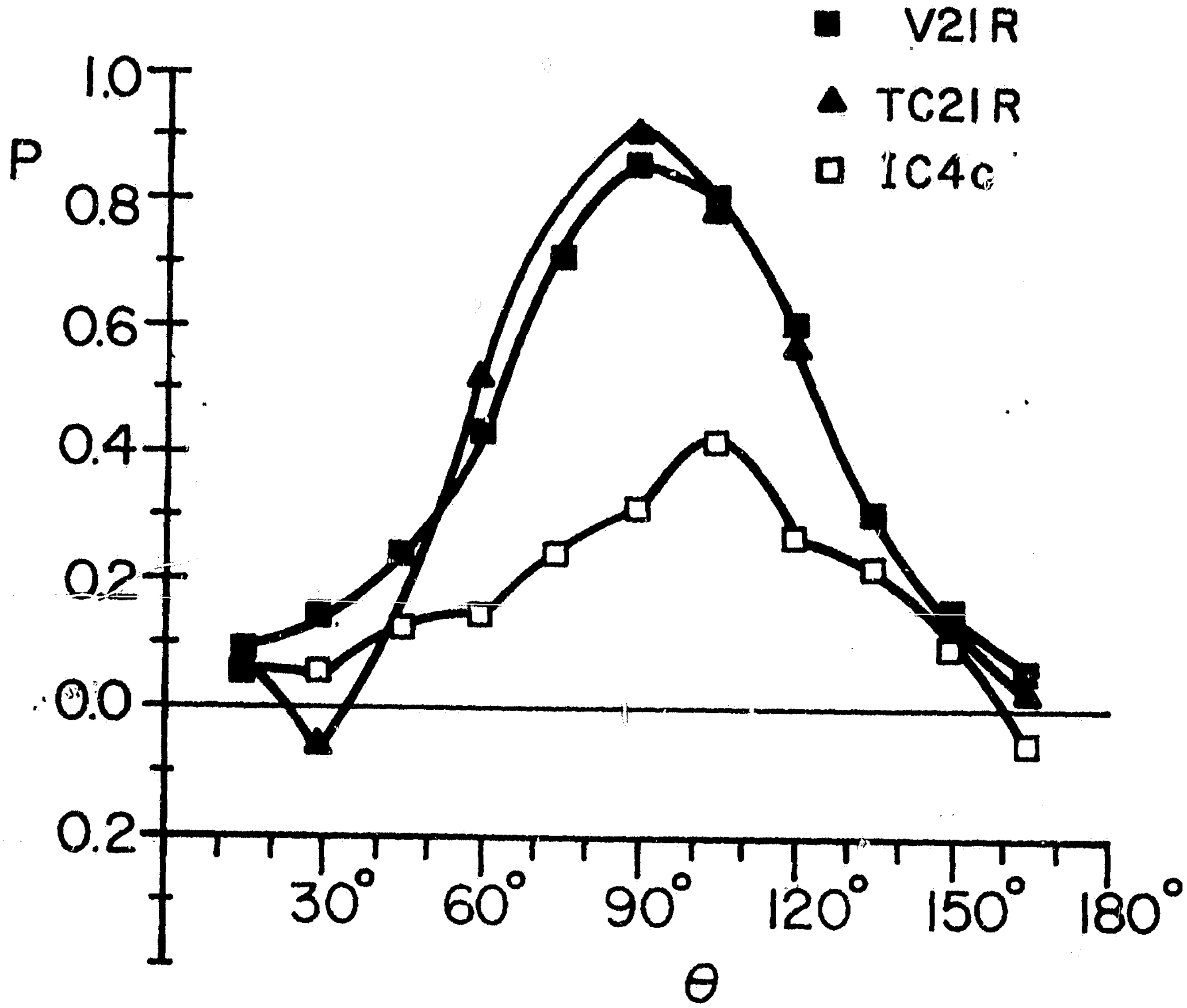

Fig. 5.11 Measured degree of polarization versus scattering angle for the equal volume "bird's-nests" TC21R, V21R and IC4c. See the fold out page for target parameters.

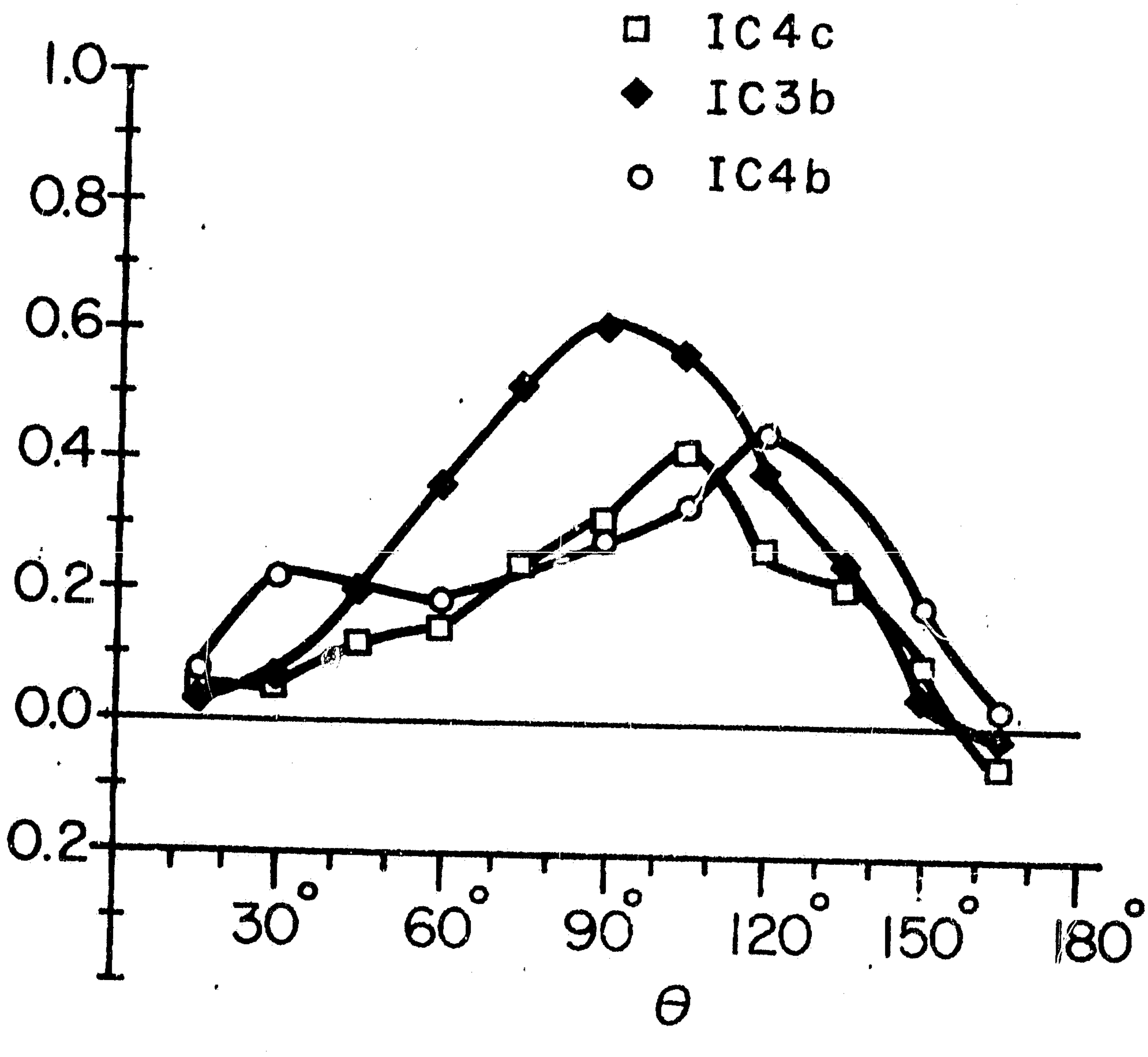

Fig. 5.12 Measured degree of polarization versus scattering angle for the agglomerates IC4c, IC3b and IC4b, of "core-mantle" cylinders. For target parameters, see the fold out page.

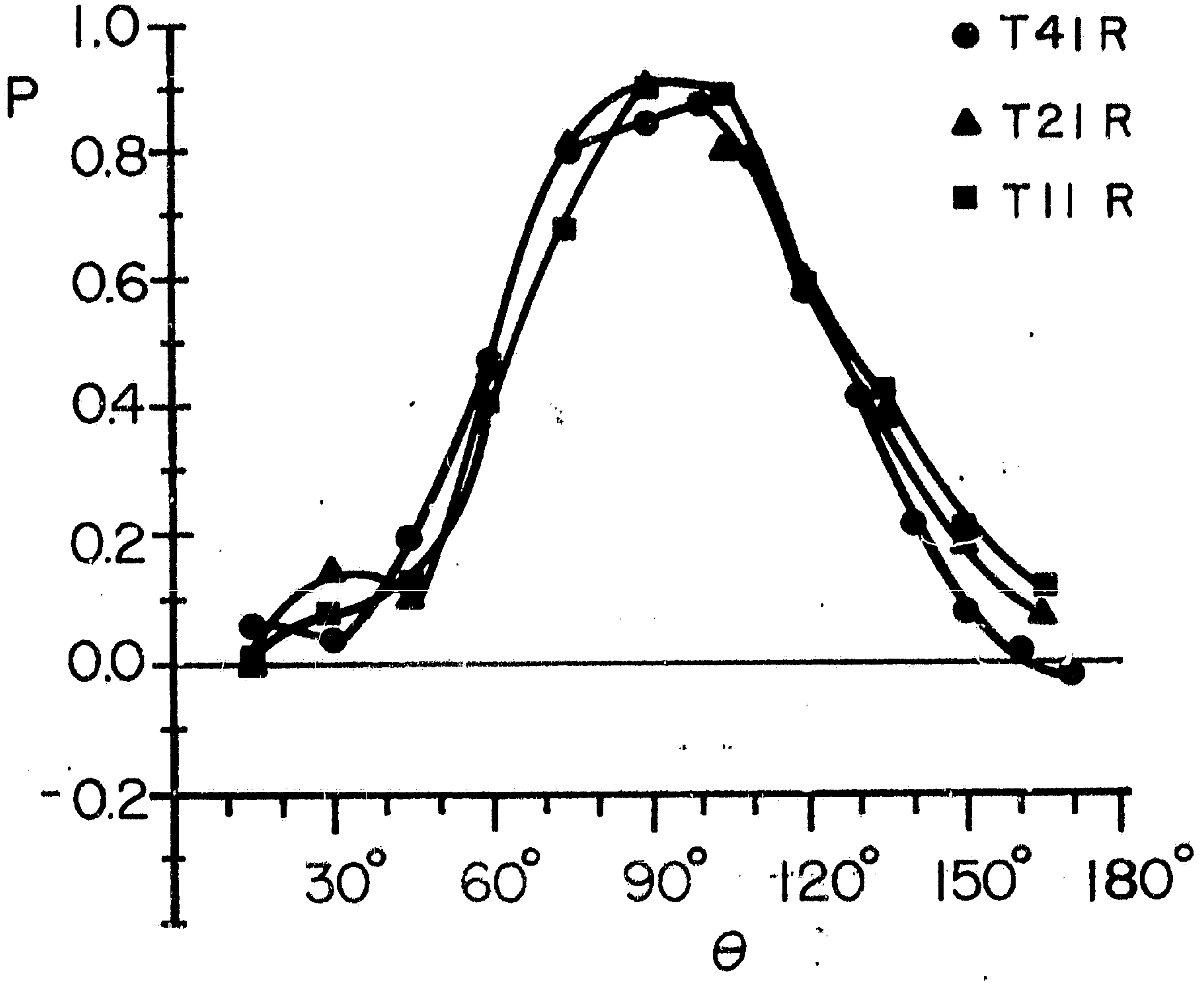

Fig. 5.13 Measured degree of polarization versus scattering angle for the ensembles T41R, T21R and T11R of x = 0.47 silicate cylinders, differing only in elongation. For target parameters, see the fold out page.

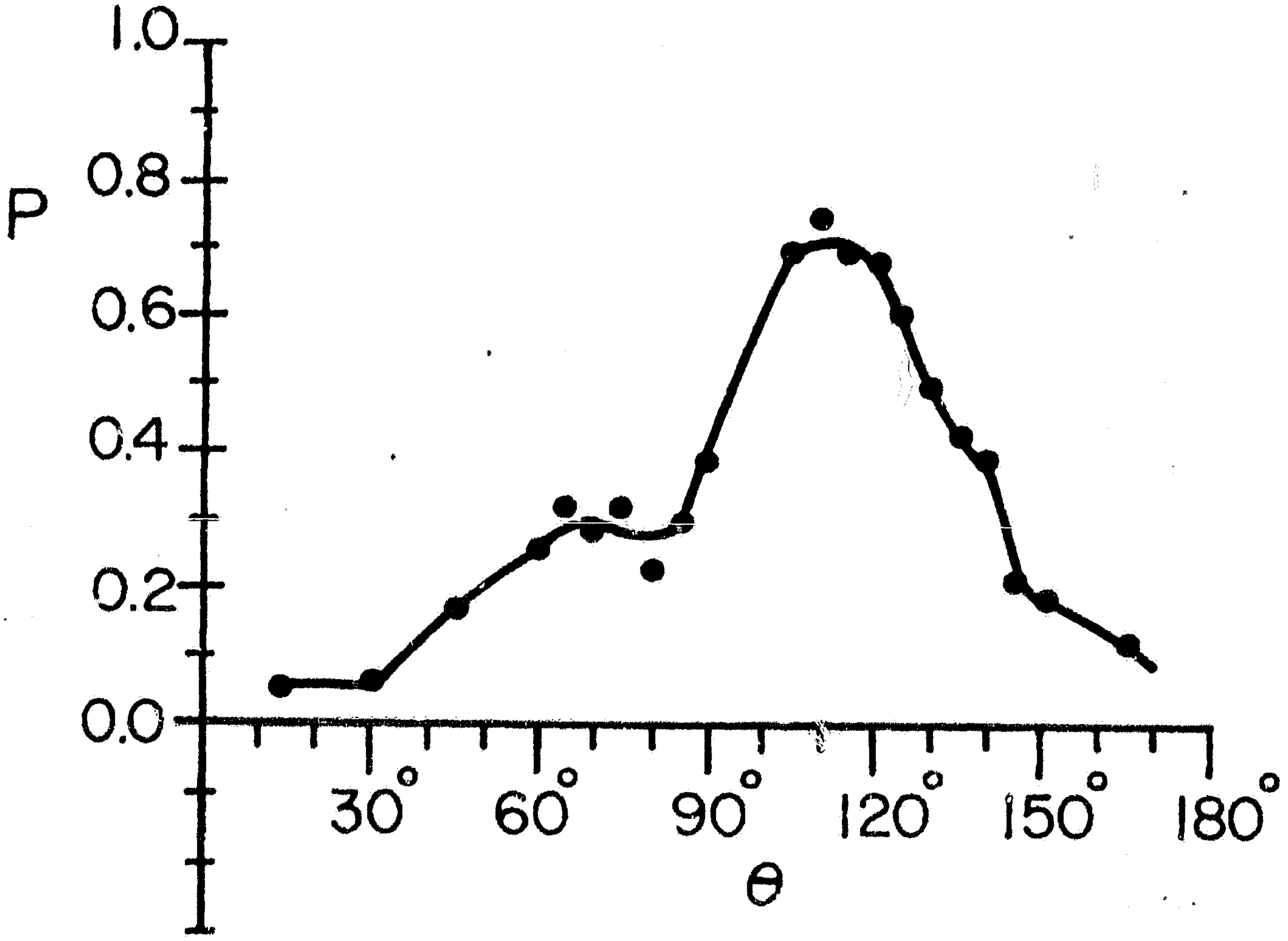

Fig. 5.14 Measured degree of polarization versus scattering angle for the single silicate-core - "ice"-mantle cylindrical model of an interstellar grain. See the fold out page for target parameters.

5.2.3 Colour

If the diameter 0.1 μm is assigned to the silicate cores, targets IC4b, IC4c, IC4d and V21R models scattering of $\lambda = 0.4$ μm light, IC3b scatter at $\lambda = 0.5$ μm and IC1a, T11R, T21R, T41R and TC21R all scatter 0.7 μm light. Pure colour is represented in fig. 5.6, both IC4c and IC3b correspond to 2 μm diameter agglomerates of 44 interstellar grains. The colour is generally blue, $I_{0.4}/I_{0.5} \approx 3$. If the agglomerates reach sizes that are currently believed to be more realistic for typical zodiacal-light particles (10-100 μm), the size parameter of the individual particles might be optically more important than the size parameter of the agglomerates. Note that in the limit where the particles become homogeneous, scattering by Mie-particles with a given index of refraction is almost colourless in this size range. We have therefore also compared the scattering from ensembles of equal-size parameter X while the size x of the individual grains is varied. I_{tot} from IC3b and IC4b, both with ensemble size parameter $X = 12.65$ are also compared in fig. 5.6 where it is seen that the 23 larger cylinders scatter more light than the 44 smaller grains in IC3b. It appears therefore that the blue light ($\lambda = 0.4$ μm) is scattered more efficiently than green ($\lambda = 0.5$ μm) light, $I_{0.4}/I_{0.5} \approx 2$. The degree of polarization (fig. 5.12) is lowest in the blue light (IC4c and IC4b) the position of the maximum $\theta_{m,\,0.4} \approx 120^{\circ}$ is shifted to $\approx 90^{\circ}$ at $\lambda = 0.5$ μm. The agglomerates TC21R and V21R of bare cylinders both have $X = 15.81$ in $\lambda = 0.7$ μm (red) light and $\lambda = 0.4$ μm (blue) light respectively. Similarly to scattering by IC4b compared to IC3b, I_{tot} is higher for V21R than for TC21R, $I_{0.4}/I_{0.7} \lesssim 2$, suggesting that the light scattered off the "ice" - free agglomerates also is slightly blue (fig. 5.5). On the other hand, the run of the degree of polarization looks quite similar for both ensembles (colourless) with $P_{max} \approx 0.87$ around $\theta = 90^{\circ}$ (fig. 5.11).

Few differences in the zodiacal light observed at different visual wavelenghts are larger than variations in the same part of the spectrum between observations by different astronomers. The colour of the zodiacal light is therefore believed to be white or grey. The colours indicated by the microwave measurements might be too prominent to compare favourably with the observations. As a realistic comparison involves scattering functions over a size distribution, more microwave measurements are desirable. It seems, however, that the scattering efficiency per cylinder decreases as the agglomerates of core-mantle grains grow in size (fig. 5.3). We see in figures 4.30 to 4.35 that the I_{11} component decreases faster than I_{22} resulting in a lower degree of polarization, (fig. 5.9), approaching that of the zodiacal light.

Some astronomers have observed negative polarization at high scattering angles (Frey et al., 1974, Wolstencroft and Rose, 1967). Weinberg and Mann (1968) found that the neutral point near 160° tends to smaller elongations with increasing wavelength. Neagative polarization is seen at $\theta = 165^{\circ}$ in several of the experimental graphs for "bird's-nests".

5.3 Comets

The inversion of the brightness intergral is much simpler for comet data than for the zodiacal light because all light observed in a given direction (ε) comes from scatterers distributed in a narrow interval of the line of sight, the scattering angle (θ) is essentially constant. To the knowledge of the author, only observations of the dust tail of comet Ikeya-Seki, 1965 VIII, (Weinberg and Beeson, 1976, Matyagin et al., 1968), provide information on I_{tot} and P over an appreciable interval of θ. The angular dependence was deduced by scanning the dust tail with a photometer. It follows that in addition to the dependence on possible variations in scattering functions for particles as a function of location in the tail, affecting $P(\theta)$, the measured brightness $I(\theta)$ also depends on the particle number density distribution. ~~Weinberg and Beeson conclude from model calculations of the degreee of polarization~~ using a Mie-program, that the observations are consistent with grains in a very narrow size-distribution. Although the observed polarization is very different from that of light scattered off the single core-mantle cylinder 12 (Fig. 5.14), the grain parameters are suggestive of those used for the single core-mantle grains in this study.

Some dust properties can also be inferred from dynamical considerations. Most dust tails can be resolved in streamers or synchrones and in syndynes. Streamers coincide with the loci expected for particles ejected simultaneously from the nucleus and subjected to a particle-dependent heliocentric repulsive force $-\frac{\mu}{R^2} m_{\text{grain}}$ counteracting the gravitation. (R is the heliocentric distance and m_{grain} is the mass of the grain). Syndynes correspond to loci for continuously ejected particles with a given μ. Conclusions on the optical properties of the particles can be drown if $\mu = \beta$ is assumed, where β is the acceleration resulting from radiation pressure in units of the gravitational attraction.

Following the model suggested by Whipple (1951) and formulated by Finson and Probstein (1968), Sekanina and Farrell (1980) interpret the structure in the dust tail of comet West 1976 VI as evidence for fragmentation of strongly non-spherical particles. The parent bodies resulting from a single burst are lined up along a streamer. As the particles burst, the fragments line up in striae. Sekanina and Farrell (1980) conclude that the repulsive acceleration μ was slightly lower for the parent bodies than the "average" on fragments ranging from 0.6 to 2.7 times the solar gravitational attraction. With the assumption $\mu = \beta$, this relation, which is difficult to account for with Mie-theory, leads Sekanina and Farrell (1980) to suggest that the parent particles are chain-like agglomerates. We note, however, that β is generally not acting in the radial direction if the scatterers does not posses spherical symmetry as for elongated structures. This is easily realized by noteing that the scattering pattern is asymmetric with respect to the incident $\vec{k}_o$-vector for particles which are asymmetric with respect to this vector. We note also that the formation of discrete striae requires a distinct correlation between the fragmentation mechanism and μ. Such a correlation might be expected if μ results from interaction with the solar wind (Coulomb drag and Lorentz force, etc..) in which case each striae would correspond to a given charge-to-mass ratio for which the parent body is likely to sputter.

Preliminary studies of the dynamics have been carried out for dust assumed to be released by comet Halley during its 1986 perihelion passage. The computer code, which also includes radiation and ion pressure is described elsewhere (Gustafson and Misconi, 1979). The main effects of the solar wind interaction during that passage are to reinforce gravitation (counteract β) and to deviate the dust towards the solar equatorial plane. For silicates corresponding to the cores of interstellar grains with an assumed charge as high as 10 Volt, $\mu \approx \beta - 0.1$ and the deviation towards the equator is $\approx 20^{\circ}$. For "ice"-coated silicates the charge was estimated to 1.2 Volt, the resulting $\mu \approx \beta$ and the deviation from the comet's-orbital plane $\approx 1.5^{\circ}$ For larger agglomerates the interaction with the solar wind seems negligible.

In conclusion, the dynamics of grains with high charge to mass ratio such as might be expected for the silicate cores resulting from the striped interstellar core-mantle particles, or for the bare particles, are expected to deviate sufficiently from central motion to distinguish them from "ice"-coated grains or agglomerates. β for the parent particles are probably comparable to that for the fragments forming the striae in comet West.

We note that at the limit, where the ensemble of scatterers is such that $m_{eq} \ll \frac{\lambda}{2\pi a}$ and the scatterers are randomly located, each scatterer approaches its scattering properties as an individual particle. At this limit, β is the same for the agglomerate as for individual scatterers.

This condition is nearly fulfilled for the "ice"-free agglomerates especially V21R and TC21R.

5.4 Impact Data

Analysis of lunar rock samples (Nagel et al., 1975) reveals the existence of very shallow craters which are indicative of low bulk-density impacting particles, $\rho \approx 1$ gcm^{-3}. The relationship between particle density and crater topology has futher revealed two groups of particles stony ($\rho \approx 2 - 3$ gcm^{-3}) and metallic-density ($\rho \approx 8$ gcm^{-3}) meteoroids. The latter create deeper and much more commonly observed (selection effects?) craters (see also Le Sergeant and Lamy, 1978). Impact data from the Helios 1 spacecraft provides an independent means of seperating a low-density component of the interplanetary dust-complex. One of the Helios impact detectors was protected from direct solar radiation by a screen. The screen also prevented particles with density lower than ≈ 1 gcm^{-3} from penetrating. Another detector, with an open aperture pointing out of the ecliptic plane, registered a large excess of impacts. The data analysis revealed a strong component of low-density dust, 30 % of which may have ρ as low as 0.1 gcm^{-3} (Grün et al., 1980). Some of this dust was identified with the high-speed β-meteoroids also detected by the Pioneer 8 and 9 spacecrafts (McDonell, 1975, Berg and Grün, 1973).

The higher-density "apex" particles are evidently different from the agglomerates studied here which have $1.2 > \rho > 0.06$ gcm^{-3}. The "bird's-nests" correspond to a low-density component orbiting close to the invariable plane. Such a component would be discriminated in the Helios 1 and 2 data. A low-density component producing the zodiacal light would also explain the descrepancy between results from the Meteoroid Penetration Experiment or MPE ("beercans") experiment onboard Pioneer 10 and 11 spacecrafts, showing a constant penetration rate from the Earth out to beyond Jupiter (Hums et al., 1974), and the zodiacal light brightness observed from the same spacecrafts (for references, see Weinberg and Sparrow, 1978, p. 109). On the basis of the present study it might be expected that the low-density β-meteoroids are clums of a few or single grains. The existence of a higher-density component of even smaller grains (the bare grains in the bi-modal model for interstellar dust by Greenberg and Hong, 1973) is predicted.

5.5 Conclusions

It is concluded on the basis of this study that the following hypothesis are consistent with the current observations in the interplanetary medium;

(1) The primordial interstellar dust-complex may be described by the bi-modal model by Greenberg and Hong (1973), modified in the dense presolar nebula as described by Greenberg (1979).

(2) Comets aggregate from the thus described interstellar dust (Whipple, 1978).

(3) Some comets may develop an "ice"-free outer crust (Brin and Mendis, 1979).

(4) The zodiacal light results from scattering of sun-light by cometary debris (Whipple, 1976).

(5) β-meteoroids might be comet and zodiacal-light particle debris.

The high degree of polarization reported in cometary dust tails as far from the comet as the antitail, favours the "ice"-free agglomerates as representatives of comet debris. However, comets with large perihelie distances or "new" comets are possibly seeding agglomerates of primordial dust particles. These "bird's-nests" may be successively stripped of their volatiles as they spiral in towards the Sun under the action of the Poynting-Robertson drag. The degree of polarization might therefore be higher for light scattered by particles closer to the Sun than by dust observed at large elongations, thus shifting P_{max} towards smaller elongations. For numerous reasons (dust-dust collisions, volatile erosion, etc...) the "bird's-nests" are expected to sublimate at an increasing rate as they approach the Sun. The smaller or sufficiently "ice"-free debris are expelled from the Solar System by the radiation pressure or the solar wind and are observed as β-meteoroids. Other higher-density dust particles, such as asteroid fragments, are more easily observed by impact detectors and through cratering of surfaces exposed to the interplanetary medium, but do probably not significantly contribute to the zodiacal light (see also Whipple, 1976). Although the "classical" component of interstellar grains are thought to stream through the inner Solar System during part of the solar cycle (Gustafson and Misconi, 1979) and might be trapped in bound orbits under some conditions (Gustafson, unpublished calculations) they are not likely candidates for the zodiacal-light particles.

5.6 Suggestions for Further Research

Out of the topics that suggest themselves on the basis of the present study, only the ones that appear to be of the most fundamental character or most urgent are mentioned below. No reference is made to their relative importance.

- Observational studies of scattering functions for comet dust[1].
- Investigation of the low density dust component or components detected by the Helios space-probe (Grün et al., 1980).
- Renewed studies of interplanetary dust dynamics, and of the evolution of the zodiacal dust cloud, using the "bird's-nest" particle model[2].
- Determination of the domain of validity of the suggested scattering approximations.
- Adaptation of the Finson-Probstein (1968) method to the "bird's-nest" type particles, for prediction of shape and structure of comet tails[2].

1) To the knowledge of the author, polarimetry $P(\theta)$ covering an appreciable interval of scattering angle (θ) has only been performed for comet Ikeya-Seki 1965 VIII. Whereas no determinations of $I_{tot}(\theta)$ are known. Deduction of $I_{tot}(\theta)$ generally involves assumptions regarding the particle number density distribution. However, an instrument probing the scattered intensity per unit volume and therefore $I_{tot}(\theta)$ has been suggested to fly on the forthcoming probe to Halley's comet.

2) The values of the radiation pressure efficiency and the electric charge of the particles are of fundamental importance in evaluation of dust dynamics and yet often subject to wide extrapolations and guesses.

APPENDIX A

Scattering Relations for Arbitrary Targets and their Mirror Particles.

a:

In accordance with the reciprocity theorem for vector waves, we can invert the time without changing the scattering problem, thus replacing $\vec{k}_o$ with $-\vec{k}_s$ and $\vec{k}_s$ with $-\vec{k}_o$. It follows from simple transformation of coordinates that $I^r_{11} = I_{11}$, $I^r_{22} = I_{22}$, $I^r_{12} = I_{21}$ and $I^r_{21} = I_{12}$ where I^r are scattered intensities from the reciprocal position. The reciprocal position is reached by rotating the scatterer 180° around the bisectrix of the complement to scattering angle.

Assuming that for every particle there is one particle in the reciprocal position, $\Sigma I_{12} = \Sigma I_{21}$ over random orientations at any given scattering angle.

b:

Mirroring with respect to the scattering plane only changes the phase of the cross-polarization components, as the transformation only involves a change of sign of one coordinate. The attention of the reader is drawn to the fact that we refer to a second particle.

c:

A fourth related position is obtained by successively applying the two previous transformations *a* and *b*.

Use of the Symmetry Relations in the Laboratory.

Arbitrary Particles.

Only the relation described in *a* is valid. But with the present orientation mechanism the reciprocal position can only be reached when the tilt axis coincides with the bisectrix to the complement of the scattering angle.

Particles with an Axis of Symmetry.

The particle appropriately reorientated is its own mirror particle. The relations *a*, *b* and *c* all prevail. Let a vector parallel to the axis of symmetry be our reference. Relation *a* implies that all scattering information can be deduced as the vector sweeps the hemisphere on either side of the bisectrix plane, defined as the plane perpendicular to the scattering plane and containing the bisectrix of the complement to θ. Relation *b* implies that it is sufficient to let the vector sweep the hemisphere on any side of the scattering plane. Thus we need only to let the vector sweep a solid angle π bound by the scattering plane and the bisectrix plane. Orientations in the opposite quarter of the sphere are related through a, on the opposite side of the scattering plane but same side of the bisectrix plane are related through b and in the fourth quarter through c. It is thus sufficient that measurements be made only in a 1/4 of the sphere.

Particles with an Axis of Symmetry and a Plane of Symmetry Perpendicular to this Axis.

In addition to a, b and c, mirroring with respect to the plane of symmetry gives an equivalent position. Thus, orientations in the solid angle $\pi/2$ bound by the scattering plane, the bisectrix plane, and a plane perpendicular to both and containing the geometrical center of the target, are equivalent to orientations in the opposite $\pi/2$ solid angle. By successively applying relation a it is realized that it is sufficient to investigate orientations in the $\pi/2$ solid angle bound by the scattering plane and the bisectrix plane on either side of the mutually perpendicular plane through the target. Thus for such particles, only 1/8 of the orientations for arbitrary particles are independent.

APPENDIX B

Periodicity of the Oscillations in the Scattering Efficiency of "Bird's-nests" as they are Rotated

The optical path difference for light scattered by A and B (see Fig. B.1) is $|p-q|$. As χ is varied the optical path difference varies. When;

$$\mathrm{Re}\{\bar{m}\}|(p_{\chi+\Delta_n}-q_{\chi+\Delta_n})-(p_\chi-q_\chi)| = n\lambda$$

where λ is the wavelength of the incident radiation and $\bar{m}$ is given by eq. 3.1, the interference pattern has gone through n periods of oscillations.

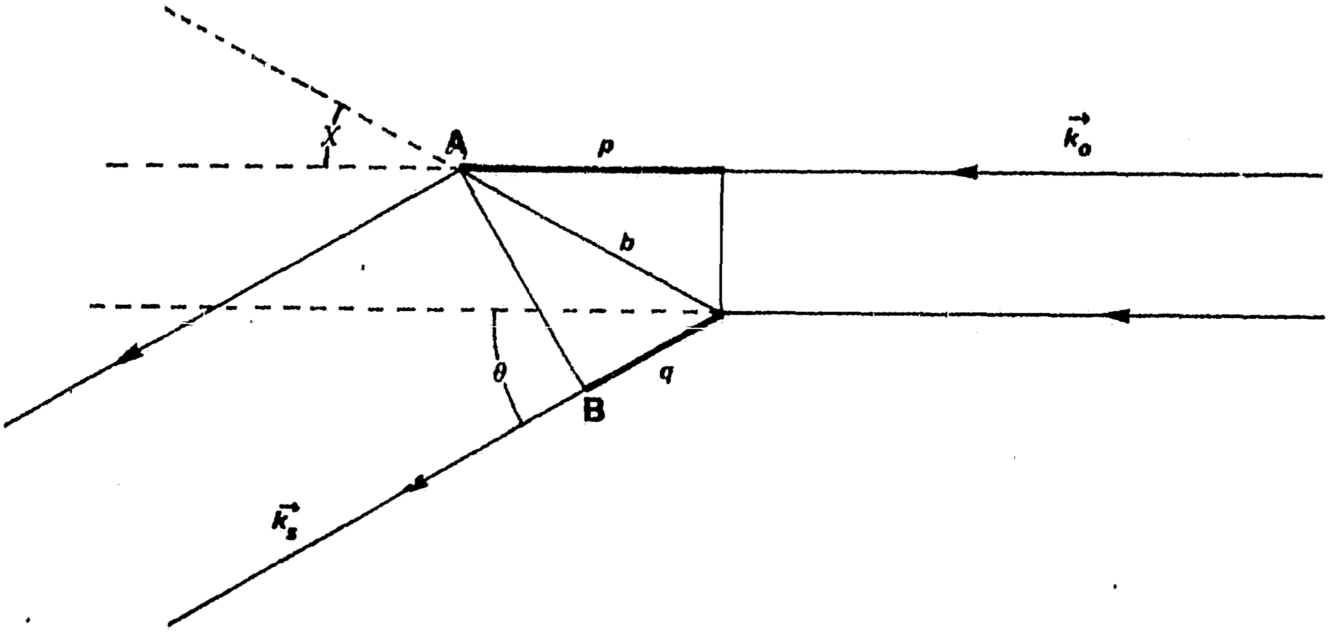

Fig. B.1 Scattering geometry projected on the scattering plane

The period $\Delta\chi$ is therefore defined by;

$$\mathrm{Re}\{\bar{m}\}\ b|\cos(\chi+\Delta\chi)-\cos(\chi+\Delta\chi+\theta)-\cos(\chi)+\cos(\chi+\theta)| = \lambda$$

Note that the distances p, q and b are all in the scattering plane, b is the projection of the distance between two scatterers in this plane. Any pair of scatterers separated by the distance a and with the line joining the two centers making an angle α with the scattering plane ($b = \cos\alpha$), will interfere such that they pass through one period of oscillation as the "bird's-nest" is rotated the angle $\Delta\chi$ from some orientation χ.

Consider a particle at the projected distance r in the scattering plane from the geometrical centre of the "bird's-nest", all particles at the projected distance b from this particle will be on the surface of the circular cylinder of

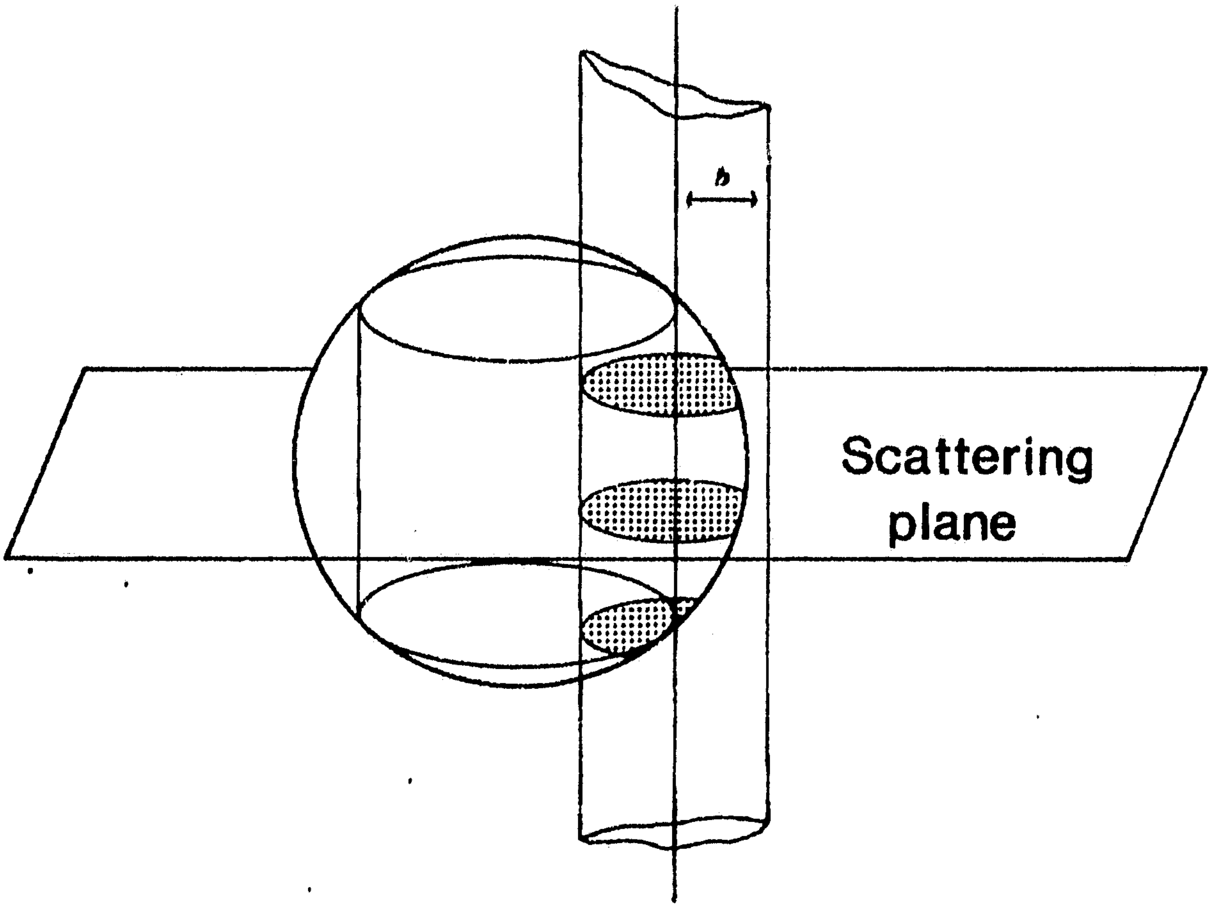

Fig. B.2 For each pair of interfering particles located each on one of the two cylindrical surfaces theire is an orientation of the spherical ensemble such as the resulting interference pattern goes through one period of oscillation as the conglomerate is rotated by an angle $\Delta\chi$.

radius b **with** the symmetry axis passing through the particle perpendicular to the **scattering plane.** As this cylinder is swept around the "bird's-nest" (always with **distance** r between the "bird's-nest" centre and the cylinder axis), an other **cylinder is** generated also with its symmetry axis perpendicular to the scattering **plane** (see fig. B.2). The total number P_{tot} of particle pairs with the projected **separation** b is the number of particles on the first cylindrical surface times the **number** of particles on the second surface.

A computer program generating Figs. B.3 looks for pairs whose individual projected distance are $b \pm d$ and where the first particle is at distance r to $r - \Delta r$. P_{tot} is therefore given by the volume V_1, corresponding to the first cylinder, times V_2, corresponding to the second cylinder, times the number density of particles. V_1 is bound by two cylindrical surfaces and two spherical surfaces and is computed using Simpsons formula. V_2 is also bound by two cylindrical and two spherical surfaces, but in such a way that it can easily be computed by addition and substraction of simple geometrical figures. It is seen from the Figs. B.3 that particle pairs producing short period oscillations exists only at the higher scattering angles. See also section 3.6.3 p. 32 and Figs. 4.1 and 4.2 on p. 40 - 42.

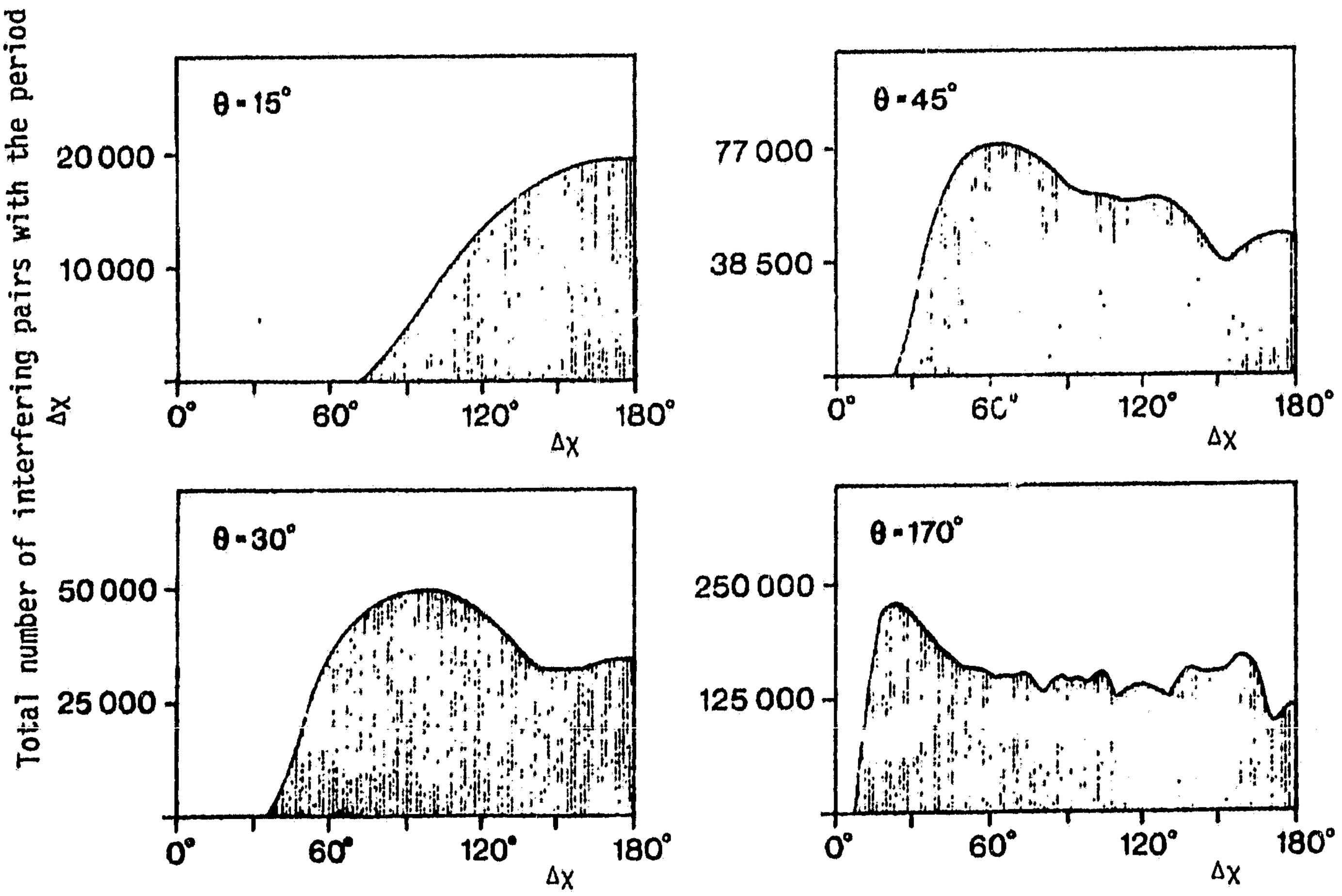

Fig. B.3 Total number of interfering pairs that goes through one period of oscillation as the ensemble is rotated an angle Δχ in the scattering plane from some initial orientation. The sperical X = 10.04 ensemble of 539 cylinders T41A is simulated at some scattering angles θ.

APPENDIX C

Scattering from a Cloud of Randomly Orientated Independent Infinite Circular Cylinders

A computer code to calculate scattering from single infinite circular cylinders at arbitrary orientation, excluding incidence along the axis of symmetry, as outlined by Lind (1966) and by Kerker (1969) was kindly provided by Dr. R. T. Wang. Note also the paper by Cohen (1980). The scattered light propagates along conical surfaces containing the $\vec{k}_0$ vector, the symmetry axis of the cone coincides with the cylinder axis. Thus, only cylinders whose axis of symmetry fall in the bisectrix plane (the plane perpendicular to the scattering plane and containing the bisectrix of the complement to θ), will contribute to the scattering in any given direction. The intensities are given in components tangential and perpendicular to the cone surface.

The geometry is shown in fig. C.1 in transformation to the coordinates

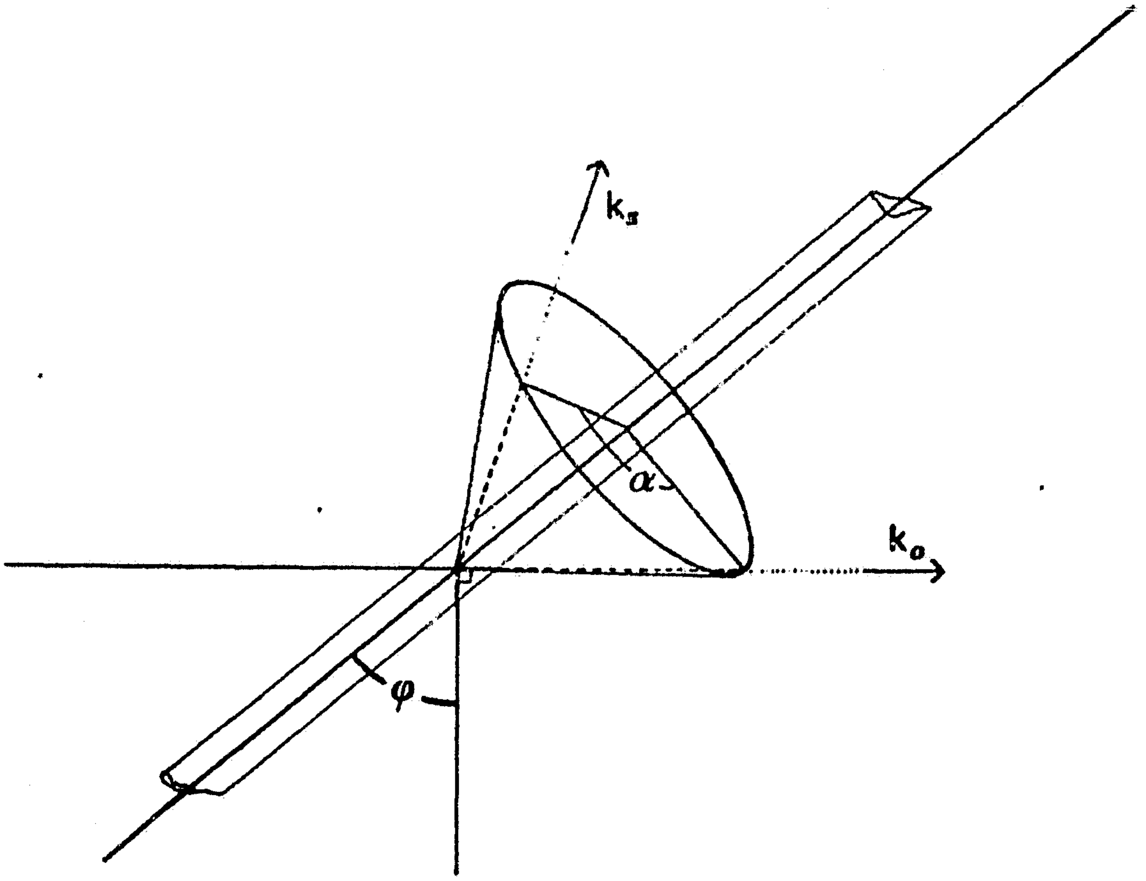

Fig. C.1 The geometry for scattering by an infinite cylinder.

θ, ψ, χ in the laboratory system (fig.2.1) the following relationships prevail.

$$\sin(\theta/2) = \cos(\varphi)\sin(\alpha/2)$$

$$\cos(\psi) = \frac{\cos(\varphi)\cos(\alpha/2)}{\cos(\theta/2)}$$

$$\chi = \theta/2$$

The intensities contributed by individual cylinders to the total scattered brightness are added, as the assumption of randomness in location implies randomness in relative phase.

To transform the second of Stokes parameters to a common coordinate system the phase relation between the four intensity components must be known as they interfere. The angular dependence of this relation is not yet derived, so we will only compute the total brightness.

Appendix D

The Infinite Cylinder Approximation for Scattering in the Far-field by Finite Cylinders

From Figs. 4.14 and 4.7 it seems that the angular dependence of scattering by finite cylinders at perpendicular incidence may be qualitatively approximated by that of infinite cylinders. Quantitatively the scattering is quite different. That off an infinite cylinder is concentrated precisely in the scattering cone so that the intensity at the far-field ($r \gg \lambda$) is inversely proportional to the distance r from the scatterer, while the scattering off finite cylinders is spread by diffraction (Lind, 1966, Greenberg, 1974) the intensity is proportional to r^{-2} when $r \gg \lambda$.

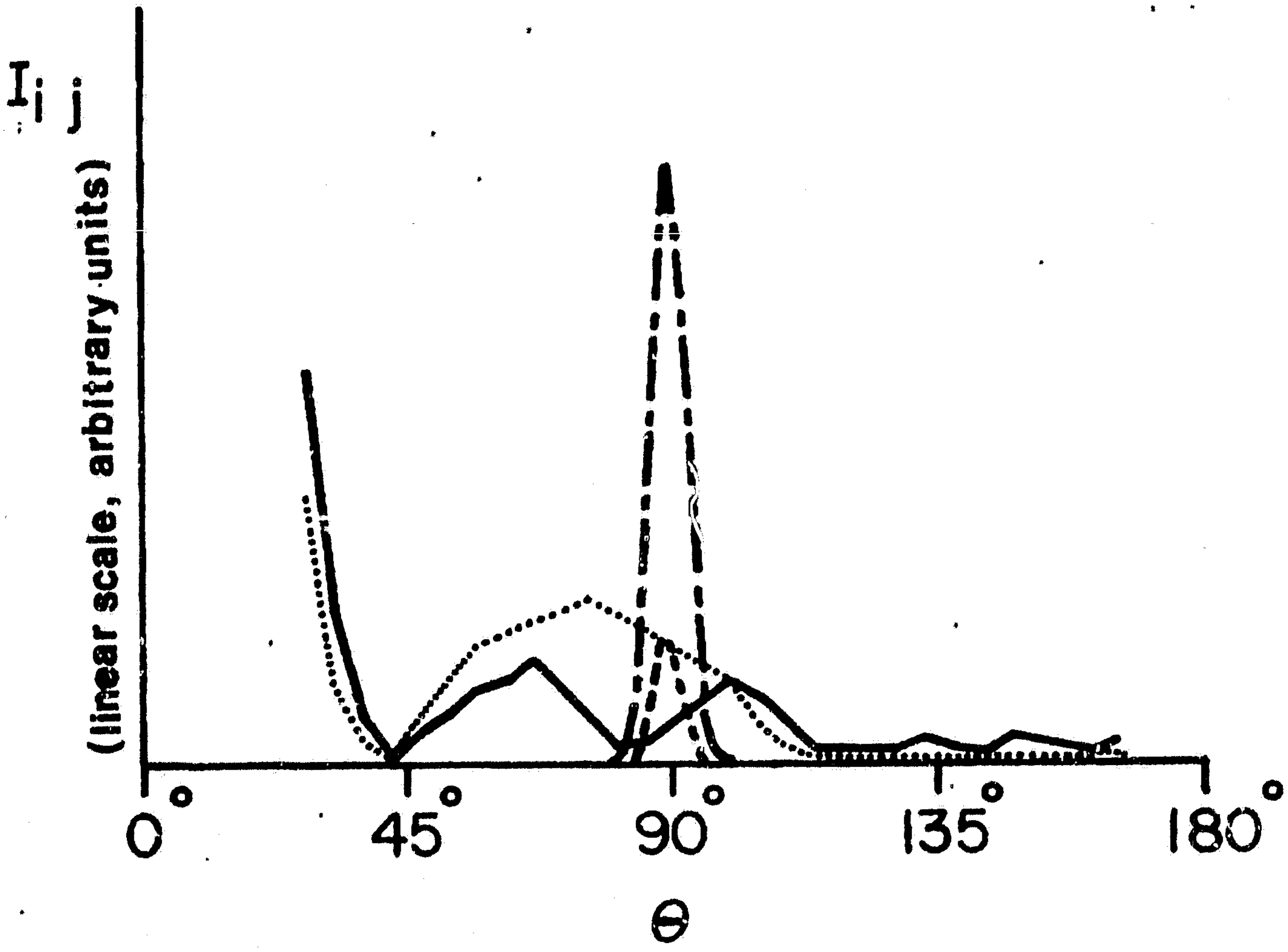

Fig. D.1 Experimental intensities versus scattering angle for radiation scattered off $x = 1.88$ lucite cylinders with their axes of symmetry pointing towards $\theta = 45^\circ$ ($\chi = 45^\circ$, $\psi = 90^\circ$). Dash-dot is for the I_{11}-component of the 210:1 -elongation cylinder extending well outside the beam, dashed curve is for the I_{22}-component from the same cylinder. Dotted curve is for the I_{11}-component scattered of the 4:1 -elongation cylinder C41, solid line is for the I_{22}-component. The background radiation (appendix E) was not compensated for.

The condition for scattering off an infinite cylinder towards a given direction is therefore that the cylinder symmetry axis is contained in the bisectrix plane (the plane perpendicular to the scattering plane and bisecting the complement to the scattering angle). Therefore, an infinite cylinder must be orientated perpendicular to the scattering plane in order to scatter in all directions θ in the scattering plane. An infinite cylinder with the orientation χ, ψ, (see appendix C) scatter in the forward direction $\theta = 0$ and $\theta = 2\chi$. In Fig. D.1 the scattering of a finite but long cylinder (extending outside the main lobe of both transmitting and receiving antenae) is shown. The cylinder is orientated such as the axis of symmetry is in the scattering plane and makes an angle $\chi = 44.6^\circ$ with the direction of propagation of the incident radiation. The receiving antena was swept from $\theta = 30^\circ$ to 170°, as expected we see a sharp peak in both scattered components I_{11} and I_{22} around $\theta = 2\chi = 89.2^\circ$. The radiation scattered off the finite cylinder is detectable in the whole interval of θ, shortward of $\theta = 45^\circ$ part of the forward scattering peak is seen. In Fig. D.2 the scattered brightness from the 4:1 -elongation cylinder averaged over "uniform" distribution of orientations is compared qualitatively to the computed brightness scattered by uniformly orientated infinite cylinders, normalized at $\theta = 90^\circ$. It is seen that the forward scattering peak extends out in side scattering thus seriously modifying the scattering pattern.

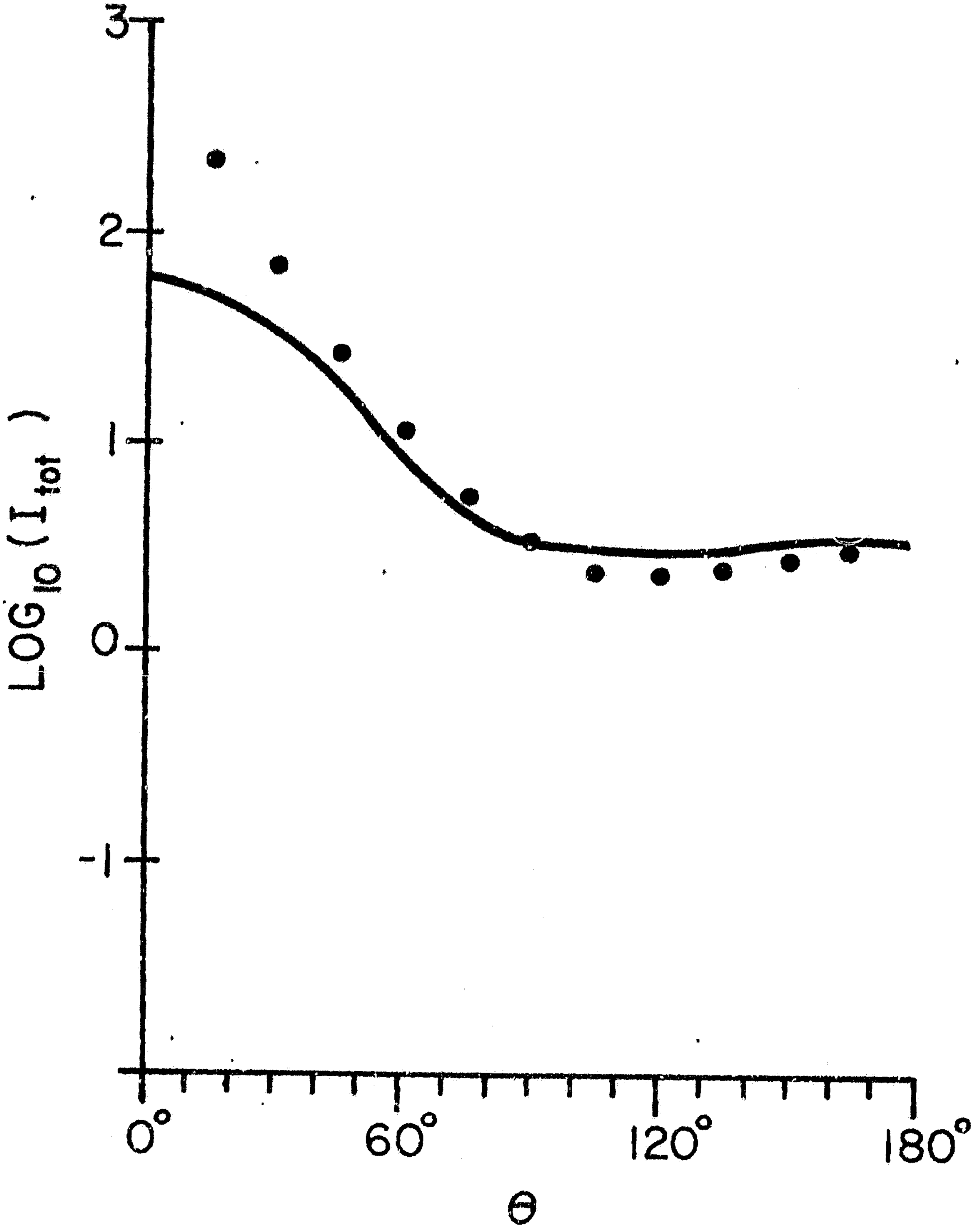

Fig. B.2 Total scattered intensities from $x = 1.88$ lucite cylinders, vesus scattering angle exept $\theta = 0°$. Dots are experimental results averaged over "uniform" distribution of orientations of the C41 cylinder (see section 2.7.1). Solid curve is for the uniform distribution of orientations for infinite cylinders, computed as described in appendix C.

Appendix E

The Background radiation in the Laboratory at S.A.L., and Detector Response

Fig. E.1 shows the background radiation versus scattering angle in the laboratory version A, in units of the potential over the detector as measured by the lock-in amplifier. If not mentioned otherwise, the background radiation was suppressed as described in section 2.5 (p. 9 - 19) to ≤ 0.1 µV. The scattering intensity 1 in absolute units corresonds to ~5 µV (the apparatus was calibrated using a standard target before and after each set of measurements and every 6 - 10 hours during the course of measurements).

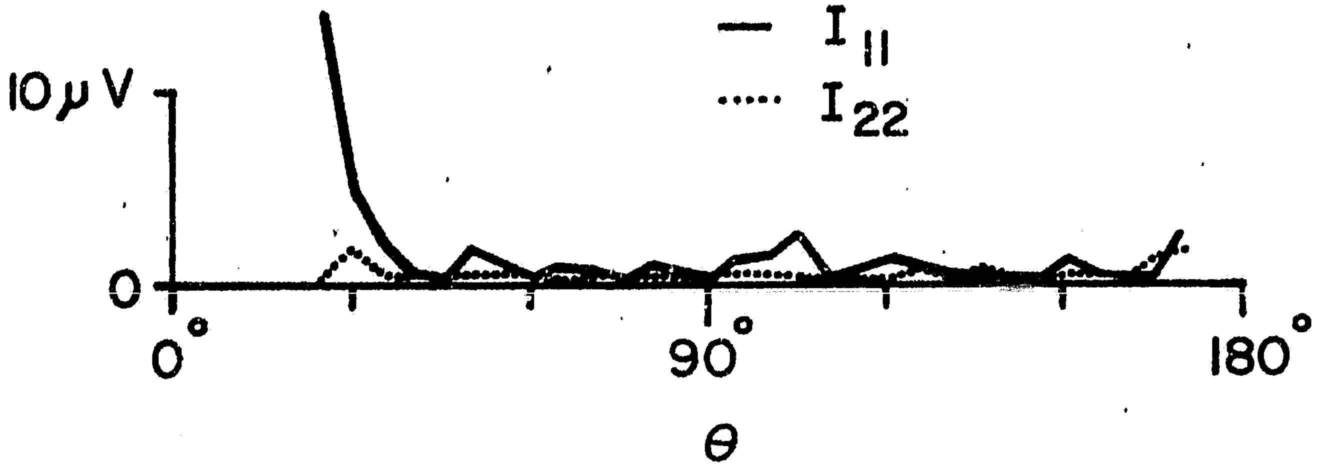

Fig. E.1 The background radiation versus scattering angle in the laboratory version A, when the background compensation waveguide was disconnected.

In the data reduction, a linear relationship was assumed to prevail between the detector unit response and the intensity of scattered radiation. This assumption is motivated by the measured linearity (Fig. E.2) in the range up to 10mV used in the measurements.

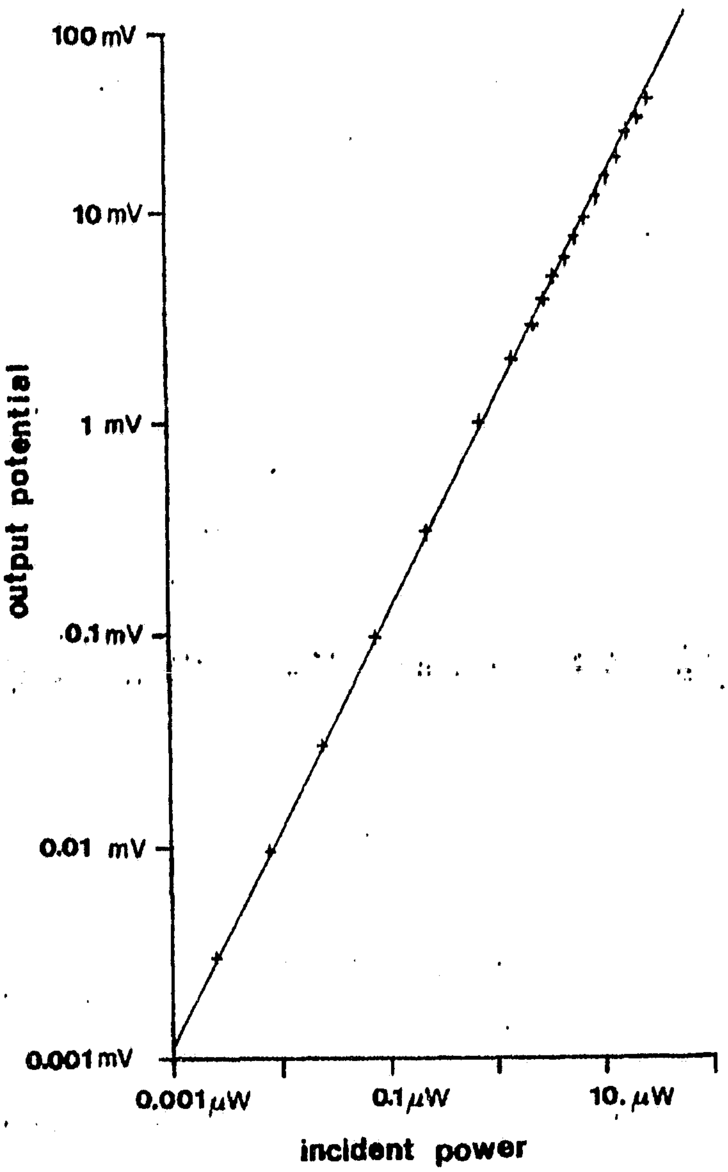

Fig. E.2 The response of the detector unit as a function of incident power.

Acknowledgements

The author had the extreme pleasure during the course of this work, to collaborate with a stimulating group of scientists who selflessly shared their vast experience.

My warm and sincere thanks go especially to Professor J. Mayo Greenberg, director for Laboratory Astrophysics at Rijksuniversiteit te Leiden, the Netherlands, who generousely offered advice, many scientific discussions and continously acted for the most efficient way to work on problems of mutual interest of which this study was the first step. In the fall of 1977, Dr. Greenberg who in effect was the director of this work gave me the opportunity to join the Space Astronomy Laboratory at Albany, New York.

Dr. Ru T. Wang of the Space Astronomy Laboratory helped to clarify numerous aspects of the light scattering problem, his invaluable contributions are gratefully acknowledged. I also owe a great debt of gratitude to Dr. Donald W. Schuerman, director of the micro-wave laboratory at S.A.L., for practically unlimited access to the laboratory and for stimulating discussions, as well as many suggestions leading to improvements of the present report.

It is also a pleasure to express my deep gratitude to Professor Jerry L. Weinberg, for his hospitality at the Space Astronomy Laboratory and for his continual interest and encouragement. I also wish to thank Mr. Richard C. Hahn for his support in the laboratory, Mrs. Isabèle Nierenberg and Mr. David E. Beeson for help with computer-related problems, as well as the rest of the staff at the Space Astronomy Laboratory for their encouragement and help in various ways.

I am also grateful to Professor R. H. Giese and Dr. R. H. Zerrull, Ruhr University for their generosity in making available the millimeter-laboratory at the Bereich Extraterrestiche Physik during part of August 1979.

Professor G. Larsson-Leander, director of Lund Observatory, Sweden has kindly provided support in many practical aspects of the work, as well as advice on the writing and many suggestions leading to improvements of the manuscript. To him and to Professor T. Elvius, past director of Lund Observatory I owe sincere thanks for their support of and interest in this work. I also wish to take this opportunity to express my gratitude to Professor A. Elvius at Stockholm Observatory.

All those who have helped me in various ways with typewriting, drawing of figures, printing of the manuscript and in other respects, I heartily thank for their efforts.

Finally, I gratefully acknowledge grants received from the Lennander Foundation of Uppsala University, Lars Hierta Foundation of the Royal Swedish

Academy of Sciences, the Faculty of Natural Sciences of Lund University, and the NASA Planetary Atmospheres Program under contract NSG 7093.

Lund Observatory, Lund,
October, 1980
Bo Å. S. Gustafson

REFERENCES

Brin, G. D., Mendis, D. A., 1979, Dust release and mantle development in comets, *Astrophys. J.*, 229, p. 402.

Brophy, J. J., 1977, *Basic Electronics for Scientists*, (eds. Zappa, C. R., Gardner, M.), McGraw-Hill Inc..

Brownlee, D. E., 1978, Microparticle studies by sampling techniques, in *Cosmic Dust*, (ed. McDonnell, J. A. M.), J. Wiley & Sons, New York, p. 295.

Cohen, A., 1980, Scattering of a linearly polarized incidence at arbitrary angle to incident plane of infinite tilted cylinders, *Optics Letters*, 5, #4, p. 150.

Delsemme, A. H., Rud, D. A., 1973, Albedos and cross-sections for the nuclei of comets 1969 IX, 1970 II and 1971 I. *Astron. and Astrophys.*, 28, p. 1.

Dumont, R., 1965, Séparation des composantes atmosphérique interplanétaire et stellaire du ciel nocturne a 5000 Å. Application a la photometrie de la lumière zodiacale et du Gegenschein, *Ann. Astrophys.*, 28, p. 265.

Dumont, R., 1972, Intensité et polarisation de la lumière solaire diffusée par un volume isolé de matière interplanétaire, *Comp. Rend. Acad. Sci. Paris*, 275, p. B-765.

Dumont, R., 1973, Phase function and polarization curve of interplanetary scatterers from zodiacal light photopolarimetry, *Planet. Space Sci.*, 21 p. 2149.

Dumont, R., 1975, On the gradient of zodiacal light with heliocentric distance., *Planet. Space Sci.*, 23, p. 1235.

Dumont, R., 1976, Ground-based observations of the zodiacal light, in *Interplanetary Dust and Zodiacal Light*, (eds. Elsässer, H., and Fechtig, H.), I.A.U. Coll. No 31, Springer-Verlag, Heidelberg, p. 85.

Dumont, R., Sánchez, F., 1975, Zodiacal light photopolarimetry II. Gradients along the ecliptic and the phase functions of interplanetary matter, *Astron. & Astrophys.*, 38, p. 405.

Fechtig, H., 1976, In-situ records of interplanetary dust particles - methods and results, in *Interplanetary Dust and Zodiacal Light*, (eds. Elsässer, H., and Fechtig, H.), I.A.U. Coll. No 31, Springer-Verlag, Heidelberg, p. 143.

Finson, M. L., Probstein, R. E., 1968, A theory of dust comets, I, model and equations, *Astrophys. J.*, 154, p. 327.

Frey, A., Hoffmann, W., Lemke, D., Thum, C., 1974, Photometry of the zodiacal light with the balloon-borne telescope THISBE, *Astron. and Astrophys.*, 36, p. 447.

Giese, R. H., 1970, Tabellen von Mie-Streufunktionen I, *Max Planck Institut, München, MPI-PAE extraterr.*, 40.

Giese, R. H., 1971, Tabellen von Mie-Streufunktionen II, *Max Planck Institut, München, MPI-PAE extraterr.*, 58.

Giese, R. H., Schwehm, G., Zerull, R., 1974, Grundlagenuntersuchungen zur interpretation extraterrestrischer zodiakallichtmessungen und lichtstreuung von staubpartikeln verschiedener formen, *Bochum, BMFT-FBW* 78.

Giese, R. H., Weiss, K., Zerull, R., Ono, T., 1978, Large fluffy particles: a possible explanation of the optical properties of interplanetary dust, *Astron. and Astrophys.*, 65, p. 265.

Greenberg, J. M., 1970, Models of the zodiacal light, in *Space Res. X*, (eds. Donahue, T. M., Smith, P. A., Thomas, L.), p. 225.

Greenberg, J. M., 1974, Some examples of exact and approximate solutions in small particle scattering: a progress report, in *Planets, stars and nebulae studied with photopolarimetry*, (ed. Gehrels, T.), U. of Arizona Press, p. 107.

Greenberg, J. M., 1978, Interstellar dust, in *Cosmic Dust*, (ed. McDonnell, J. A. M.), J. Wiley & Sons, New York, p. 187.

Greenberg, J. M., 1979, Pre-stellar interstellar dust, *Moon and Planets*, 20, p. 15.

Greenberg, J. M., 1980, From interstellar dust to comets to the zodiacal light, invited paper presented at I.A.U. Symposium No 90, Ottawa.

Greenberg, J. M., Gustafson, B. Å. S., 1980, A comet fragment model for zodiacal light particles, to appear in *Astron. and Astrophys.*

Greenberg, J. M., Hong, S.-S., 1974, The chemical composition and distribution of interstellar grains, I.A.U. Symposium No 60, Telaviv, p. 155.

Greenberg, J. M., Lind, A. C., Wang, R. T., Libelo, L. F., 1967, in *Electromagnetic scattering*,(eds. Rowell, L. & Stein, R.), Gorden & Breach, New York, p. 3.

Grün, E., Pailer, N., Fechtig, H., Kissel, J., 1980, Orbital and physical characteristics of micrometeoroids in the inner solar system as observed by HELIOS 1, *Planet. Space Sci.*, 28, p. 333.

Gustafson, B. Å. S., Misconi, N. Y., 1979, Streaming of interstellar grains in the solar system, *Nature*, 282, p. 276.

Hagen, W., Allamandola, L. J., Greenberg, J. M., 1979, Interstellar molecule formation in grain mantles: the laboratory analog experiments, results and implications, *Astrophys. Space Sci.*, 65, p. 215.

von Hippel, 1954, *Dielectrics and Waves*, John Wiley & Sons, New York, p. 231.

Hong, S.-S., Greenberg, J. M., 1980, A unified model of interstellar grains: A connection between alignement efficiency, grain model size, and cosmic abundance, *Astron. Astrophys.*, 88, p. 194.

Huges, D. W., 1974, Cosmic dust influx to the upper atmosphere during the major meteor showers, in *Space Research XIV*, Akademie-Verlag, Berlin, p. 709.

van de Hulst, H. C., 1957, *Light Scattering by Small Particles*, John Wiley & Sons, New York.

Irvine, W. M., Leschine, S. B., Schloerb, F. P., 1980, Thermal history, chemical composition and relationship of comets to the origin of life, *Nature*, 283, p. 748.

Kerker, M., 1969, *The Scattering of Light*, Academic, New York.

Lanzerotti, L., J., Brown, W. L., Poate, J. M., Augustyniak, W. M., 1978, Low energy cosmic ray erosion of ice grains in interplanetary and interstellar media, *Nature*, 272, p. 431.

Leinert, C., Link, H., Pitz, E., 1974, Rocket photometry of the inner zodiacal light, *Astron. & Astrophys.* 30, p. 411.

Le Sergeant, L. B., Lamy, P. L., 1978, Interplanetary dust: are there two independent populations?, *Nature*, 276, p. 800.

Lind, A. C., 1966, Electromagnetic scattering by finite cylinders, Ph.D. Thesis, Resselaer Polytechnic Institute, Troy, New York.

Matyagin, V. S., Sabitov, Sh. N., Kharitonov, A. V., 1968, Polarimetry of the tail of comet Ikeya-Seki, *Soviet Astron. -AJ*, 11, p. 863.

Nagel, K., Neukum, G., Eichhorn, G., Fechtig, H., Müller, o., Schneider, E., 1975, Dependencies of microcrater formation on impact parameters, *Max-Planck -Inst. Kernphysik Heidelberg, MPIH-1975-V10*, p. 171.

Schaefer, R.,1980, Ph.D. Thesis, State University of New York at Albany, Albany, New York, in preparation.

Schuerman, D. W., 1980, Evidence that the properties of interplanetary dust beyond 1 AU are not homogeneous, paper presented at I.A.U. Symposium No 90, Ottawa.

Schuerman, D. W., Wang, R. T., Gustafson, B. Å. S., 1980, in preparation.

Sekanina, Z., Farrell, J. A., 1980, Evidence for fragmentation of strongly nonspherical dust particles in the tail of comet West 1976 VI, paper presented at I.A.U. Symposium No 90, Ottawa.

Verniani, F., 1969, Structure and fragmentation of meteoroids, *Space Sci. Rev.*, 10, p. 230.

Wang, R. T., 1968, Electromagnetic scattering by spheres of anisotropic refractive indices, Ph.D. Thesis, Rensselaer Polytechnic Institute, Troy, New York.

Wang. R. T., Greenberg, J. M., 1978, Final Report, *NASA NSG 7353, August*.

Weinberg, J. L., 1964, The zodiacal light at 5300 Å, *Ann. Astrophys.*, 27, p. 718.

Weinberg, J. L., 1967, *The Zodiacal Light and Interplanetary Medium*, (ed. Weinberg, J. L.), NASA SP-150.

Weinberg, J. L., Beeson, D. E., 1976, Photoelectric polarimetry of the tail of comet Ikeya-Seki (1965 VIII), in *The Study of Comets*, Proc. I.A.U. Colloq. No. 25, (ed. Donn, B., et al.) NASA SP-393, p. 92.

Weinberg, J. L., Mann, H. M., 1968, Negative polarization in the zodiacal light, *Astrophys. J.*, 152, p. 665.

Weinberg, J. L., Sparrow, J. G., 1978, Zodiacal light as an indicator of interplanetary dust, in *Cosmic Dust*, (ed. McDonnell, J. A. M.), J. Wiley & Sons, New York, p. 75.

Whipple, F. L., 1951, A comet model. II. physical relations for comets and meteors, *Astrophys. J.*, 113, p. 464.

Whipple, F. L., 1976, Sources of interplanetary dust, in *Interplanetary Dust and Zodiacal Light*, (eds. Elsässer, H., and Fechtig, H.), I.A.U. Coll. No 31, Springer-Verlag, Heidelberg, p. 403.

Whipple, F. L., 1978, Comets, in *Cosmic Dust*, (ed. McDonnell, J. A. M.), J. Wiley & Sons, New York, p. 1.

Wickramasinghe, N. C., 1973, *Light Scattering Functions for Small Particles*, Hilger, London.

Wolstencroft, R. D., Rose, L. J., 1967, Observations of the zodiacal light from a sounding rocket, *Astrophys. J.*, 147, p. 271.

Zerull, R., 1973, Mikrowellenanalogieexperimente zur lichtstreuung an staubpartikeln, *Bochum*, *BMFT-FBW* 73.

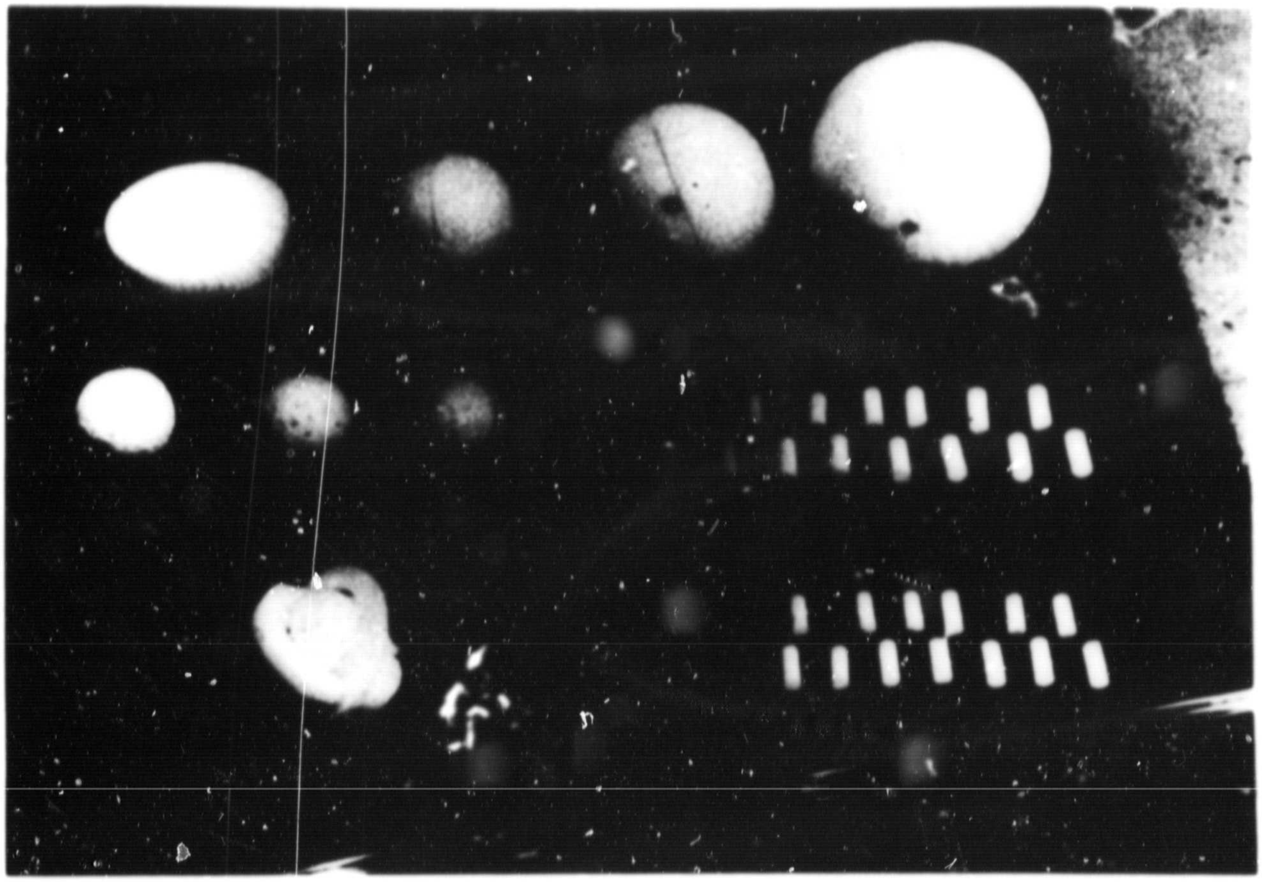

The sets of measurements represented in the diagram to the right were performed using cylinders as single targets or assembled in "bird's-nest" structures. A selection of the modules is shown above. In the upper left corner the ensemble P11 is seen and from the left in the middle row targets T11R, T41R and T41A. During measurements targets T11R, T21R and T41R were mounted in the annular rings fitted around T21R below. On the bottom, part of the long single x = 1.88 cylinder is seen.

SECTION 1

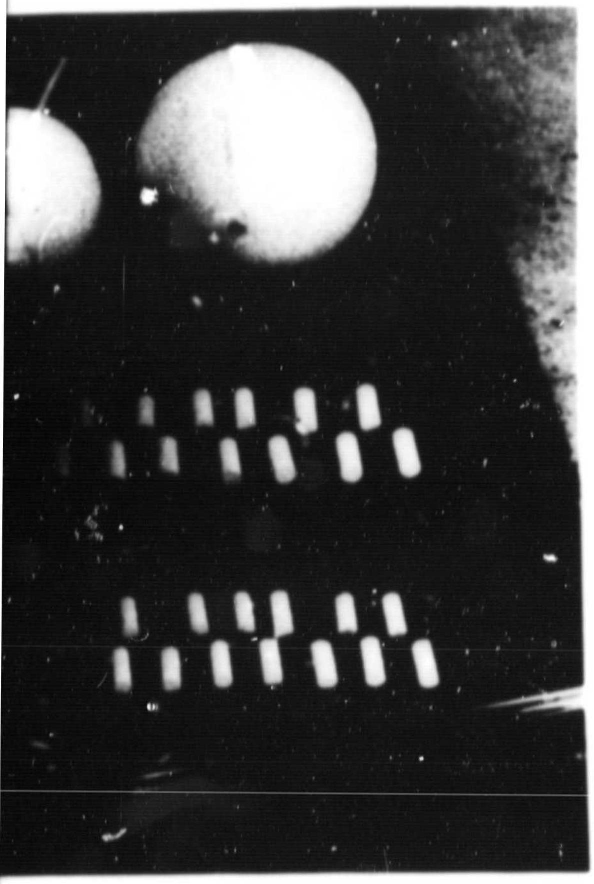

-nted in the diagram to the right
is single targets or assembled in
-ction of the modules is shown
r the ensemble P11 is seen and from
-ts T11R, T41R and T41A. During
R and T41R were mounted in the annular
. On the bottom, part of the long single

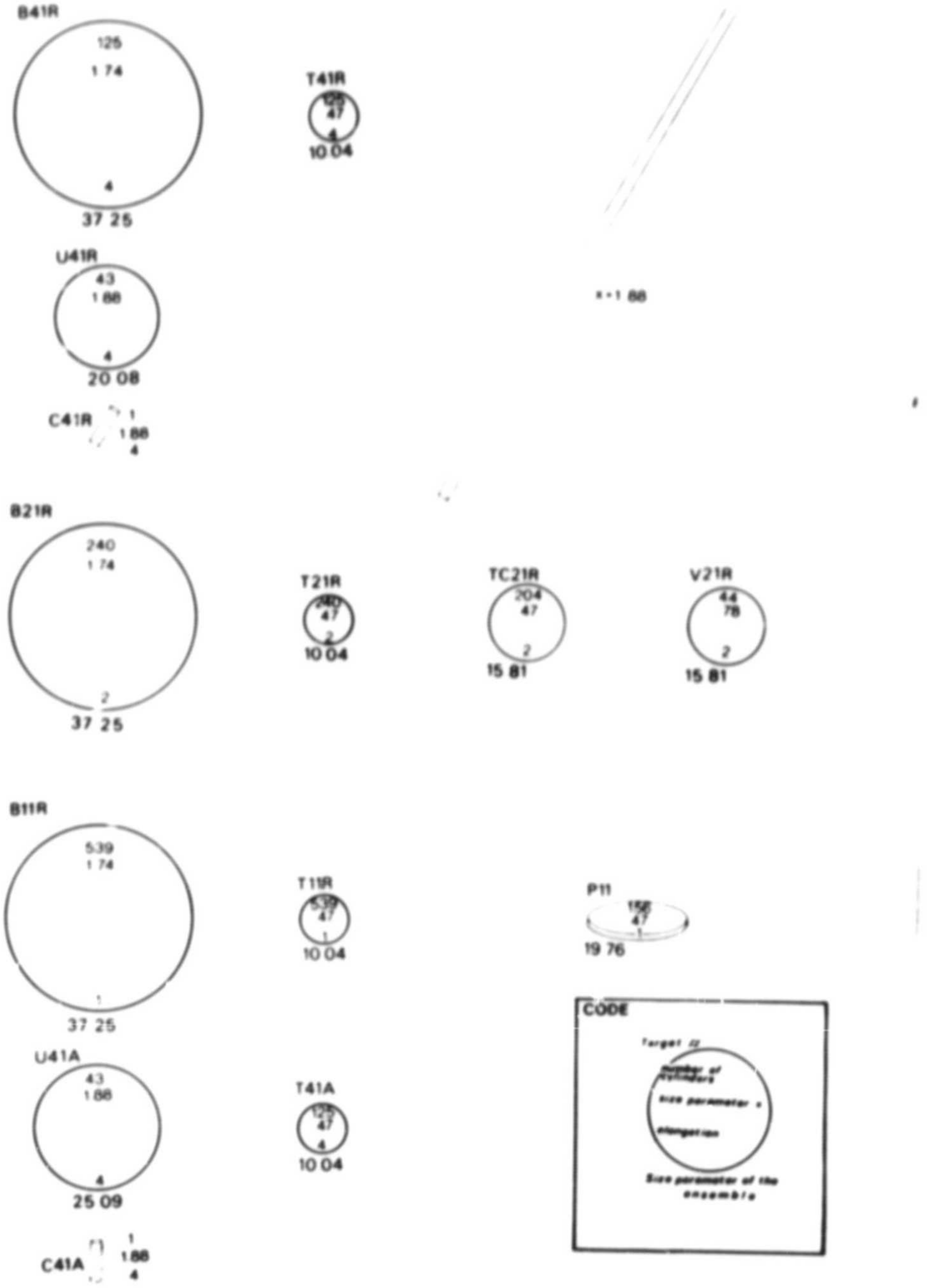

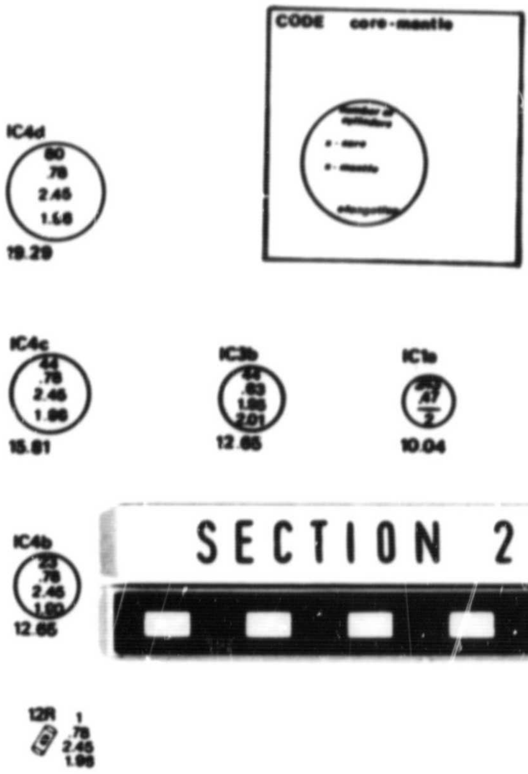

SECTION 2